Master's Thesis

Dual Band Circular Polarization Selective Structures for Space Applications

Johan Lundgren

Department of Electrical and Information Technology,
Faculty of Engineering, LTH, Lund University, 2016.

Dual Band Circular Polarization Selective Structures for Space Applications

LUND
UNIVERSITY

Department of Electrical and Information Technology
Faculty of Engineering, Lund University,
SE-221 00, Lund, Sweden

Author:
Johan Lundgren

Supervisors:
Daniel Sjöberg &
Andreas Ericsson

Examiner:
Mats Gustafsson

August 24, 2016

Abstract

Satellites are key components in today's modern world, but they are expensive to launch and the orbits are crowded. With use of a dual band circular polarization selective structure (CPSS) the satellites can be improved and the number of reflectors needed to carry out a certain task can be reduced. A dual band CPSS reflects one handedness of circular polarization and transmits the other, over a certain frequency band, and over the other frequency band the opposite occurs. This can be done with use of a CPSS coated reflector or a diplexer type setup. This thesis investigates, through full wave simulations of normal incidence, different candidates for dual band reciprocal symmetrical CPSS. The frequency bands of interest in this thesis are 17.7-20.2 GHz and 27.5-30.0 GHz and the goals are: insertion loss and return loss of less than 0.50 dB and an axial ratio of less than 0.78 dB (or 1.74 dB if diplexer setup is considered) for the targeted circular polarization within the frequency band.

The dual band CPSS candidates consists of multiple layers of non-resonant metal elements, meander lines and capacitively loaded strips, on substrates inter-spaced by low-permittivity foam sheets. Two meander line designs of 6 and 9 layers fulfill the goals specified for the diplexer setup with a bandwidth of 14.73-20.55 GHz (33.0%) and 27.04-30.82 GHz (13.1%) for the 6 layer design, 14.55-20.76 GHz (35.2%) and 27.20-30.31 GHz (10.8%) for the 9 layer design. Moreover the 9 layer meander line design fulfill most of the stricter axial ratio requirement with bandwidth of 16.16-20.38 GHz (23.1%) and 28.31-29.53 GHz (4.2%).

Sammanfattning

Satelliter är nyckelkomponenter i dagens moderna värld, dock är de dyra att skjuta upp och omloppsbanorna är fullpackade. Genom att använda en cirkulärpolariseringsselektiv struktur (CPSS) kan satelliter förbättras och antalet reflektorer som behövs för att utföra en viss uppgift minskas. Detta kan genomföras genom att belägga en reflektor med en CPSS struktur eller genom att använda en diplexer-uppställning. En tvåbandig CPSS reflekterar den ena polarisationen och transmitterar den andra över ett visst frekvensband och över det andra frekvensbandet sker det omvända. Detta examensarbete undersöker, genom fullvågssimuleringar vid normalt infall, olika kandidater för tvåbandig reciprok-symmetrisk-CPSS. Frekvensbanden är 17.7-20.2 GHz och 27.5-30.0 GHz samt målen är: Inkopplingsförlust samt reflektionsförlust lägre än 0.50 dB och en axelkvot lägre än 0.78 dB (1.74 dB, om en diplexerupp- ställning tänks användas) för de berörda polarisationerna inom frekvensbanden.

De tvåbandiga CPSS-kandidaterna består av flertalet lager av icke-resonanta metallelement, meanderlinjer och kapacitivt lastade remsor, tryckta på substrat med låg-permitivitetsmaterial som distanser. Två meanderlinedesigner bestående av 6 och 9 lager uppfyller de specificerade kraven för en diplexeruppställning. Deras bandbredd är 14.73-20.55 GHz (33.0%) och 27.04-30.82 GHz (13.1%) för designen med 6 lager, 14.55-20.76 GHz (35.2%) och 27.20-30.31 GHz (10.8%) för designen med 9 lager. Utöver detta uppfyller designen med 9 lager meanderlinjer merparten av de striktare axelkvotskravet med en bandbredd på 16.16-20.38 GHz (23.1%) och 28.31-29.53 GHz (4.2%).

Contents

Acknowledgements

First and foremost I would like to thank Professor Daniel Sjöberg for introducing me to the concepts of which the thesis is based and for providing insightful comments along the way. I would also like to thank Andreas Ericsson for all the long discussions we had and for all support guiding me through.

I extend thank, despite all crashes and power outages, to the computational computers. I am glad you eventually saw the possibilites and decided to work with me.

Lastly I thank my father, mother and sister for their supporting and believing in me during this work and throughout the years.

Acronyms

AR Axial Ratio.

CP Circular Polarization.

CPSS Circular Polarization Selective Structure.

CST Computer Simulation Technology.

DGR Dual Gridded Reflector.

ESA European Space Agency.

FEM Finite Element Method.

FIT Finite Integration Technique.

IEEE Institute of Electrical and Electronics Engineers.

IL Insertion Loss.

LH Left Handed.

LHCP Left Hand Circular Polarization/Polarized.

LHCPSS Left Hand Circular Polarization Selective Structure.

LP Linear Polarization.

LPSS Linear Polarization Selective Structure.

RH Right Handed.

RHCP Right Hand Circular Polarization/Polarized.

RHCPSS Right Hand Circular Polarization Selective Structure.

RL Return Loss.

XPD Cross Polar Discrimination.

Chapter 1

Introduction

1.1 Background and Motivation

In this day and age communication with electromagnetic waves is widely used and satellites in orbit are a key component in connecting areas around the world. Today there are more than 2000 satellites for communication purposes, and putting a satellite in these very crowded orbits is an expensive endeavour, which means reducing the cost and improving functionality is always welcome. When dealing with satellite links certain frequency bands are used and naturally one wishes to send as much information as possible within these bands. A way to be able to do this is to use orthogonal polarization of the electromagnetic waves. Linear Polarization (LP) is well understood and suitable in some applications. Changing polarization of the transmitted wave for linear polarization from one orthogonal state to the other is simply done by rotating the transmitting antenna 90°. A drawback of using linearly polarized electromagnetic waves is that the receiving antenna needs to be oriented in the same direction as the transmitting antenna to maximize the signal received [1]. Naturally one understands that it is problematic to maintain an alignment when working with satellites and linear polarization is not preferred. Another unwanted effect is the Faraday rotation which will rotate the linear polarized light as it propagates through the ionosphere, creating further misalignment [1]. Instead Circular Polarization (CP) is preferred since there is not an alignment requirement between transmitting and receiving antennas and moreover there is less path loss compared to linear polarization [2]. The requirement is simply that the receiver/transmitter must be designed for one of the orthogonal circular polarizations.

There is a demand for higher data rates in the near future and this pushes the next generation communication satellites to operate in higher frequency bands. These high throughput satellites will have two frequency bands for

uplink and downlink communication. Their operational bands are likely to be 18.2-20.2 GHz and 28-30 GHz but can be extended to the wider bands 17.7-20.2 GHz and 27.5-30 GHz [3]. The satellites are expected to use multiple spot beam systems [2]. In combination with multiple beams the satellites often reuse frequency and polarization in order to create coverage of the intended landmass without ever having a mutual overlap and thus reducing interference in communication. An example of coverage is seen in Figure 1.1 where the spots are coded after frequency and polarization.

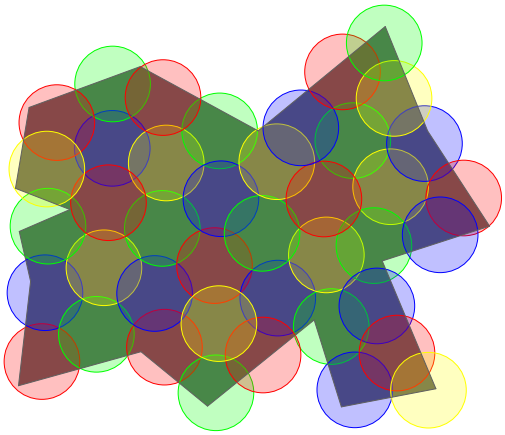

Figure 1.1: Example of multi-beam coverage (red= $\{f_1, \text{RHCP}\}$, green= $\{f_1, \text{LHCP}\}$, blue= $\{f_2, \text{RHCP}\}$, yellow= $\{f_2, \text{LHCP}\}$) of an arbitrary landmass (gray)

This kind of satellite coverage can be realized using many reflectors as seen in Figure 1.2, typically one reflector per beam color seen in Figure 1.1. Not only is the satellite spatially large but it is very costly to have several reflectors and this solution is thus not preferred. There are ways reflectors can be improved. One way involves being able to separate the polarizations with some kind of structure. In the case of linearly polarized electromagnetic waves it is simple to carry out this separation of the polarizations. A Linear Polarization Selective Structure (LPSS) can be as simple as a metallic grid. Electromagnetic waves impinging with polarization parallel to the metallic grid will be reflected and polarization perpendicular to the grid will pass through unhindered. A Dual Gridded Reflector (DGR) using these grid structures can be used to separate orthogonal linear polarizations and realize different lobe forms for the two polarizations. DGR is a very interesting concept useful for this problem. However a DGR is for linear polarization and finding an equivalent structure for circular polarization

is not as simple. If Circular Polarization Selective Structure (CPSS) (and DGR equivalents) are considered to exist then there are two ways they can be used to improve and reduce the number of reflectors.

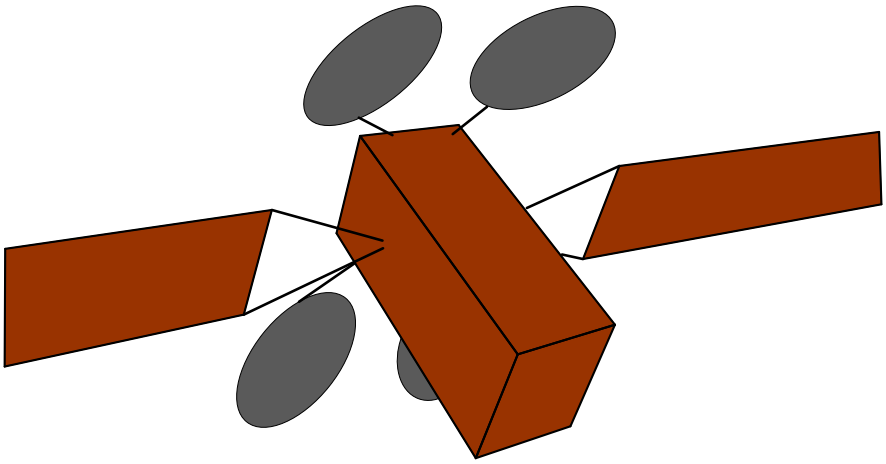

Figure 1.2: A satellite with four gray reflectors.

Consider the case of Right Handed (RH) and Left Handed (LH) CP. For a dual band scenario the structure will reflect Right Hand Circular Polarization/Polarized (RHCP) and transmit Left Hand Circular Polarization/Polarized (LHCP) in one of the frequency bands and in the other band the opposite will occur (reflect LHCP, transmit RHCP). One proposed structure involves a DGR equivalent for circular polarization. The European Space Agency (ESA) has suggested three different approaches involving CPSS to create a DGR equivalent [4]. For the DGR's suggested, certain polarization and frequency combinations are reflected in the first layer of the reflector and others in the second layer and so the different beams will have different lobe forms.

The other option is to use the CPSS as a diplexer where the different polarizations and frequencies are reflected or transmitted by a flat structure and on to a common reflector, this is seen in Figure 1.3 [5, 6]. In this case recieving and transmitting is done by the same physical horn and thus two horns are needed for the configuration in Figure 1.3. This setup will enable the use of four color coverage, depicted in Figure 1.1, with only two reflectors as opposed to the four reflectors currently needed.

The two types of structures for a dual band scenario that has been described is what this thesis aims to investigate. Depending on the result

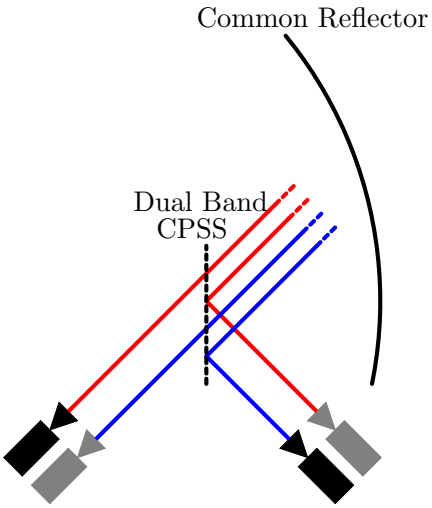

Figure 1.3: Example of usage of dual band CPSS as a diplexer. Transmitters are black, receivers are gray and RHCP is marked with red lines and the blue lines corresponds to LHCP.

one of these options might be better than the other. The purpose of the thesis is to present a functional dual band CPSS (simulated in a full wave solver) working according to certain specifications that will be presented in upcoming section. Developing a dual band CPSS enables the use of the aperture of the satellite more efficiently and allows for more missions per satellite, a quality highly sought for [7, 8].

1.2 Course of Action and Target goals

This thesis aims to present dual band CPSS candidates for use in space application for the two bands 17.7-20.2 GHz and 27.5-30 GHz. The designs will be simulated for normal incidence and optimized in CST Studio Suite 2015. The performance requirements of the structures will be discussed more later but are also stated here for completeness (Table 1.1) . Their definitions are found in the Chapter 3.

Table 1.1: Summarizing the targets for the CPSS. Band 1 is 17.7-20.2 GHz, Band 2 is 27.5-30 GHz. The higher values for axial ratio are the relaxed requirements.

	Pol. Band 1	Pol. Band 2	Target Value
Insertion Loss	RH	LH	$\leq$ 0.5 dB
Return Loss	LH	RH	$\leq$ 0.5 dB
AR Transmission	RH	LH	$\leq$ 0.78 dB ($\leq$ 1.74 dB)
AR Reflection	LH	RH	$\leq$ 0.78 dB ($\leq$ 1.74 dB)

1.3 Outline of the Thesis

The thesis is composed of 8 chapters. The current chapter introduced the subject and defined the purpose of the thesis. The second chapter will introduce the concept of CPSS, provide necessary information regarding previous work and define the materials used. In order to understand how a dual band CPSS can function the third chapter is devoted to theory. In the first part of the chapter basic theory is covered and then more specific theory pertaining to the thesis is presented and two different design structures are presented. Chapter 4 briefly deals with the analytical code used for the thesis and chapter 5 focuses on important considerations when implementing the designs in full wave solvers. The result and discussion of the optimized structures are kept in chapter 6. The last two chapters, 7 and 8, contain the summary, conclusions that are made and future work regarding the presented dual band CPSS.

Chapter 2

Circular Polarization Selective Structures

Selectivity in linear polarization has been used for many years with several more or less simple designs such as grids of straight wires [9]. There has not been an equivalent, simple structure, for selection in circular polarization and the feasibility of it ever existing has been a topic of articles in the past [9]. Nowadays, it is known that these structures indeed can be created. In this chapter the basic properties of a circular polarization selective structure will be discussed, followed by previous work in the area.

2.1 Concept of Circular Polarization Selective Structures

CPSSs are constructed in such a way that they have a capability of filtering circularly polarized electromagnetic waves. An ideal CPSS will give lossless transmission for one circular polarization and total reflection for the orthogonal polarization, within the designed frequency range. The two circular polarizations are left-handed- and right-handed- polarization and provide a natural way to categorize the CPSS depending on which type of CP is reflected. These categories are called Left Hand Circular Polarization Selective Structure (LHCPSS) and Right Hand Circular Polarization Selective Structure (RHCPSS), where an ideal LHCPSS reflects an impinging left handed circular polarized wave and vice versa for RHCPSS. Conceptually RHCPSS and LHCPSS are similar and all CPSS in this chapter will now be considered to be LHCPSS unless stated otherwise. The CPSS can be divided in further categories as the reflected and transmitted wave do not need to be of the same polarization as the original impinging waves. Four different CPSSs can theoretically be constructed and these are illustrated in Figure 2.1.

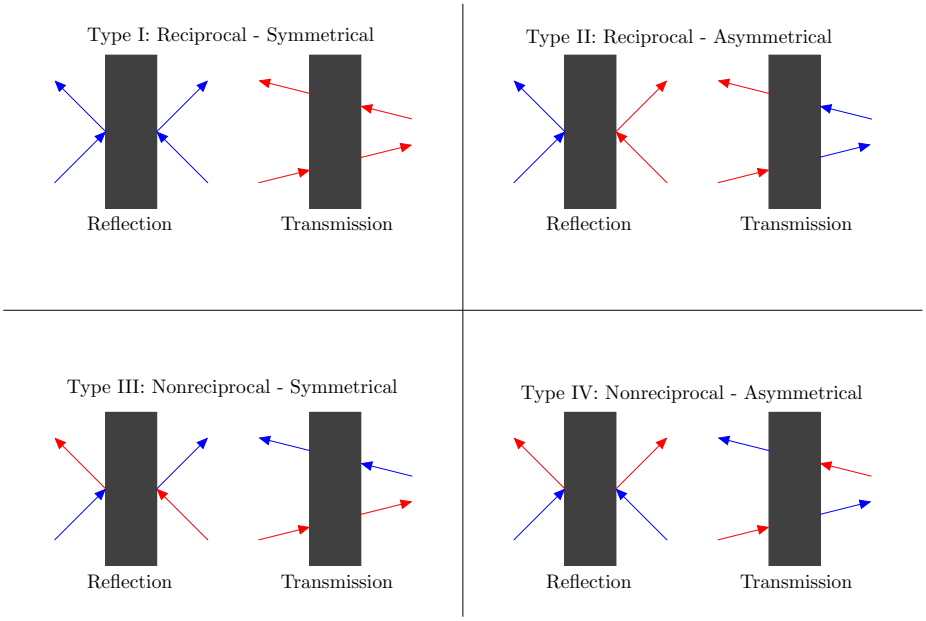

Figure 2.1: Reflection and transmission for different types of circular polarization selective structures. Red is RHCP and blue is for LHCP.

Two types are non reciprocal which implies that they can not be constructed by reciprocal materials but need more exotic materials such as magnetized ferrite crystals and are not interesting for this application [5]. The second type (Reciprocal - Asymmetrical) has not been constructed as far as the author is aware. In this thesis, Reciprocal-Symmetrical selective surfaces are the type to be investigated and henceforth when using the word CPSS it is implied that it is Reciprocal-Symmetrical. It can be shown from theory that a reciprocal-symmetrical CPSS must have the three following properties [10]:

1. "The CP wave reflected by a CPSS will be of the same polarization as the incoming wave"

2. "The wave transmitted by a CPSS will be of the same polarization as the incoming wave"

3. "An infinite CPSS cannot be made of an infinitely thin surface"

2.2 Previous Work

During the last half century there has been interest in creating CPSS and several different concept designs have been presented. Many of these are

reliant upon the resonant behavior of the structure. In more recent years non-resonant structures have become more common. There are advantages and disadvantages with both resonant and non-resonant structures. The major designs will now be presented in a chronological order. In order to provide some insight to the performance of these structures some graphs will be shown. These graphs will show the Return/Insertion Loss which can be viewed as a measurement of losses in reflection and transmission, where 0 dB is perfect reflection/transmission. Moreover the purity of the circular polarization will be shown as Axial Ratio (AR), where 0 dB is a perfectly circular polarized wave. All of these concepts will be defined properly in the theory section (Section 3.2).

The oldest design known was invented in 1966 and consists of Pierrot elements, named after the inventor Robert Pierrot [11]. An individual element can be seen in Figure 2.2 a) and it is in essence a bent metal wire with lengths based on the target wavelength.

The general idea behind this element is that any circularly polarized wave can also be described with a linear basis. The linear components of the electromagnetic wave will only interact with the wires if they are parallel to them. If the propagation direction is in the z-direction and the middle section of the Pierrot element is equal to a quarter wavelength then an electric field currently in the x-direction will be in the y-direction after propagating a quarter wavelength in the z-direction. Currents will be induced on the wire by a wave impinging on it and depending on if the incident electromagnetic wave is polarized left or right handed the induced currents will either add in phase or out of phase and so be either resonant or not. If the structure is resonant the wave will be reflected and transmitted if not. An example of performance for a RHCPSS designed around 10 GHz and with normal incidence can be seen in Figure 2.3. This structure is quite narrowband (1.05 GHz) and although not seen in the figure it has poor performance for other angles of incidence, mainly the AR is affected [12].

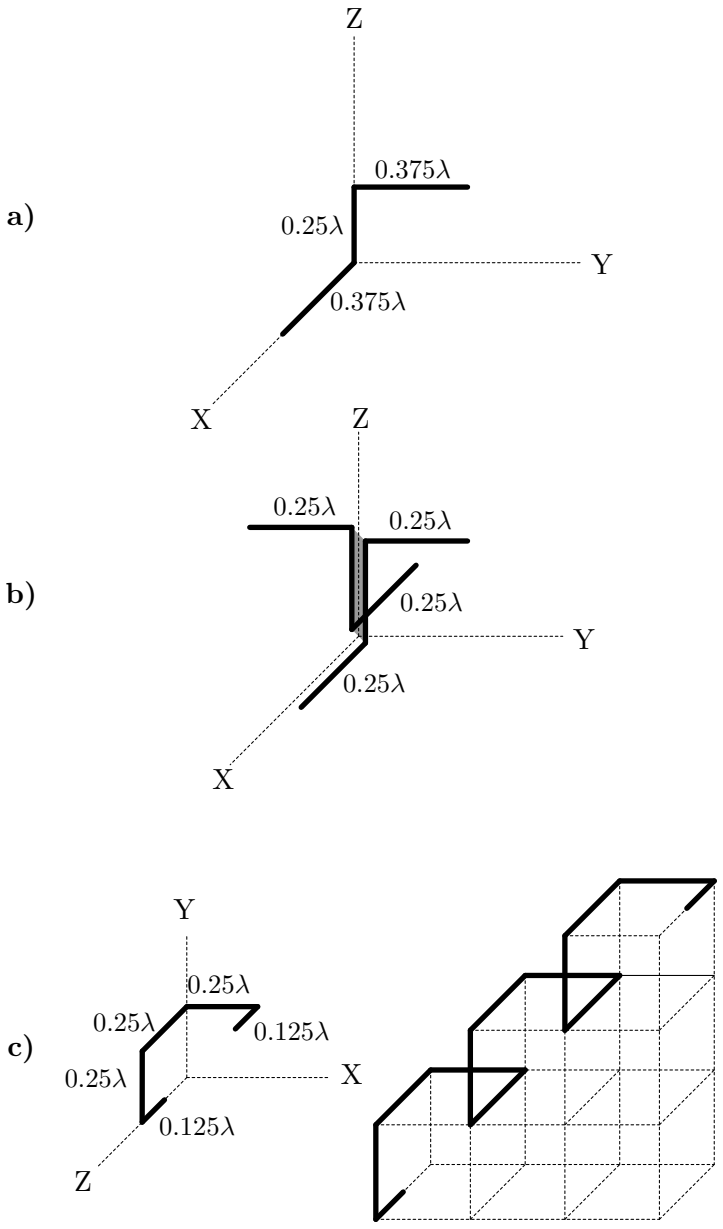

Figure 2.2: Resonant CPSS elements. a) Pierrot, b) Tilston, c) Morin.

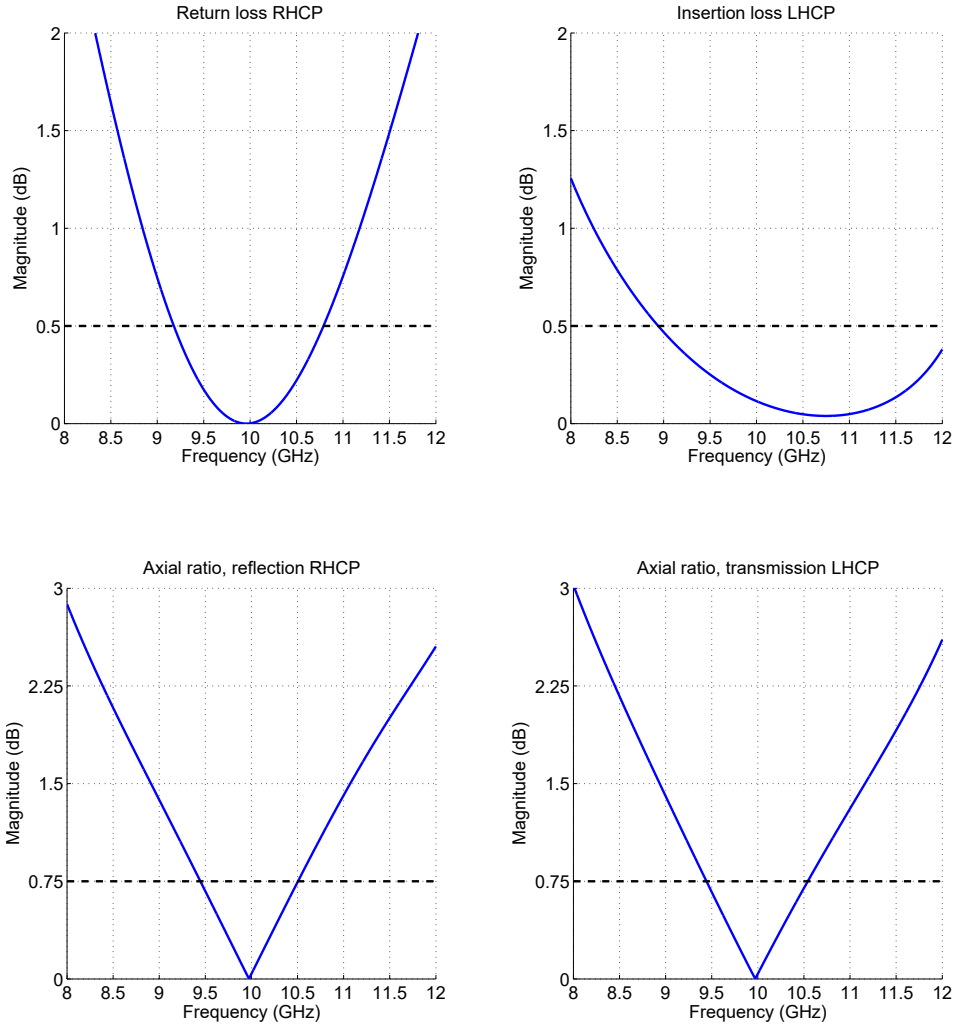

Figure 2.3: Performance of a Pierrot RHCPSS. Taken from [12].

The second design introduced was by Tilston in 1986 [13, 14]. The Tilston cell, like the Pierrot, consists of bent metal wires. The element can be seen in Figure 2.2 b). There are two dipoles and they are connected by a transmission line having $\lambda/4$ physical length and $\lambda/2$ electrical length, the gray area in 2.2 b). Similar to the Pierrot element the linear components of a LHCP electromagnetic wave impinging on this structure will cause the dipoles to create a voltage over the central gap. If these voltages are in phase there will be symmetry around the transmission line. The two dipoles in the Tilston cell will be in resonance for this LHCP wave and thus reflect it. If the input wave is a RHCP wave then the voltages would be out of phase and consequently get reflected. For this design to function

it is of importance that the transmission line has an electrical length of $\lambda/2$ to properly transform to open/short circuit but moreover a physical length of a quarter wavelength in order for the dipoles to pick up the orthogonal components of the electromagnetic wave in phase. In Figure 2.4 the performance of a Tilston RHCPSS can be seen. As with the Pierrot structure, normal incidence with the target frequency 10 GHz is used. The Tilston structure has a bandwidth of 0.83 GHz and has poor performance for oblique incidence [12].

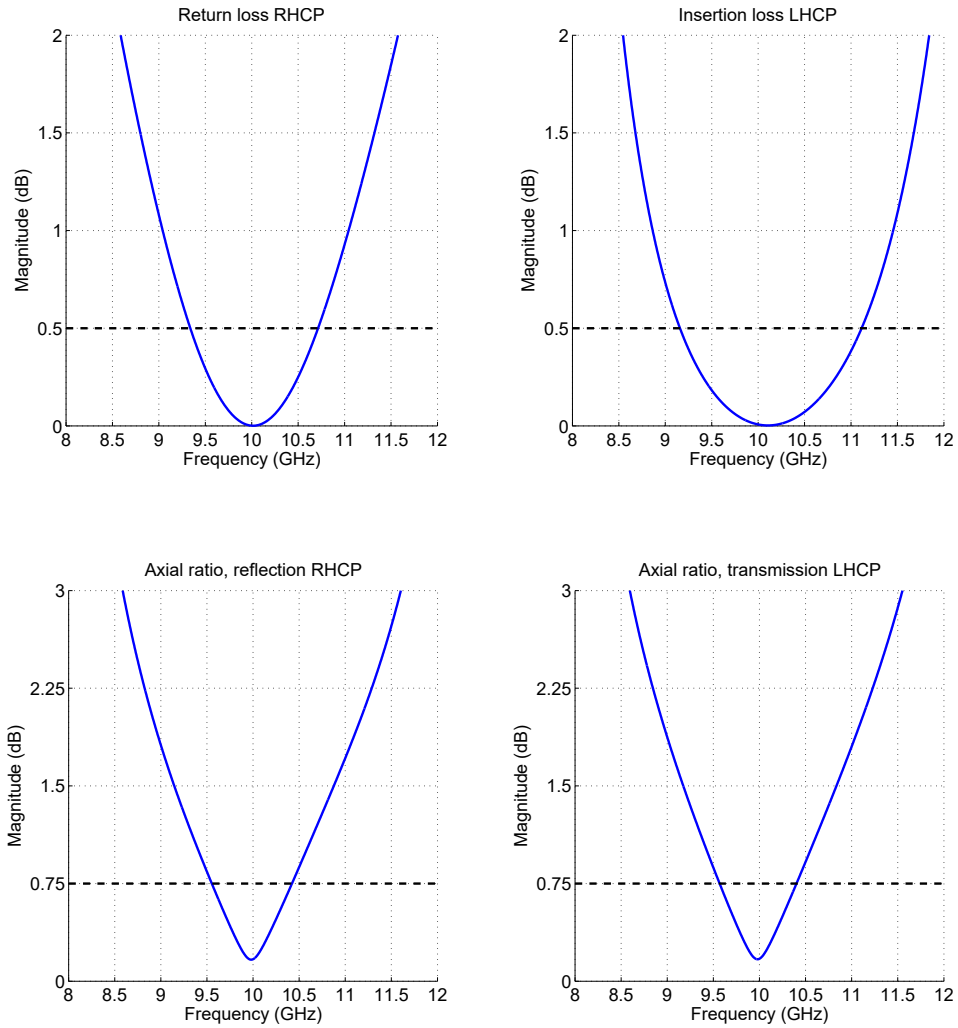

Figure 2.4: Performance of a Tilston RHCPSS. Taken from [12].

In 1994 Morin [15] introduced another design which consists of interconnected metal wires forming a helix structure. The unit cell and the helix structure are visible in Figure 2.2 c). Similarly to the two previous elements the lengths of the wires for the Morin cell are such that the induced currents will add either in phase or out of phase depending on the polarization of the incoming wave. The performance can be seen in Figure 2.5 and is comparable to the other two resonant structures. Bandwidth for the design presented is 1.04 GHz. For oblique incident the performance is not kept and all graphs differ significantly [12].

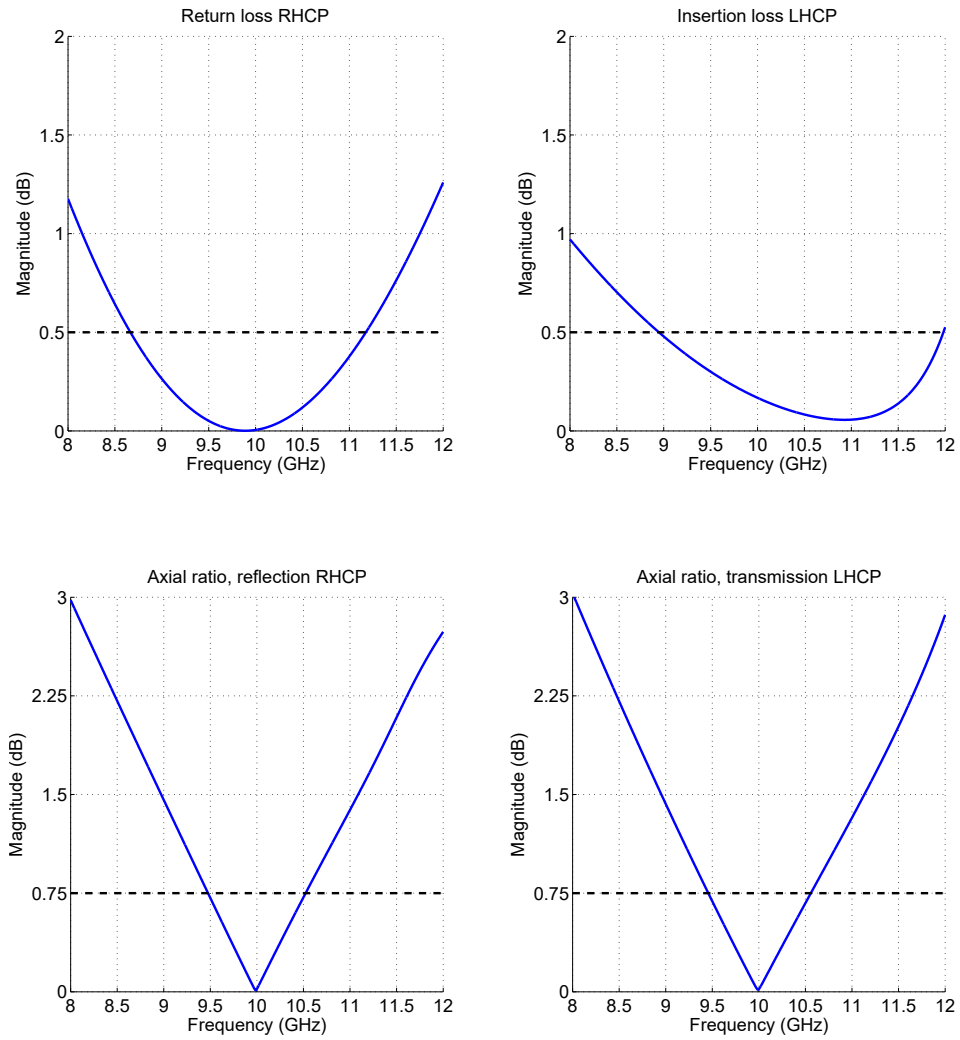

Figure 2.5: Performance of a Morin RHCPSS. Taken from [12].

These three structures presented are the basic CPSS based on resonant behavior. Naturally due to the ingenuity of the human race some variations of these basic elements exists and have been produced over the years but alas not all can be presented here. A common problem with the resonant structures is that the bandwidth is relatively narrow as seen by the three structures and that they are very sensitive to change in the incidence plane. In order to improve the CPSS there has been an effort to investigate other structures that do not depend on a resonant behavior.

One approach is to make a circular to linear polarizer and consequently carry out the separation in linear polarization with a simple strip grid and then convert back to circular polarization [16]. The circular to linear polarizer consists of a number of layers of meander lines not rotated after one another. The number of layers helps improving the axial ratio and this structure has a much better bandwidth than the resonant case [16]. The results are seen in Figure 2.6 and consist of data taken from their simulations [16]. Even though the requirements may not be met completely this structure has flat curves and a possibility of much greater bandwidth than previous resonant structures.

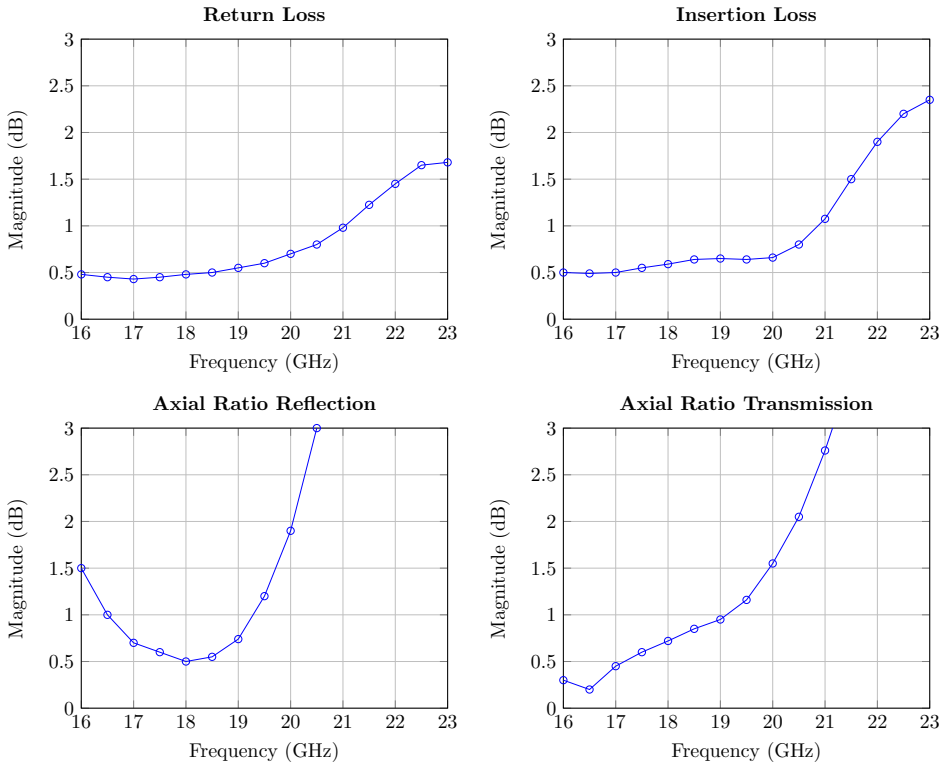

Figure 2.6: Simulated preformance of cascade CPSS, made with data from Joyal and Laurin [16].

This was for the single band scenario but polarizers have also been used to investigate possibility of dual bands. In this case a dual band linear to circular polarization conversion in reflection has been made without use of meander lines [8]. This structure provides conversion from one linear polarization to one handedness of circularly polarized electromagnetic waves in the first frequency band and the orthogonal circular polarization in the second frequency band.

The second approach is different to the others and is what will be used for this thesis. The approach draws inspiration from a way to design circular polarizers with optical metamaterials [17]. One layer will have a certain response in a linear basis and by stacking several layers and tweaking their relative rotation the selectivity in polarization will become clear. More on how this occurs will be described in Section 3.2. Based on this concept and using meander line layers a wide band CPSS has been theorized [6] and physical construction of a similar design is ongoing. The simulation results are significantly better than other designs previously mentioned as

seen in Figure 2.7. The full drawn black line show the target frequencies and target bandwidth of 6 GHz.

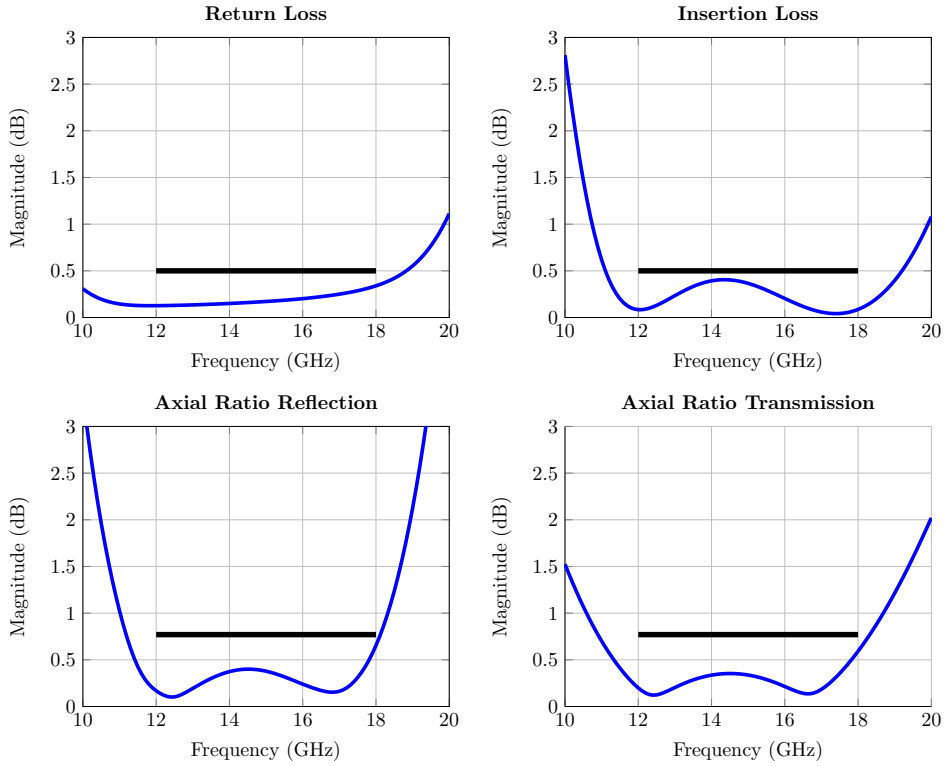

Figure 2.7: Performance of wideband meander design [6].

This kind of design approach can also be used in order to create a dual band CPSS. A very limited introduction can be given by the following brief argument. Consider the elements with a certain response in the x-y basis and a circularly polarized wave moving in the z-direction. In Figure 2.8 a LHCP wave (red) is traveling through the structure with the field aligned the same way for all layers and thus experiencing the structure in some way. The same effect will be had for a higher frequency and when the incoming wave is RHCP. This can be seen by the higher frequency blue line (RHCP) since the vector aligns parallel to the lower frequency red line (LHCP) for all layers.

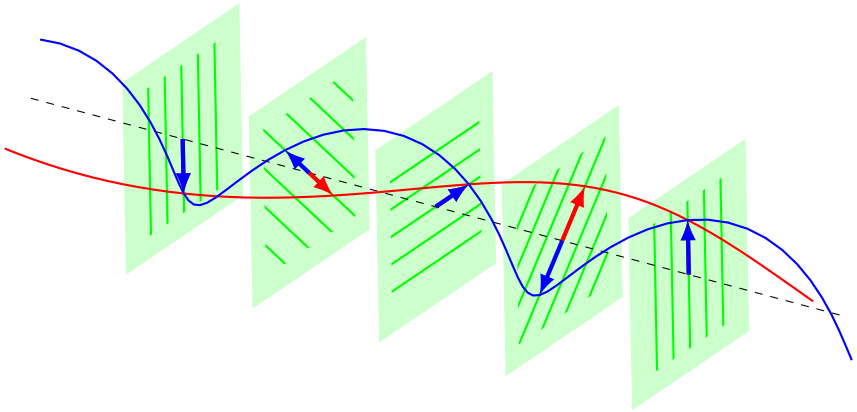

Figure 2.8: Illustration of alignment of different rotations through a structure.

Creating such a dual band structure has not previously been done and what has been presented above is how far the previous work has reached. This thesis will now continue the work on CP selectivity and show the feasibility of a dual band CPSS based on full wave simulations.

2.3 Structure Requirements and Constraints

The requirements that will be set for the dual band CPSS in this thesis is based on previous project description from ESA and used in similar applications [18]. A return loss and insertion loss of less than 0.50 dB is wanted. For AR the requirement is set in Cross Polar Discrimination (XPD) as higher than 27 dB and this is equivalent to an AR of 0.78 dB or less (see (3.45)) This strict requirement of AR is valid for when the proposed design will be used as a curved reflector described earlier (DGR equivalent). When using the CPSS as a diplexer the AR requirement can be relaxed since for this case there are antenna feed designs with good performance [3] to make up for the less strict AR. The relaxed AR requirements used are similar to previous work using an XPD of higher than 20 dB which equates to an AR of 1.74 or less [5].

There are also certain parameters that are fixed and not used in the optimization and those are important to mention. For completeness these are stated here but the labeling of these items are not guaranteed to make sense until Section 5.8 where they are initiated properly. These parameters and their fixed thickness can be seen in Table 2.1.

Table 2.1: Fixed thicknesses for certain parameters used in the thesis.

Parameter Name	Abbreviation	Thickness (mm)
Substrate	t_{subs}	0.1
Metal Printed on Substrate	t_{metal}	0.018
Bonding Layers	t_{bond}	0.05

The proposed structure must be made of feasible and suitable materials for space applications. The materials used have been used in previous projects and are chosen based on their low loss tangent and permittivity as well as low thermal expansion coefficient. The properties can be seen in Table 2.2. The metal parts will all consist of copper.

Table 2.2: Properties of materials used in the thesis.

Parameter Name	Material	ϵ_r	$\tan(\delta)$
Substrate	Dupont AP8515R kapton	3.4	0.003
Distances	Rohacell 31 HF foam	1.04	0.0017
Bonding Layers	Arlon CuClad6250 bonding film	2.32	0.0013

Chapter 3
Theory

This section serves as a brief theory section for the master thesis. It acts as an introduction to the general concepts involved and will not be explained in great detail. Definitions will be introduced as appropriate and expanded upon further when the need arises. The starting point will be Maxwell's equations and from this waves, polarization and how a structure can be treated with S and T matrices shall be described. The confident reader can skip to Section 3.2 where the specific theory for the thesis begins. Much of the information presented here can be found in standard books [19–21].

3.1 General Theory

3.1.1 Maxwell's Equations

The interesting subject of classical electromagnetic theory can be described beautifully by Maxwell's equations. Based on previous empirical and theoretical work (done by Ampere, Faraday and Gauss) Maxwell published the equations in 1873 [22]. In differential form the equations read:

$$\nabla \times \boldsymbol{E} = -\frac{\partial \boldsymbol{B}}{\partial t}, \tag{3.1a}$$

$$\nabla \times \boldsymbol{H} = \boldsymbol{J} + \frac{\partial \boldsymbol{D}}{\partial t}, \tag{3.1b}$$

$$\nabla \cdot \boldsymbol{D} = \rho, \tag{3.1c}$$

$$\nabla \cdot \boldsymbol{B} = 0. \tag{3.1d}$$

In order, the equations are: Faraday's law of induction, Ampère's law including Maxwell's displacement current and the last two equations are Gauss' laws for electric and magnetic fields. Since no magnetic monopole has been found yet the right hand side of Gauss' law for magnetic fields is zero. Sometimes the two last equations are omitted in favor of conservation of charge ($\nabla \cdot \boldsymbol{J} + \frac{\partial \rho}{\partial t} = 0$). The reason for this is simple. Gauss'

equations can be derived from the divergence of Ampère and Faraday's laws in combination with charge conservation and observing that for any vector $\boldsymbol{F}$ the relation $\nabla \cdot (\nabla \times \boldsymbol{F}) = 0$ holds. Throughout this thesis work the SI system of units will be used and the units of the above quantities are:

$\boldsymbol{E}$ is the electric field, in volts per meter (V/m)
$\boldsymbol{H}$ is the magnetic field, in amperes per meter (A/m)
$\boldsymbol{D}$ is the electric flux density, in coulombs per meter squared ($\mathrm{C/m^2}$)
$\boldsymbol{B}$ is the magnetic flux density, in Webers per meter squared (i.e. Tesla) ($\mathrm{Wb/m^2}$)
$\boldsymbol{J}$ is the electric current density, in Amperes per meter squared ($\mathrm{A/m^2}$)
ρ is the volume electric charge density, in Coulombs per meter cubed ($\mathrm{C/m^3}$)

Note that ρ and $\boldsymbol{J}$ are the result of external charges and not any induced polarization, charge or current. They are source terms and when considering problems of electromagnetic wave propagation these are limited to the radiating structure. Far away from the source the simpler source free Maxwell's equations are obtained:

$$\nabla \times \boldsymbol{E} = -\frac{\partial \boldsymbol{B}}{\partial t}, \tag{3.2a}$$

$$\nabla \times \boldsymbol{H} = \frac{\partial \boldsymbol{D}}{\partial t}, \tag{3.2b}$$

$$\nabla \cdot \boldsymbol{D} = 0, \tag{3.2c}$$

$$\nabla \cdot \boldsymbol{B} = 0. \tag{3.2d}$$

These equations are not sufficient to solve the system since there are 6 independent equations but 12 unknowns (4 vectors of three components). The equations needed are the constitutive relations. In vacuum these are,

$$\boldsymbol{D} = \epsilon_0 \boldsymbol{E}, \tag{3.3a}$$

$$\boldsymbol{B} = \mu_0 \boldsymbol{H}, \tag{3.3b}$$

where ϵ_0, μ_0 are the permittivity and permeability of vacuum. The units and values are:

$$\epsilon_0 = 8.854 \cdot 10^{-12} \text{ F/m},$$
$$\mu_0 = 4\pi \cdot 10^{-7} \text{ H/m}.$$

From these quantities we can define other important physical constants. The speed of light and characteristic impedance (in vacuum) as:

$$\mathrm{c}_0 = \frac{1}{\sqrt{\mu_0 \epsilon_0}} = 299792458 \text{ m/s}, \quad \eta_0 = \sqrt{\frac{\mu_0}{\epsilon_0}} = 376.730... \ \Omega.$$

For a linear isotropic, material (3.3) becomes

$$\boldsymbol{D} = \epsilon \boldsymbol{E}, \tag{3.4a}$$

$$\boldsymbol{B} = \mu \boldsymbol{H}, \tag{3.4b}$$

where $\epsilon = \epsilon_0 \epsilon_\mathrm{r} = \epsilon' - \mathrm{j}\epsilon''$ (similar for μ). The losses in materials are often of importance and they can be described by the loss tangent defined as:

$$\tan(\delta) = \frac{\omega \epsilon'' + \sigma}{\omega \epsilon'}. \tag{3.5}$$

Moreover the speed of light and impedance in the material is given by $v = \frac{1}{\sqrt{\mu\epsilon}}$ and $\eta = \sqrt{\frac{\mu}{\epsilon}}$.

3.1.2 Plane Waves and Polarization

The fundamental electromagnetic equations and definitions have been presented. How electromagnetic waves propagate and other, for this thesis, vital definitions will be presented. Consider a source free space described by (3.2). Now taking the curl of (3.2a) and further using the constitutive relations (3.4). The following is obtained,

$$\nabla \times (\nabla \times \boldsymbol{E}(\boldsymbol{r}, t)) = -\mu\epsilon \frac{\partial^2 \boldsymbol{E}(\boldsymbol{r}, t)}{\partial t^2}. \tag{3.6}$$

Since $\nabla \times (\nabla \times A) = \nabla(\nabla \cdot A) - \nabla^2 A$ for any vector, and $\nabla(\nabla \cdot \boldsymbol{E}) = \boldsymbol{0}$ in a source free region,

$$\nabla^2 \boldsymbol{E}(\boldsymbol{r}, t) - \frac{1}{c^2} \frac{\partial^2 \boldsymbol{E}(\boldsymbol{r}, t)}{\partial t^2} = \boldsymbol{0}. \tag{3.7}$$

This is the well-known wave equation which elegantly describes how electromagnetic waves behave. Now consider a wave traveling in the z-direction and no spatial dependence in the x- or y-direction. Waves with these properties are called plane waves. These waves are unphysical (carry infinite energy) but serve as an approximation far away from the source. For this type of waves (3.7) becomes,

$$\left(\frac{\partial^2}{\partial z^2} - \frac{1}{c^2} \frac{\partial^2}{\partial t^2} \right) \boldsymbol{E}(z, t) = \boldsymbol{0}. \tag{3.8}$$

The magnetic field associated with the wave is given by,

$$\boldsymbol{H} = \frac{1}{\eta}\hat{\boldsymbol{z}} \times \boldsymbol{E}. \tag{3.9}$$

The most general solution to the wave equation can be written as forward and backwards traveling fields:

$$\boldsymbol{E}_+(z,t) = \boldsymbol{F}(z-ct), \tag{3.10a}$$
$$\boldsymbol{E}_-(z,t) = \boldsymbol{G}(z+ct), \tag{3.10b}$$

where the +/- subscript indicate forward/backward movement in the z-direction, $\boldsymbol{F}$ and $\boldsymbol{G}$ are arbitrary functions such that $\hat{\boldsymbol{z}} \cdot \boldsymbol{F} = \hat{\boldsymbol{z}} \cdot \boldsymbol{G} = 0$. This solution is quite general, but further restrictions can be imposed to obtain a more familiar set of solutions. We concentrate on only the E-field (H-field is then easily obtained). If the additional assumption of harmonic time dependence is made then the electric field can be written as [19],

$$\boldsymbol{E}(\boldsymbol{r},t) = \boldsymbol{E}(z)e^{\mathrm{j}\omega t}. \tag{3.11}$$

The wave equation can then be separated into space and time dependence. The space dependence is given by the Helmholtz equation,

$$\nabla^2\boldsymbol{E}(\boldsymbol{r}) + k^2\boldsymbol{E}(\boldsymbol{r}) = 0, \tag{3.12}$$

where $k = \frac{\omega}{c}$. With the previous assumption of plane waves the above equation reduces to,

$$\frac{\partial^2\boldsymbol{E}(z)}{\partial z^2} + k^2\boldsymbol{E}(z) = 0. \tag{3.13}$$

The solution to this equation are the forward and backwards fields,

$$\boldsymbol{E}_+(z) = \boldsymbol{E}_{0+}e^{-\mathrm{j}kz}, \tag{3.14a}$$
$$\boldsymbol{E}_-(z) = \boldsymbol{E}_{0-}e^{+\mathrm{j}kz}. \tag{3.14b}$$

As before there can be no component in the z-direction. Besides this requirement $\boldsymbol{E}_{0\pm}$ are arbitrary constant vectors.
For now consider only forward going waves. Any such plane wave can be described as obtained,

$$\boldsymbol{E}_+(z,t) = \boldsymbol{E}_{0+}e^{\mathrm{j}\omega t-\mathrm{j}kz} = (\hat{\boldsymbol{x}}A + \hat{\boldsymbol{y}}B)e^{\mathrm{j}\omega t-\mathrm{j}kz}. \tag{3.15}$$

The wave has components in x- and y- direction and from this the polarization state can be discussed. The polarization is determined by the direction

of the real value of the time-varying field, $\mathrm{Re}(\boldsymbol{E}(\boldsymbol{r},t))$. Using trigonometric relations the polarization ellipse can be obtained,

$$\frac{\mathrm{Re}(E_{\mathrm{x}}^2)}{|A^2|}+\frac{\mathrm{Re}(E_{\mathrm{y}}^2)}{|B^2|}-2\cos\phi\frac{\mathrm{Re}(E_{\mathrm{x}})\mathrm{Re}(E_{\mathrm{y}})}{|A||B|}=\sin^2\phi, \tag{3.16}$$

where $\phi=\arg(A)-\arg(B)$. It is clear that if $\phi=\{0,\pi\}$ then the polarization state is a line as equation 3.16 reduces to $\mathrm{Re}(E_{\mathrm{y}})=\pm\frac{|A|}{|B|}\mathrm{Re}(E_{\mathrm{x}})$. This corresponds to a linear polarized wave. If ϕ is $\pm\pi/2$ and $|A|=|B|$ then the polarization ellipse reduces to a circle and so describes circular polarization. As seen circular polarization and linear polarization are special cases of (3.16) and the general polarization state is elliptical. From equation 3.16 the general state can be drawn (Figure 3.1).

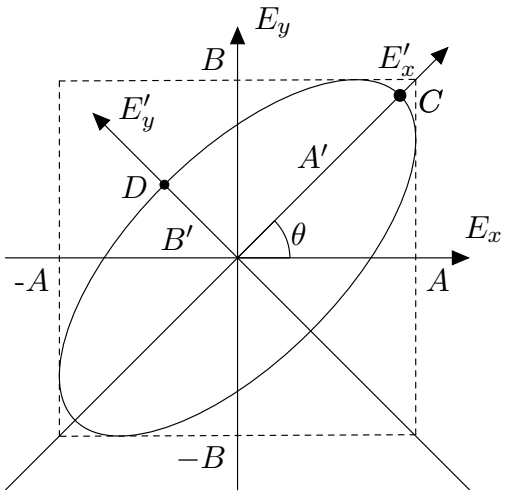

Figure 3.1: General polarization ellipse.

The tilt angle θ in Figure 3.1 is related to ϕ by,

$$\tan 2\theta=\frac{2AB}{A^2-B^2}\cos\phi. \tag{3.17}$$

An ellipse has a major and a minor axis. The ellipse is a circle if the ratio between the axes are one. The semi-axes of the ellipse in Figure 3.1 are given by the following expressions:

$$A'=\sqrt{\frac{1}{2}(A^2+B^2)+\frac{s}{2}\sqrt{(A^2-B^2)^2+4A^2B^2\cos(\phi)}}, \tag{3.18a}$$

$$B'=\sqrt{\frac{1}{2}(A^2+B^2)-\frac{s}{2}\sqrt{(A^2-B^2)^2+4A^2B^2\cos(\phi)}}, \tag{3.18b}$$

where $s = \text{sign}(A - B)$.

In this thesis circular polarization will be used extensively and the definition from Institute of Electrical and Electronics Engineers (IEEE) [23] will be used. The definition can be presented as follows, consider an orthonormal right-handed basis, fixed in space, $\hat{\boldsymbol{a}}, \hat{\boldsymbol{b}}, \hat{\boldsymbol{c}}$. If the wave is traveling in the $\hat{\boldsymbol{c}}$-direction and one observes the ab-plane from the tip of the $\hat{\boldsymbol{c}}$ unit vector and the electric field vector rotates in a mathematical positive direction then the wave is right circular polarized. Conversely the wave is left circular polarized if the rotation direction is negative. This is illustrated in Figure 3.2 where the circles obtained from plotting the tip of the electric field vector for all times. The direction of movement of the tip is indicated by the arrows on the circles.

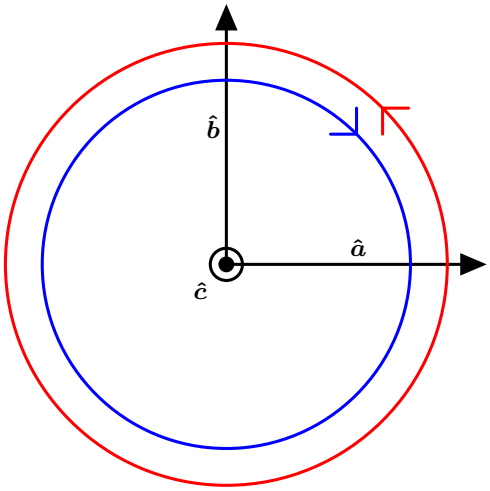

Figure 3.2: Circles traced by the electric field vector, red circle is right handed and blue circle is left handed.

In short this gives the following,

$$\begin{aligned}
\boldsymbol{E}(z) &= (\hat{\boldsymbol{x}} - \mathrm{j}\hat{\boldsymbol{y}})e^{-\mathrm{j}kz} && \text{Right-polarized, forward moving,} \\
\boldsymbol{E}(z) &= (\hat{\boldsymbol{x}} + \mathrm{j}\hat{\boldsymbol{y}})e^{-\mathrm{j}kz} && \text{Left-polarized, forward moving,} \\
\boldsymbol{E}(z) &= (\hat{\boldsymbol{x}} - \mathrm{j}\hat{\boldsymbol{y}})e^{\mathrm{j}kz} && \text{Left-polarized, backward moving,} \\
\boldsymbol{E}(z) &= (\hat{\boldsymbol{x}} + \mathrm{j}\hat{\boldsymbol{y}})e^{\mathrm{j}kz} && \text{Right-polarized, backward moving.}
\end{aligned}$$

Keep in mind that this also means that a right circular wave traces a left handed helix in space and similarly a left circular wave traces a right handed

helix. Throughout this work circular polarization is of great importance, and a measure of the purity of the circular polarization is needed. A good quantity of this is the axial ratio.

The axial ratio is defined by the IEEE as "The ratio of the major to minor axes of a polarization ellipse" and can be computed as [24],

$$\mathrm{AR} = \max\Big(\frac{A'}{B'}, \frac{B'}{A'}\Big). \tag{3.19}$$

Both linear and circular polarization can serve as a basis and conversion between linear and circular polarization for a wave propagating in positive z-direction can be summarized by the following matrices

$$\begin{pmatrix} E^{\mathrm{R}} \\ E^{\mathrm{L}} \end{pmatrix} = \frac{1}{\sqrt{2}} \begin{pmatrix} 1 & \mathrm{j} \\ 1 & -\mathrm{j} \end{pmatrix} \begin{pmatrix} E^{\mathrm{X}} \\ E^{\mathrm{Y}} \end{pmatrix}, \tag{3.20}$$

$$\begin{pmatrix} E^{\mathrm{X}} \\ E^{\mathrm{Y}} \end{pmatrix} = \frac{1}{\sqrt{2}} \begin{pmatrix} 1 & 1 \\ -\mathrm{j} & \mathrm{j} \end{pmatrix} \begin{pmatrix} E^{\mathrm{R}} \\ E^{\mathrm{L}} \end{pmatrix}, \tag{3.21}$$

where R stands for right polarized and L for left polarized.

3.1.3 Reflection and Transmission

In the previous sections the polarization of electromagnetic waves has been described and now propagation of these waves will be discussed. For the sake of simplicity the electromagnetic wave is propagating in the z-direction and is linearly polarized with the E-field in the x-direction. The wave is propagating in a lossless and isotropic dielectric (ϵ and μ constant). After some rearranging of equations 3.9 and 3.14 the fields can be related to the forwards and backwards electric fields through

$$\begin{pmatrix} E \\ H \end{pmatrix} = \begin{pmatrix} 1 & 1 \\ 1/\eta & -1/\eta \end{pmatrix} \begin{pmatrix} E_+ \\ E_- \end{pmatrix}. \tag{3.22}$$

The impedance and the reflection coefficient at position z are as follows,

$$Z(z) = \frac{E(z)}{H(z)} = \eta \frac{Z(0) - \mathrm{j}\eta \tan(kz)}{\eta - \mathrm{j}Z(0)\tan(kz)}, \tag{3.23}$$

$$\Gamma(z) = \frac{E_-(z)}{E_+(z)} = \Gamma(0)e^{2\mathrm{j}kz}. \tag{3.24}$$

The relation between the reflection coefficient and impedance, at the position z, is given by

$$Z(z) = \eta \frac{1 + \Gamma(z)}{1 - \Gamma(z)}, \tag{3.25a}$$

$$\Gamma(z) = \frac{Z(z) - \eta}{Z(z) + \eta}. \tag{3.25b}$$

3.1.4 Transfer and Scattering matrices

The quantities E_+, E_-, Γ are easily propagated (equation 3.14, 3.24) whereas E, H, Z are not. They do however have another advantage and that is interface crossings, where E, H, Z are all continuous at normal incidence with respect to an interface. Consider an interface, the total fields on either side can then be written as,

$$\begin{pmatrix} E_2 \\ H_2 \end{pmatrix} = \begin{pmatrix} 1 & 0 \\ 0 & 1 \end{pmatrix} \begin{pmatrix} E_1 \\ H_1 \end{pmatrix}. \tag{3.26}$$

For this application the more interesting forward and backwards electric fields are

$$\begin{pmatrix} 1 & 1 \\ 1/\eta_2 & -1/\eta_2 \end{pmatrix} \begin{pmatrix} E_{2+} \\ E_{2-} \end{pmatrix} = \begin{pmatrix} 1 & 1 \\ 1/\eta_1 & -1/\eta_1 \end{pmatrix} \begin{pmatrix} E_{1+} \\ E_{1-} \end{pmatrix}, \tag{3.27}$$

$$\begin{pmatrix} E_{2+} \\ E_{2-} \end{pmatrix} = \frac{1}{2} \begin{pmatrix} 1 & \eta_2 \\ 1 & -\eta_2 \end{pmatrix} \begin{pmatrix} 1 & 1 \\ 1/\eta_1 & -1/\eta_1 \end{pmatrix} \begin{pmatrix} E_{1+} \\ E_{1-} \end{pmatrix}. \tag{3.28}$$

Which simplifies to,

$$\begin{pmatrix} E_{2+} \\ E_{2-} \end{pmatrix} = \frac{1}{\tau} \begin{pmatrix} 1 & \rho \\ \rho & 1 \end{pmatrix} \begin{pmatrix} E_{1+} \\ E_{1-} \end{pmatrix}, \tag{3.29}$$

where,

$$\rho = \frac{\eta_1 - \eta_2}{\eta_1 + \eta_2}, \tag{3.30a}$$

$$\tau = \frac{2\eta_1}{\eta_1 + \eta_2}, \tag{3.30b}$$

are the reflection and transmission coefficients respectively. The matrix in (3.29) is called matching matrix. Now the forward and backward fields of a slab of length l can easily be written as,

$$\begin{pmatrix} E_{1+} \\ E_{1-} \end{pmatrix} = \frac{1}{\tau_1} \begin{pmatrix} 1 & \rho_1 \\ \rho_1 & 1 \end{pmatrix} \begin{pmatrix} e^{\mathrm{j}k_1 l_1} & 0 \\ 0 & e^{-\mathrm{j}k_1 l_1} \end{pmatrix} \frac{1}{\tau_2} \begin{pmatrix} 1 & \rho_2 \\ \rho_2 & 1 \end{pmatrix} \begin{pmatrix} E_{2+} \\ E_{2-} \end{pmatrix}. \tag{3.31}$$

This can easily be extended for several slabs. Writing the expression above as,

$$\begin{pmatrix} E_{1+} \\ E_{1-} \end{pmatrix} = \begin{pmatrix} T_{11} & T_{12} \\ T_{21} & T_{22} \end{pmatrix} \begin{pmatrix} E_{2+} \\ E_{2-} \end{pmatrix}, \tag{3.32}$$

the transfer matrix is apparent. The transfer matrix (T-matrix) is very convenient in computations since propagating the related fields are easy. However, it is often desired to relate the incoming field to the outgoing.

By converting the transfer matrix, to relate the incident and the scattered fields to each other, the scattering matrix is obtained,

$$\begin{pmatrix} E_{1-} \\ E_{2+} \end{pmatrix} = \begin{pmatrix} \Gamma_{aa} & \mathcal{T}_{ab} \\ \mathcal{T}_{ba} & \Gamma_{bb} \end{pmatrix} \begin{pmatrix} E_{1+} \\ E_{2-} \end{pmatrix}. \tag{3.33}$$

This is a very brief introduction to the scattering and transfer matrices in the simplest case. This can be expanded to more complex structures, dielectrics and angles of incident. Treating isotropic dielectric/magnetic materials only require a small modification to the equations, the wave number k. However, the purpose of this section is not to dwell too deeply in this theory. The general result for a bianisotropic slab will be stated. Similar to the above matrices the slab can be described by the so called ABCD-matrix [20].

$$\begin{pmatrix} \boldsymbol{E}(z_1) \\ \boldsymbol{H}(z_1) \times \hat{\boldsymbol{z}} \end{pmatrix} = \begin{pmatrix} \boldsymbol{A} & \boldsymbol{B} \\ \boldsymbol{C} & \boldsymbol{D} \end{pmatrix} \begin{pmatrix} \boldsymbol{E}(z_2) \\ \boldsymbol{H}(z_2) \times \hat{\boldsymbol{z}} \end{pmatrix}. \tag{3.34}$$

In the surrounding free space using the relation $\boldsymbol{E}_{\pm} = \pm \boldsymbol{Z}_0 \cdot (\boldsymbol{H}_{\pm} \times \hat{\boldsymbol{z}})$ implies that

$$\begin{pmatrix} (\boldsymbol{I} + \boldsymbol{r}) \cdot \boldsymbol{E}_{1+} \\ \boldsymbol{Z}_0^{-1} \cdot (\boldsymbol{I} - \boldsymbol{r}) \cdot \boldsymbol{E}_{1+} \end{pmatrix} = \begin{pmatrix} \mathbf{A} & \boldsymbol{B} \\ \mathbf{C} & \boldsymbol{D} \end{pmatrix} \cdot \begin{pmatrix} \mathbf{t} \cdot \boldsymbol{E}_{1+} \\ \mathbf{Z}_0^{-1} \cdot \mathbf{t} \cdot \boldsymbol{E}_{1+,} \end{pmatrix}, \tag{3.35}$$

where $\mathbf{Z_0}$ is the wave impedance dyadic. The reflection and transmission dyadics can be solved for [25],

$$\boldsymbol{r} = (\mathbf{A} + \boldsymbol{B} \cdot \mathbf{Z}_0^{-1} - \mathbf{Z}_0 \cdot \mathbf{C} - \mathbf{Z}_0 \cdot \boldsymbol{D} \cdot \mathbf{Z}_0^{-1}) \cdot (\mathbf{A} + \boldsymbol{B} \cdot \mathbf{Z}_0^{-1} + \mathbf{Z}_0 \cdot \mathbf{C} + \mathbf{Z}_0 \cdot \boldsymbol{D} \cdot \mathbf{Z}_0^{-1})^{-1}, \tag{3.36a}$$

$$\mathbf{t} = 2(\mathbf{A} + \boldsymbol{B} \cdot \mathbf{Z}_0^{-1} + \mathbf{Z}_0 \cdot \mathbf{C} + \mathbf{Z_0} \cdot \boldsymbol{D} \cdot \mathbf{Z}_0^{-1})^{-1}. \tag{3.36b}$$

How materials actually scatter light is a very interesting subject but require much more theoretical background. The interested reader can read more about this subject in Basic Theory of Electromagnetic Scattering [26]. For this thesis it is sufficient to accept that the above scattering and transfer matrices can be constructed for the structures of interest. With the scattering matrix introduced the plausibility of a dual band CPSS can soon be introduced.

3.2 Specific Theory

The theoretical framework has now been presented and we are ready to discuss how to describe circular polarization selective structures by using the scattering and transfer matrices.

3.2.1 Ideal Scattering Matrices

Consider a structure interacting with electromagnetic waves. The structure is infinite in the xy-plane with infinitesimal thickness in the z-direction. Electromagnetic waves are incident from both sides of this structure ($z > 0$ and $z < 0$). These two excitation planes are labeled port 1 and port 2. The incident waves are right hand circular polarized and left hand circular polarized. With previous notion of the scattering matrix the outgoing waves from this surface can be described through the scattering matrix (subscript indicates port number, superscript indicates polarization),

$$S^{\mathrm{CP}} = \begin{pmatrix} S_{11}^{RR} & S_{11}^{RL} & S_{12}^{RR} & S_{12}^{RL} \\ S_{11}^{LR} & S_{11}^{LL} & S_{12}^{LR} & S_{12}^{LL} \\ S_{21}^{RR} & S_{21}^{RL} & S_{22}^{RR} & S_{22}^{RL} \\ S_{21}^{LR} & S_{21}^{LL} & S_{22}^{LR} & S_{22}^{LL} \end{pmatrix}, \quad \text{where} \quad S_{ij}^{kl} = \frac{E_i^k}{E_j^l}. \tag{3.37}$$

A CPSS is a structure which has selectivity in which polarization it reflects. As previously stated this structure will reflect left handed circular polarization. Thus the ideal LHCPSS can be represented with the following S matrix,

$$S_{\mathrm{Ideal}}^{\mathrm{LHCPSS}} = \begin{pmatrix} 0 & 0 & e^{-\mathrm{j}\phi_t} & 0 \\ 0 & e^{-\mathrm{j}\phi_r} & 0 & 0 \\ e^{-\mathrm{j}\phi_t} & 0 & 0 & 0 \\ 0 & 0 & 0 & e^{-\mathrm{j}\phi_r} \end{pmatrix}, \tag{3.38}$$

where ϕ_t and ϕ_r are the phases of the transmission and reflection coefficients, respectively. Similarly for an RHCPSS,

$$S_{\mathrm{Ideal}}^{\mathrm{RHCPSS}} = \begin{pmatrix} e^{-\mathrm{j}\phi_r} & 0 & 0 & 0 \\ 0 & 0 & 0 & e^{-\mathrm{j}\phi_t} \\ 0 & 0 & e^{-\mathrm{j}\phi_r} & 0 \\ 0 & e^{-\mathrm{j}\phi_t} & 0 & 0 \end{pmatrix}. \tag{3.39}$$

The goal of this thesis is to create a structure that is LHCPSS for a certain frequency, f_1, and a RHCPSS for another frequency, f_2. From the scattering matrix (3.37) certain valuable quantities can be computed. From IEEE definitions [24],

Return Loss

Definition: "The ratio of incident to reflected power at a reference plane of a network."

$$\mathrm{RL} = -20\log_{10}(|S_{mm}^{\mathrm{kl}}|). \tag{3.40}$$

For this thesis only $k = l$ is of interest.

Insertion Loss

Definition: "Resulting from the insertion of a transducer in a transmission path or system: the ratio of (1) the power delivered to that part of the system following the transducer, before insertion of the transducer, to (2) the power delivered to that same part of the system after insertion of the transducer. It is generally expressed as a ratio in decibels (dB)."

$$\mathrm{IL} = -20\log_{10}(|S_{mn}^{\mathrm{kk}}|), \quad m \neq n. \tag{3.41}$$

Axial Ratio

The definition of AR has already been covered. For the sake of completeness it is stated once more.
Definition:"The ratio of the major to minor axes of a polarization ellipse"
The axial ratio can be expressed with the scattering parameters as,

$$\mathrm{AR} = 20\log_{10}\left(\frac{\sqrt{\sqrt{1+\alpha}+1}}{\sqrt{\sqrt{1+\alpha}-1}}\right), \tag{3.42}$$

where,

$$\alpha = \frac{1}{4}\left(\left|\frac{S_{mn}^{\mathrm{kl}}}{S_{mn}^{\mathrm{ll}}}\right| - \left|\frac{S_{mn}^{\mathrm{ll}}}{S_{mn}^{\mathrm{kl}}}\right|\right)^2. \tag{3.43}$$

These expressions are obtained by expressing the polarization ellipse semi-axes, A' and B', with Stokes parameters and simplifying [21]. There is another widely used term to measure polarization purity, XPD. The XPD is defined as the ratio of the average received power of the desired polarization (co-polarized) relative to the average received power of the undesired one (cross-polarized) and can be computed as [27]:

$$\mathrm{XPD} = 20\log_{10}\left(\left|\frac{S_{mn}^{kk}}{S_{mn}^{kl}}\right|\right), k \neq l. \tag{3.44}$$

Only AR will be used in this thesis but for comparison with other work the relation between AR and XPD is given by the following conversion, where the AR and XPD are given in dB,

$$\mathrm{XPD} = 20\log_{10}\left(\frac{\mathrm{AR}+1}{\mathrm{AR}-1}\right), \tag{3.45a}$$

$$\mathrm{AR} = 20\log_{10}\left(\frac{10^{\frac{\mathrm{XPD}}{20}}+1}{10^{\frac{\mathrm{XPD}}{20}}-1}\right). \tag{3.45b}$$

These are the definitions needed to easily characterize the proposed structures.

3.2.2 Linear to Circular Polarization Representation

Before further direct calculations of the S-matrices the two port conversion between linear and circular polarization must be described. The reason for this is that the structure will consist of multiple layers of a structure which has a certain response in linear polarization. When multiple layers are stacked together it will soon be clear that a selectivity in circular polarization appears.

The conversion between linear to circular polarization is given by (3.20). However, this is for propagation in the z-direction. The outgoing waves from the ports are incident on the structure and thus travel in both positive and negative z-direction depending on the port. Since the direction of propagation is different the following conversion matrices are needed:

$$\begin{pmatrix} E_1^{\mathrm{R}} \\ E_1^{\mathrm{L}} \end{pmatrix} = \frac{1}{\sqrt{2}} \begin{pmatrix} 1 & -\mathrm{j} \\ 1 & \mathrm{j} \end{pmatrix} \begin{pmatrix} E_1^{\mathrm{X}} \\ E_1^{\mathrm{Y}} \end{pmatrix}, \tag{3.46}$$

$$\begin{pmatrix} E_2^{\mathrm{R}} \\ E_2^{\mathrm{L}} \end{pmatrix} = \frac{1}{\sqrt{2}} \begin{pmatrix} 1 & \mathrm{j} \\ 1 & -\mathrm{j} \end{pmatrix} \begin{pmatrix} E_2^{\mathrm{X}} \\ E_2^{\mathrm{Y}} \end{pmatrix}. \tag{3.47}$$

The scattered fields in linear and circular representation are then given by,

$$\begin{pmatrix} E_1^{\mathrm{R}} \\ E_1^{\mathrm{L}} \\ E_2^{\mathrm{R}} \\ E_2^{\mathrm{L}} \end{pmatrix} = \frac{1}{\sqrt{2}} \begin{pmatrix} 1 & -\mathrm{j} & 0 & 0 \\ 1 & \mathrm{j} & 0 & 0 \\ 0 & 0 & 1 & \mathrm{j} \\ 0 & 0 & 1 & -\mathrm{j} \end{pmatrix} \begin{pmatrix} E_1^{\mathrm{X}} \\ E_1^{\mathrm{Y}} \\ E_2^{\mathrm{X}} \\ E_2^{\mathrm{Y}} \end{pmatrix} = P \cdot \begin{pmatrix} E_1^{\mathrm{X}} \\ E_1^{\mathrm{Y}} \\ E_2^{\mathrm{X}} \\ E_2^{\mathrm{Y}} \end{pmatrix}. \tag{3.48}$$

With (3.48) a conversion between linear and circular polarization for the scattering matrix can be done. Due to the convenient block matrix form the inverse is simply,

$$P^{-1} = \frac{1}{\sqrt{2}} \begin{pmatrix} 1 & 1 & 0 & 0 \\ \mathrm{j} & -\mathrm{j} & 0 & 0 \\ 0 & 0 & 1 & 1 \\ 0 & 0 & -\mathrm{j} & \mathrm{j} \end{pmatrix}. \tag{3.49}$$

3.2.3 Single Layer

The complete structure will consist of multiple linearly polarized elements stacked after one another. One reason for this will become clear after this subsection. Continue to consider the single layers to be infinitesimally thin and separated by a distance, d. Each layer can be rotated in the $xy-$plane

by an angle ϕ. If aligned with the coordinate system ($\phi = 0$) the scattering matrix for these elements in linear polarization are,

$$S(\phi = 0)^{\mathrm{LP}}_{\mathrm{Linear}} = \begin{pmatrix} r_{\mathrm{x}} & 0 & t_{\mathrm{x}} & 0 \\ 0 & r_{\mathrm{y}} & 0 & t_{\mathrm{y}} \\ t_{\mathrm{x}} & 0 & r_{\mathrm{x}} & 0 \\ 0 & t_{\mathrm{y}} & 0 & r_{\mathrm{y}} \end{pmatrix}. \tag{3.50}$$

Only co-polarized transmission and reflection are present. For clarification, the subscript linear indicates that it is a linearly polarized element and the superscript indicates in which basis the matrix is presented. Each layer will be rotated an angle ϕ, in the xy-plane, compared to the previous layer and the scattering matrix for such an arbitrary rotated element will then be the result of a simple rotation described by the following transformation,

$$\begin{aligned} S(\phi)^{\mathrm{LP}}_{\mathrm{Linear}} = & \begin{pmatrix} \cos\phi & \sin\phi & 0 & 0 \\ -\sin\phi & \cos\phi & 0 & 0 \\ 0 & 0 & \cos\phi & \sin\phi \\ 0 & 0 & -\sin\phi & \cos\phi \end{pmatrix}. \\ & \begin{pmatrix} r_{\mathrm{x}} & 0 & t_{\mathrm{x}} & 0 \\ 0 & r_{\mathrm{y}} & 0 & t_{\mathrm{y}} \\ t_{\mathrm{x}} & 0 & r_{\mathrm{x}} & 0 \\ 0 & t_{\mathrm{y}} & 0 & r_{\mathrm{y}} \end{pmatrix} \begin{pmatrix} \cos\phi & -\sin\phi & 0 & 0 \\ \sin\phi & \cos\phi & 0 & 0 \\ 0 & 0 & \cos\phi & -\sin\phi \\ 0 & 0 & \sin\phi & \cos\phi \end{pmatrix}. \end{aligned} \tag{3.51}$$

After observing that $t_{x,y} = 1 + r_{x,y}$ (equation 3.30) and carrying out the multiplication the result is,

$$\begin{aligned} S^{\mathrm{LP}}_{\mathrm{Linear}} = & r_{\mathrm{x}} \begin{pmatrix} \cos^2\phi & -\cos\phi\sin\phi & \cos^2\phi & -\cos\phi\sin\phi \\ -\cos\phi\sin\phi & \sin^2\phi & -\cos\phi\sin\phi & \sin^2\phi \\ \cos^2\phi & -\cos\phi\sin\phi & \cos^2\phi & -\cos\phi\sin\phi \\ -\cos\phi\sin\phi & \sin^2\phi & -\cos\phi\sin\phi & \sin^2\phi \end{pmatrix} \\ & + r_{\mathrm{y}} \begin{pmatrix} \sin^2\phi & \cos\phi\sin\phi & \cos^2\phi & \cos\phi\sin\phi \\ \cos\phi\sin\phi & \cos^2\phi & \cos\phi\sin\phi & \cos^2\phi \\ \sin^2\phi & \cos\phi\sin\phi & \sin^2\phi & \cos\phi\sin\phi \\ \cos\phi\sin\phi & \cos^2\phi & \cos\phi\sin\phi & \cos^2\phi \end{pmatrix} + \begin{pmatrix} 0 & 0 & 1 & 0 \\ 0 & 0 & 0 & 1 \\ 1 & 0 & 0 & 0 \\ 0 & 1 & 0 & 0 \end{pmatrix}. \end{aligned} \tag{3.52}$$

Now with use of equation 3.48 and 3.49 conversion to circular polarization is simple,

$$S^{\mathrm{CP}}_{\mathrm{Linear}} = P S^{\mathrm{LP}}_{\mathrm{Linear}} P^{-1} =$$
$$\frac{1}{2}\begin{pmatrix} 1 & -\mathrm{j} & 0 & 0 \\ 1 & \mathrm{j} & 0 & 0 \\ 0 & 0 & 1 & \mathrm{j} \\ 0 & 0 & 1 & -\mathrm{j} \end{pmatrix} \cdot \left[\begin{pmatrix} \cos^2\phi & -\cos\phi\sin\phi & \cos^2\phi & -\cos\phi\sin\phi \\ -\cos\phi\sin\phi & \sin^2\phi & -\cos\phi\sin\phi & \sin^2\phi \\ \cos^2\phi & -\cos\phi\sin\phi & \cos^2\phi & -\cos\phi\sin\phi \\ -\cos\phi\sin\phi & \sin^2\phi & -\cos\phi\sin\phi & \sin^2\phi \end{pmatrix} \right.$$
$$\left. + r_{\mathrm{y}} \begin{pmatrix} \sin^2\phi & \cos\phi\sin\phi & \cos^2\phi & \cos\phi\sin\phi \\ \cos\phi\sin\phi & \cos^2\phi & \cos\phi\sin\phi & \cos^2\phi \\ \sin^2\phi & \cos\phi\sin\phi & \sin^2\phi & \cos\phi\sin\phi \\ \cos\phi\sin\phi & \cos^2\phi & \cos\phi\sin\phi & \cos^2\phi \end{pmatrix} + \begin{pmatrix} 0 & 0 & 1 & 0 \\ 0 & 0 & 0 & 1 \\ 1 & 0 & 0 & 0 \\ 0 & 1 & 0 & 0 \end{pmatrix} \right]$$
$$\cdot \begin{pmatrix} 1 & 1 & 0 & 0 \\ \mathrm{j} & -\mathrm{j} & 0 & 0 \\ 0 & 0 & 1 & 1 \\ 0 & 0 & -\mathrm{j} & \mathrm{j} \end{pmatrix}. \quad (3.53)$$

After some rearranging the more manageable expression is obtained.

$$S^{\mathrm{CP}}_{\mathrm{Linear}} = \frac{r_{\mathrm{x}} + r_{\mathrm{y}}}{2} \begin{pmatrix} 0 & 1 & 1 & 0 \\ 1 & 0 & 0 & 1 \\ 1 & 0 & 0 & 1 \\ 0 & 1 & 1 & 0 \end{pmatrix}$$
$$+ \frac{r_{\mathrm{x}} - r_{\mathrm{y}}}{2} \begin{pmatrix} e^{2\mathrm{j}\phi} & 0 & 0 & e^{2\mathrm{j}\phi} \\ 0 & e^{-2\mathrm{j}\phi} & e^{-2\mathrm{j}\phi} & 0 \\ 0 & e^{-2\mathrm{j}\phi} & e^{-2\mathrm{j}\phi} & 0 \\ e^{2\mathrm{j}\phi} & 0 & 0 & e^{2\mathrm{j}\phi} \end{pmatrix} + \begin{pmatrix} 0 & 0 & 1 & 0 \\ 0 & 0 & 0 & 1 \\ 1 & 0 & 0 & 0 \\ 0 & 1 & 0 & 0 \end{pmatrix}. \quad (3.54)$$

Comparing this expression to the ideal RHCPSS and LHCPSS (equation 3.39 and 3.38) it is clear that circular polarization selectivity cannot be achieved with only one layer. The choice of word 'selective structure' over the commonly used 'selective surface' becomes apparent, as an infinitely thin surface is not sufficient to achieve a CPSS with linearly polarized elements.

3.2.4 Multiple Layers

The scattering matrix for one layer is now known. However, the scattering matrix for a multilayer structure needs to be constructed. Since the transfer matrix is easier to propagate, the single layer scattering matrix (3.54) must be converted to a transfer matrix. The total transfer matrix can

be computed and then converted back to a scattering matrix. Assuming equidistant layers, the total transfer matrix is,

$$\mathrm{T}(k,\phi) = \mathrm{T}^{\mathrm{CP}}_{\mathrm{Linear}}(k,\phi_0 = 0) \prod_{n=1}^{N} \mathrm{T}_d \cdot \mathrm{T}^{\mathrm{CP}}_{\mathrm{Linear}}(k,\phi_n), \tag{3.55}$$

where,

$$T_d = \begin{pmatrix} e^{-\mathrm{j}kd} & 0 & 0 & 0 \\ 0 & e^{-\mathrm{j}kd} & 0 & 0 \\ 0 & 0 & e^{\mathrm{j}kd} & 0 \\ 0 & 0 & 0 & e^{\mathrm{j}kd} \end{pmatrix}. \tag{3.56}$$

The transfer matrix $\mathrm{T}^{\mathrm{CP}}_{\mathrm{Linear}}(k,\phi)$ is computed from the following expressions using the 2x2 block matrices for the S and T matrices (follows from (3.32) and (3.33), and some algebra),

$$T_{11} = S_{12} - S_{11}S_{21}^{-1}S_{22}, \tag{3.57a}$$
$$T_{12} = S_{11}S_{21}^{-1}, \tag{3.57b}$$
$$T_{21} = -S_{21}^{-1}S_{22}, \tag{3.57c}$$
$$T_{22} = S_{21}^{-1}. \tag{3.57d}$$

With the above equations the transfer matrix related to the single layer scattering matrix (3.54) becomes,

$$\begin{aligned} T^{\mathrm{CP}}_{\mathrm{Linear}} = &\begin{pmatrix} 1 & 0 & 0 & 0 \\ 0 & 1 & 0 & 0 \\ 0 & 0 & 1 & 0 \\ 0 & 0 & 0 & 1 \end{pmatrix} + \frac{1}{2}\frac{r_{\mathrm{x}} + r_{\mathrm{y}} + 2r_{\mathrm{x}}r_{\mathrm{y}}}{1 + r_{\mathrm{x}} + r_{\mathrm{y}} + r_{\mathrm{x}}r_{\mathrm{y}}} \begin{pmatrix} 1 & 0 & 0 & 1 \\ 0 & 1 & 1 & 0 \\ 0 & -1 & -1 & 0 \\ -1 & 0 & 0 & -1 \end{pmatrix} \\ &+ \frac{1}{2}\frac{r_{\mathrm{x}} - r_{\mathrm{y}}}{1 + r_{\mathrm{x}} + r_{\mathrm{y}} + r_{\mathrm{x}}r_{\mathrm{y}}} \begin{pmatrix} 0 & e^{2\mathrm{j}\phi} & e^{2\mathrm{j}\phi} & 0 \\ e^{-2\mathrm{j}\phi} & 0 & 0 & e^{-2\mathrm{j}\phi} \\ -e^{-2\mathrm{j}\phi} & 0 & 0 & -e^{-2\mathrm{j}\phi} \\ 0 & -e^{2\mathrm{j}\phi} & -e^{2\mathrm{j}\phi} & 0 \end{pmatrix}. \end{aligned} \tag{3.58}$$

Henceforth, the case where $r_{\mathrm{y}} = 0$ and $r_{\mathrm{x}} = r$ will be used. This simplifies the transfer matrix somewhat,

$$T^{\mathrm{CP}}_{\mathrm{Linear}} = \begin{pmatrix} 1 & 0 & 0 & 0 \\ 0 & 1 & 0 & 0 \\ 0 & 0 & 1 & 0 \\ 0 & 0 & 0 & 1 \end{pmatrix} + \frac{r/2}{1+r} \begin{pmatrix} 1 & e^{2\mathrm{j}\phi} & e^{2\mathrm{j}\phi} & 1 \\ e^{-2\mathrm{j}\phi} & 1 & 1 & e^{-2\mathrm{j}\phi} \\ -e^{-2\mathrm{j}\phi} & -1 & -1 & -e^{-2\mathrm{j}\phi} \\ -1 & -e^{2\mathrm{j}\phi} & -e^{2\mathrm{j}\phi} & -1 \end{pmatrix}. \tag{3.59}$$

All matrices involved in equation 3.55 are now known and similar to equation 3.57, conversion back to a scattering matrix is done by.

$$S_{11} = T_{12}T_{22}^{-1}, \tag{3.60a}$$
$$S_{12} = T_{11} - T_{12}T_{22}^{-1}T_{21}, \tag{3.60b}$$
$$S_{21} = T_{22}^{-1}, \tag{3.60c}$$
$$S_{22} = -T_{22}^{-1}T_{21}. \tag{3.60d}$$

As the reader might observe this matrix is very tedious to compute but if certain approximations from scattering theory is applied (the Born approximation [28]) it can be shown that the resulting scattering matrix can be written as,

$$S_{\text{Linear}}^{\text{CP}} = e^{-\mathrm{j}kd}\begin{pmatrix} 0 & 0 & 1 & 0 \\ 0 & 0 & 0 & 1 \\ 1 & 0 & 0 & 0 \\ 0 & 1 & 0 & 0 \end{pmatrix} + \sum_{n=1}^{N} \frac{r}{2}\begin{pmatrix} e^{-2\mathrm{j}kz_n}e^{2\mathrm{j}\phi_n} & e^{-2\mathrm{j}kz_n} & e^{-\mathrm{j}kd} & e^{2\mathrm{j}\phi_n}e^{-\mathrm{j}kd} \\ e^{-2\mathrm{j}kz_n} & e^{-2\mathrm{j}kz_n}e^{-2\mathrm{j}\phi_n} & e^{-2\mathrm{j}\phi_n}e^{-\mathrm{j}kd} & e^{-\mathrm{j}kd} \\ e^{-\mathrm{j}kd} & e^{-2\mathrm{j}\phi_n}e^{-\mathrm{j}kd} & e^{-2\mathrm{j}kz_n}e^{2\mathrm{j}\phi_n} & e^{-2\mathrm{j}kz_n} \\ e^{2\mathrm{j}\phi_n}e^{-\mathrm{j}kd} & e^{-\mathrm{j}kd} & e^{-2\mathrm{j}kz_n} & e^{-2\mathrm{j}kz_n}e^{-2\mathrm{j}\phi_n} \end{pmatrix}. \tag{3.61}$$

This is the total scattering matrix for the entire structure and for frequency f_1 the structure should be a LHCPSS. For which number of layers the structure becomes a LHCPSS for f_1 will now be computed. In order to show this certain elements in above matrix should be minimized and others maximized so that the matrix becomes of the form seen in (3.38). If $\phi_n = -k_1 z_n$ the rotation between each layer is in negative direction and thus introduce θ as $\phi_n = -n\theta$, where $0 < \theta < \pi/2$, in order to keep the rotation a positive number. With this rotation $|S_{11/22}^{LL}|$ is maximized since,

$$S_{11}^{LL} = \frac{r}{2}\sum_{n=1}^{N} e^{2\mathrm{j}\phi_n}e^{-2\mathrm{j}\phi_n} = \frac{r}{2}N. \tag{3.62}$$

Moreover $|S_{11/22}^{\text{RR}}|$ should be minimized. This occurs when,

$$\sum_{n=1}^{N} e^{2\mathrm{j}\phi_n}e^{2\mathrm{j}\phi_n} = \sum_{n=1}^{N} e^{-4\mathrm{j}\theta n} = 0. \tag{3.63}$$

The above equation is a geometric series and thus the sum can be written as ,

$$e^{-4\mathrm{j}\theta}\left(\frac{1-e^{-4\mathrm{j}\theta N}}{1-e^{-4\mathrm{j}\theta}}\right)=0, \tag{3.64}$$

This in turn shows the condition:

$$e^{-4\mathrm{j}\theta N}=1. \tag{3.65}$$

Now we wish to find for which number of layers (N), with a given rotation (θ), this holds. Rewriting equation 3.65,

$$4\theta N=2\pi k, \qquad k\in\mathbb{Z}^{+}. \tag{3.66}$$

$$N=\frac{\pi}{2\theta}k. \tag{3.67}$$

Since both N and k are positive integers the smallest value of N is given by,

$$N_{min}=a, \tag{3.68}$$

where

$$\frac{\pi}{2\theta}=\frac{a}{b}, \qquad a \text{ and } b \text{ relative prime},$$

and consequently $k_{\min}=b$. The minimal number of layers can be directly related to the (smallest) denominator of θ/π. Label the denominator θ_d. Then the simple expression,

$$N_{min}=\begin{cases}\theta_d, & \theta_d \text{ odd}\\ \theta_d/2, & \theta_d \text{ even}\end{cases}, \tag{3.69}$$

gives the number of layers for when the RHCP wave is minimized. However, the cross-polarization should also be minimized for both reflection and transmission. These are all minimized when,

$$\sum_{n=1}^{N}e^{\pm 2\mathrm{j}\theta n}=0. \tag{3.70}$$

This gives, through similar argument as previous, a condition much like equation 3.67,

$$N=\frac{\pi}{\theta}k \tag{3.71}$$

Following similar arguments the result in order to minimize cross-polarization the minimal number of layers are,

$$N_{min}=\theta_d. \tag{3.72}$$

Combining this with previous it is clear that (3.72) is also a solution to (3.69) and thus the minimal number of layers is described by (3.72).

The structure is now a LHCPSS at frequency f_1. This is not the only frequency where this kind of behavior occurs. The structure will become a RHCPSS at a frequency f_2 when the rotation between each layer is precisely $\pi - \theta$ since for an electromagnetic wave a rotation of θ clockwise is the same as a counterclockwise rotation of $\pi - \theta$. This is illustrated in figure 3.3.

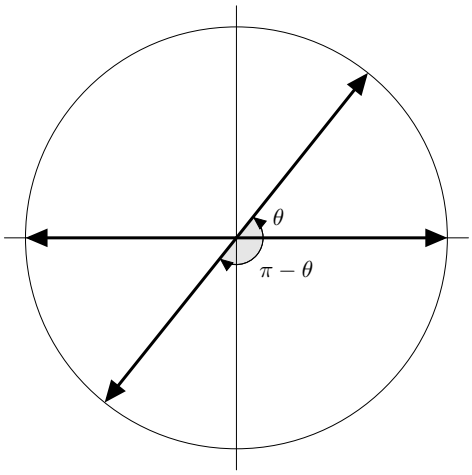

Figure 3.3: Rotation of θ in positive direction and $\pi - \theta$ in negative direction.

The structure will be an RHCPSS since then $k_2 z_n = n\pi - k_1 z_n$ and thus $|S^{\mathrm{RR}}_{11/22}|$ will be maximized and $|S^{\mathrm{LL}}_{11/22}|$ as well as the cross-polarization will be minimized for the previously chosen number of layers N_{min}. This can be seen by the following,

$$S^{\mathrm{RR}}_{11/22} = \frac{r}{2}\sum_{n=1}^{N} e^{-2\mathrm{j}(n\pi - k_1 z_n)} e^{2\mathrm{j}\phi_n} = \frac{r}{2}\sum_{n=1}^{N} e^{2\mathrm{j}(-n\pi + n\theta - n\theta)} = \frac{r}{2}N, \tag{3.73}$$

$$S^{\mathrm{LL}}_{11/22} = \frac{r}{2}\sum_{n=1}^{N} e^{-2\mathrm{j}(n\pi - k_1 z_n)} e^{-2\mathrm{j}\phi_n} = \frac{r}{2}\sum_{n=1}^{N} e^{4\mathrm{j}n\theta}, \tag{3.74}$$

$$S^{\mathrm{LR}}_{11/22} = S^{\mathrm{RL}}_{11/22} = \frac{r}{2}\sum_{n=1}^{N} e^{-2\mathrm{j}(n\pi - k_1 z_n)} = \frac{r}{2}\sum_{n=1}^{N} e^{2\mathrm{j}n\theta}. \tag{3.75}$$

Equation (3.74) is minimized since (3.63) is fulfilled. Similarly (3.75) is satisfied due to (3.70). The frequency when this occurs is given by,

$$k_1 z_n = n\theta, \tag{3.76a}$$

$$k_2 z_n = n(\pi - \theta). \tag{3.76b}$$

Combined and simplified to,

$$k_2 = \frac{\pi - \theta}{\theta} k_1. \tag{3.77}$$

Because $k = 2\pi f$ the same relation holds for frequency.

$$f_2 = \frac{\pi - \theta}{\theta} f_1. \tag{3.78}$$

In satellite communication the separation between the frequencies for the bands is of importance and from above equation this separation can be written as,

$$|f_2 - f_1| = f_\Delta(\theta) = \frac{\pi - 2\theta}{\theta}, \quad 0 < \theta < \pi/2. \tag{3.79}$$

This function is strictly convex and a small rotation corresponds to a large separation.

From this theory a dual band CPSS seems plausible. In Figure 3.4 the discussed S-parameters are plotted as a function of frequency relative to f_1. In this case the rotation between each layer is $2\pi/5$ rad (72°) and the structure consists of 5 layers. The minimization and maximization of the scattering parameters are apparent and the dual band behavior is shown in Figure 3.4.

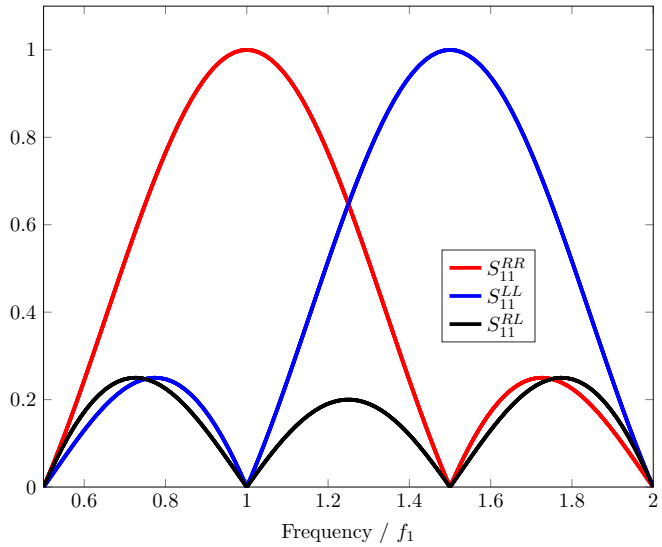

Figure 3.4: Magnitude of S-parameters for a 5 layered structure, each layer rotated $\phi = 2\pi/5$.

In Table 3.1, different rotation angles between layers, the lowest optimal number of layers for that rotation and for which frequencies the dual band CPSS is operating can be seen.

A remark about this theory of weak interaction is that selectivity in reflection is clear but there is no selectivity in transmission. This is a higher order effect and cannot be seen from this simple model. The selectivity can be motivated from a power conservation point of view. If the structure is reflective for a certain incoming polarization ($|S_{11}^{NN}|^2 \approx 1$) then the transmission is bounded by $|S_{21}^{NN}|^2 \leq 1 - |S_{11}^{NN}|^2 - |S_{11}^{NM}|^2 - |S_{21}^{NM}|^2$.

Table 3.1: The number of layers and for what frequencies the dual band CPSS is operating for a certain rotation between layers.

Rotation (degree/radian)	N_{min}	f_2
18° / (π/10)	10	$9f_1$
20° / (π/9)	9	$8f_1$
22.5° / (π/8)	8	$7f_1$
24° / (2π/15)	15	$6.5f_1$
30° / (π/6)	6	$5f_1$
36° / (π/5)	5	$4f_1$
40° / (2π/9)	9	$3.5f_1$
45° / (π/4)	4	$3f_1$
60°/ (π/3)	3	$2f_1$
72° / (2π/5)	5	$1.5f_1$
90° / (π/2)	2	$1f_1$

In this thesis the frequency regions of interest are between 17.7-20.2 GHz and 27.5-30 GHz and $f_2/f_1 \approx 1.36 \rightarrow \theta = 76.3°$. Based on presented theory a 5 layered structure with a rotation of 72° between each layer seems to be a promising candidate. However, in order to investigate proposed structures full wave simulations needs to be done. Typically these are done with periodic boundary conditions (planar infinite structure) in a simulation environment such as CST Studio Suite. If the structures have important regions on the boundary of the unit cell (i.e not confined within the unit cell) only certain angles of rotations can be simulated. This is an important limitation. More on this in later chapter regarding CST models (Section 5.2).

3.3 Proposed Designs

The feasibility of a dualband CPSS has been shown but how to obtain such matrices described has not been touched upon yet. This is the purpose of the following section where theory regarding some designs will be presented. Not all designs have existing theory and the designs that do are based on empirical formulas. The designs lacking in theory will be motivated based on physical concepts. The existing theory will be useful as scripts in different computational programs can be written. These scripts can do a rough optimization and get decent initial parameters of the structure before an optimization in a full wave simulations is started.

It is often quite hard to intuitively have an idea of the solution to Maxwell's

equations (3.2). A very useful concept of microwave network analysis can be used if the circuit dimensions are small in relation to the electromagnetic wavelength. The structure can then be treated as lumped passive or active components. The circuit is small enough so that the phase difference is negligible from one point in the circuit to another and voltages and currents are uniquely defined. Instead of Maxwell's equations (3.2) concepts such as impedance from circuit theory and Kirchhoff's voltage and current laws can be used [29]. The transverse fields can be identified as vector currents and vector voltages [20, 25].

$$\boldsymbol{E}_t = \boldsymbol{V}, \tag{3.80a}$$

$$-\hat{\boldsymbol{z}} \times \boldsymbol{H}_t = \boldsymbol{I}. \tag{3.80b}$$

The ABCD-matrix for voltages and currents can now be written (3.35). These matrices are well known and straight forward to compute for simple circuits. Thus if a layer of the proposed structure has a circuit model equivalent and the parameters of model can be computed then the reflection can be computed and the CPSS simulated in simple scripts.

3.3.1 Linearly Polarized Elements

The theory presented earlier in the chapter was based on linearly polarized elements. For certain such elements there is existing theory of equivalent circuit parameters derived from variational expressions.

Strip

The, perhaps, most simple linearly polarized element is a simple strip. This element will not be used in any presented structure. However, it is very simple and has similarities to other elements and thus it is presented to increase understanding of the subject. The strip is infinitesimally thin in the z-direction, infinite in the x-direction and a certain width in the y-direction. Consider a grid of these strips with periodicity a. For an electric-field impinging perpendicular to the direction of the strip, the effect will be predominately capacitive. For an electric-field impinging parallel to the strip grid the effect will be predominately inductive. The circuit models are then very simple, illustrated in Figure 3.5.

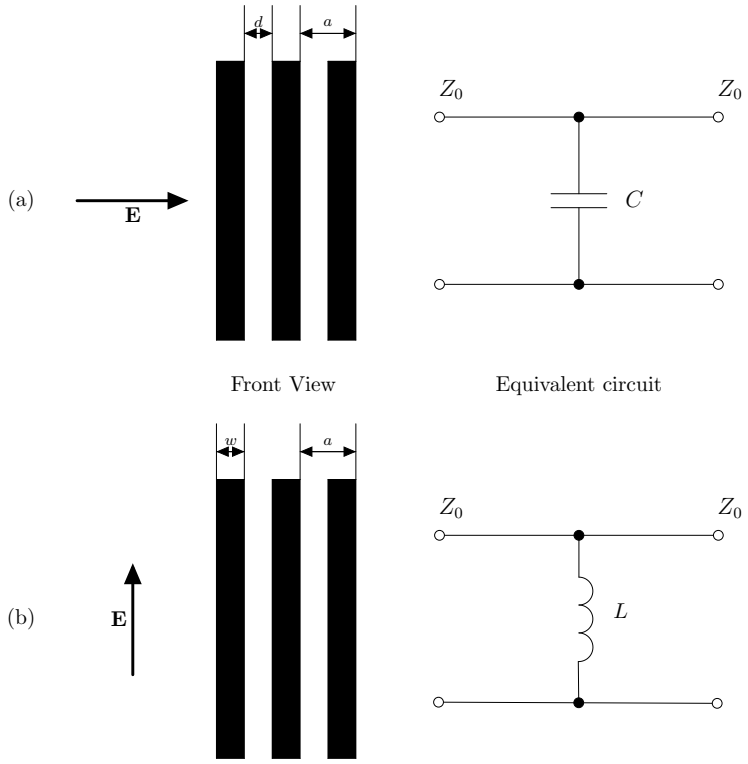

Figure 3.5: Equivalent circuit models for scattering against infinitesimally thin metal strip for normal incidence. (a) Capacitive strips. (b) Inductive strips.

How the capacitance and inductance in Figure 3.5 depend on the geometry have been investigated and can be estimated as follows [30],

$$C \approx \frac{4a\epsilon_0}{2\pi} \ln \frac{2a}{\pi d}, \tag{3.81a}$$

$$L \approx \frac{a\mu_0}{2\pi} \ln \frac{2a}{\pi w}. \tag{3.81b}$$

With these expressions the ABCD-matrix can now be computed (naturally also the scatteringmatrix) and an analytical code can be written to investigate the structure. The ABCD matrix for the circuits in Figure 3.5 is [31],

$$\begin{pmatrix} 1 & 0 \\ -Y_{L,C} & 1 \end{pmatrix}, \tag{3.82}$$

where $Y_L = \frac{Z_0}{\mathrm{j}\omega L}$ and $Y_C = Z_0 \mathrm{j}\omega C$. Using (3.36a) the reflection coefficients are given by,

$$r_{\mathrm{x}} = -1/(1 + 2\mathrm{j}\omega L/Z_0), \tag{3.83a}$$

$$r_{\mathrm{y}} = -Z_0\mathrm{j}\omega C/2/(1 + Z_0\mathrm{j}\omega C/2). \tag{3.83b}$$

From these expressions it is clear that an increase in inductance reduces the reflection in x-direction and an increase in the capacitance increases reflection in y-direction. In order to have a large capacitance the ratio d/a should be small and similarly for a large inductance w/a should be small. The strip grid should therefore consist of closely spaced strips of small width.

Meander Lines

A design that has been gaining popularity when investigating circular polarization selective structures are the meander lines [6, 16]. The meander lines are similar to a strip grid in respect to the circuit model. The geometry of a meander line can be seen in Figure 3.6. From an optimization perspective these grids have more parameters to vary and thus the capacitance and inductance can be tuned in a better way. Moreover in order to obtain good results for oblique incidence there is a requirement that the structure itself has a two fold rotational symmetry but lacking longitudinal-reflection symmetry [9]. The simple strip grid does not have this lack of longitudinal-reflection symmetry and thus neither does a multilayered strip structure. However, the meander lines have a lack of longitudinal symmetry and thus the multilayer structure consisting of meander lines can be constructed to also have this lack of longitudinal symmetry. Only normal incidence is considered in this thesis and the rotational symmetry does not matter in this case. It can be considered as a bonus perk of the meander lines.

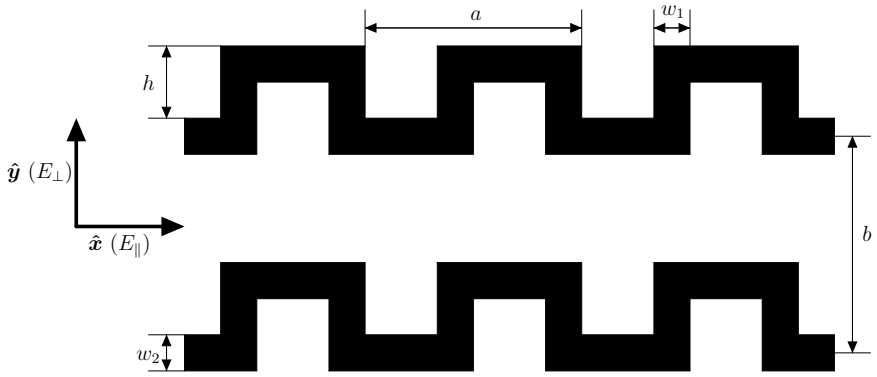

Figure 3.6: Meander line geometry used in analytical model.

The circuit model for the meander line is the same as that of the strip grid. However, the inductance and capacitance is naturally different from that of the strip grid. The admittance for perpendicular polarization $E_\perp$ in the equivalent circuit is given by [32],

$$Y_\perp = \mathrm{j}B_\perp = \mathrm{j}(B_c + B_L + B_\square). \tag{3.84}$$

The first term, B_c, is the contribution due to line segments which are parallel to the meander-line axis and B_L from the segments perpendicular to the meander-line axis [33]. The $B_\square$ term is the contribution of a periodic grid structure of approximate rectangular apertures which forms from the combination of parallel and perpendicular line segments [34]. They can be computed as follows [32],

$$B_c = K_2 \frac{4b}{\lambda} \left[-\ln \sin\left(\frac{\pi(b - w_2)}{2b} \right) \right] \Big/ \eta_0, \tag{3.85}$$

$$B_\square = \frac{1}{\beta - \frac{1}{\beta}} K_1 \left\{ \frac{-\ln\left(\sin\left[\frac{\pi}{4} \left(\frac{a-2w_1}{8a} + \frac{b-h}{2b} \right) \right] \right)}{\frac{1}{2}\left(\frac{b}{h} + \frac{a}{\frac{a}{2}+w_1} + \frac{1}{4}\left[(\frac{b}{\lambda})^2 + (\frac{a}{\lambda})^2 \right] \right.} \right\}, \tag{3.86}$$

$$\beta = \left[1 - 0.205 \left(\frac{a - 2w_1}{8a} + \frac{b - h}{2b} \right) \right] \Big/ \left[\frac{1}{2}(a + b)/\lambda \right]. \tag{3.87}$$

Here, λ is the free space wavelength, a is the meander-line pitch, b is the periodicity of the meander line array, h is the height of the meander line, w_1 is the line width of the meander line perpendicular to axis and w_2 is the

line width of the meander line parallel to axis. The assumed unit is inches. K_n are empirical constants with values:

$$K_1 = 7.1772 \cdot 10^{-3},$$

$$K_2 = 3.2661,$$

$$K_3 = 9.2989 \cdot 10^{-3}.$$

If the impinging electric field is in parallel polarization with respect to the structure then the impedance is given by,

$$Z_{\parallel} = \mathrm{j}X_{\parallel} = \mathrm{j}(X_1 + X_2). \tag{3.88}$$

$$Z_{\parallel} = \frac{\mathrm{j}\eta_0 a}{2\lambda\left[1 - \left(\frac{fh}{5.62}\right)^2\right]} \cdot \left\{K_4\left[-\frac{b}{a}\ln\left(\frac{\pi w_2}{2b}\right)\right] - K_5\left[\frac{2h}{a}\ln\left(\frac{4a}{\pi w_1}\right) - 0.492\right]\right\}. \tag{3.89}$$

f is the frequency in GHz and the empirical constants are [34],

$$K_4 = 5.3242,$$

$$K_5 = 1.7424.$$

This model has been validated by Blackney et al. [33]. There is another model which uses a simpler equivalent circuit [35]. This model assumes equal width of the parallel and perpendicular line segments but an attempt of extending this to more general meander lines have been made [34]. With these models of capacitance and inductance the meander line structure can now be described analytically and simulated quickly after implemented in a coding language of choice.

Capacitively Loaded Strip

Due to the restrictions of unit cell feasibility described in upcoming Section 5.2, other structures which are contained completely within a parallelogram are of interest. The rotations between the layers in the structure can then be set to any angle and moreover the number of parameters to use in optimization will increase. As seen in this theory section a layer for which the impinging electromagnetic wave has a strong response in one direction but not in the orthogonal direction are of interest when constructing a dual band CPSS. One way to construct such a structure is to have large

polarizability of the structure in one direction. A proposed structure and the circuit model is seen in Figure 3.7.

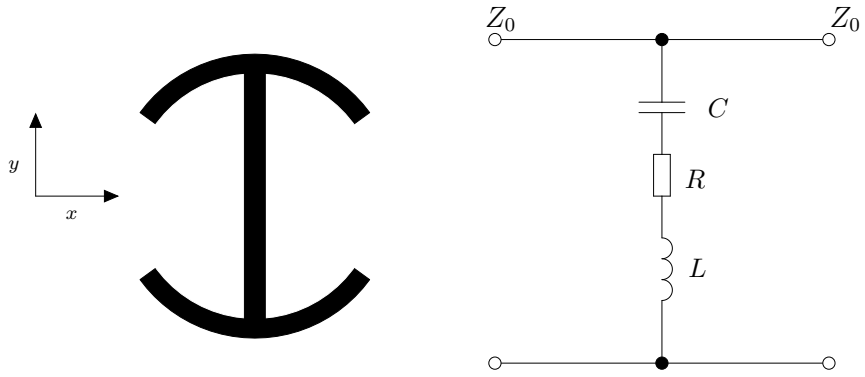

Figure 3.7: Circuit equivalent for capacitively loaded strip structure

An electric field oriented in the y-direction will feel a larger capacitance compared to an electric field oriented in the x-direction. The circuit model is the same for both orthogonal directions but the circuit parameters change and likely the capacitance is affected the most. To the author's knowledge no analytical study of this structure has been done and thus there are no explicit formulas to relate the geometry of the object to the circuit parameters. There will not be an explicit code to do rough optimization and a good initial point for full wave solvers might not be found.

Chapter 4
Analytical Model

Based on previously presented theory, the implementation in any programming language of choice is straight forward. Initially the code was written in Python but it has also been implemented in MATLAB and both codes are in agreement. Optimization routines from both programs were used. In pseudocode the script can be summarized by:

```
Define constants;
Define frequency regions;
if use_materials
    define materials;
else
    set materials to vacuum;
end

parameters=start_parameters;
optimal_parameters=minimize(PenaltyFunction,parameters);
ScatteringMatrix=ComputeSmatrix(optimal_parameters);
PlotCharacteristics(ScatteringMatrix);


function PenaltyFunction(parameters)
    Define Penalty;
    ComputeSmatrix(parameters);
    evaluate Penalty;
return Penalty;

function ComputeSmatrix(parameters)
    Compute reflection %Based on Goldstone [35]
    for Number_of_layers
        Compute Transfermatrix;
        Compute Propagationmatrix;
        Convert to circular polarization;
        Multiply with total Transfermatrix;
    end
    Convert Transfermatrix to Scatteringmatrix;
return Scatteringmatrix;
```

The code is very fast and one run will take approximately two minutes. There is no need for a good computational computer to run this code. After one iteration the script can be run again with the previous obtained best parameter setting to continue optimization and hopefully further improve the results. The end result from this code will then be used as a starting point for optimization using full wave solvers.

Chapter 5

Implementation in Full Wave Solver

There are many full wave solvers on the commercial market. The program that is used in this thesis is the CST Studio Suite from 2015 with an educational license provided by the Department of Electrical and Information Technology, Faculty of Engineering, Lund University. CST uses a Finite Integration Technique (FIT), in the frequency domain the implementation is very similar to the Finite Element Method (FEM). Unlike many other numerical methods which solve Maxwell's equations (3.2) in their differential form CST solves the equations in their integral form. To be able to solve the equations numerically a finite domain needs to be defined. CST creates a mesh of the domain and then formulates Maxwell's equations on each cell separately. In essence this then becomes a large matrix problem. CST has different solvers which compute the S-parameters. The main solver of interest is the Frequency Domain Solver. The frequency domain solver is recommended when periodic structures are considered and hence this is the only solver used in the thesis. Per default the Frequency Domain Solver solves the problem at one frequency at a time and then interpolates the S-parameters in between the computed points. Based on this information CST decides which new frequency points to compute and carries on until a certain accuracy is obtained.

5.1 Conventions in CST

An important thing to note is that CST seems to use the basis,

$$\hat{\mathbf{e}}_+ = \frac{\hat{\mathbf{x}} - \mathrm{j}\hat{\mathbf{y}}}{\sqrt{2}}, \tag{5.1a}$$

$$\hat{\mathbf{e}}_- = \frac{\hat{\mathbf{x}} + \mathrm{j}\hat{\mathbf{y}}}{\sqrt{2}}, \tag{5.1b}$$

instead of the RHCP and LHCP for each port. When converting the CST data for use in other programs one has to be careful and keep this in mind.

A complete transformation to the standard form (3.37) is given by the following transformation [12]:

$$\mathbf{S} = \begin{pmatrix} 1 & 0 & 0 & 0 \\ 0 & 1 & 0 & 0 \\ 0 & 0 & 0 & 1 \\ 0 & 0 & 1 & 0 \end{pmatrix} \begin{pmatrix} S_{11}^{\mathrm{CST}} & -S_{12}^{\mathrm{CST}} & S_{13}^{\mathrm{CST}} & -S_{14}^{\mathrm{CST}} \\ -S_{21}^{\mathrm{CST}} & S_{22}^{\mathrm{CST}} & -S_{23}^{\mathrm{CST}} & S_{24}^{\mathrm{CST}} \\ S_{31}^{\mathrm{CST}} & -S_{32}^{\mathrm{CST}} & S_{33}^{\mathrm{CST}} & -S_{34}^{\mathrm{CST}} \\ -S_{41}^{\mathrm{CST}} & S_{42}^{\mathrm{CST}} & -S_{43}^{\mathrm{CST}} & S_{44}^{\mathrm{CST}} \end{pmatrix} \begin{pmatrix} 0 & 1 & 0 & 0 \\ 1 & 0 & 0 & 0 \\ 0 & 0 & 1 & 0 \\ 0 & 0 & 0 & 1 \end{pmatrix}. \tag{5.2}$$

5.2 Restrictions of Unit Cell

Previously in this thesis it has been stated that a unit cell for meander lines cannot be constructed for arbitrary rotations between each layer. Here follows a proof of this and for which angles that a unit cell construction for a structure with material on the boundary of the unit cell is possible.

Consider a two dimensional object of certain width (y-direction) and infinite length (x-direction). If this object is repeated in the y-direction with a period, P, a grid will be constructed. Now consider n layers of this material each layer rotated with an angle α in regards to the previous layer. When observing the obtained material in the xy-plane a pattern of rotated grids emerge. A limitation to simulations is the computational power and finding a unit cell of this rotated grid is important as then the scattering of infinite structures can be computed with use of periodic boundary conditions. However, it is not for every angle of rotation that it is possible to create a unit cell consisting of a parallelogram. Unless explicitly noted the unit cell will moreover be considered to be a parallelogram. The possible angles and the number of layers for a unit cell will now be motivated.

Consider a unit cell emerging from a n-layered, α-rotated grids . In figure 5.1 such a structure is shown with a unit cell highlighted.

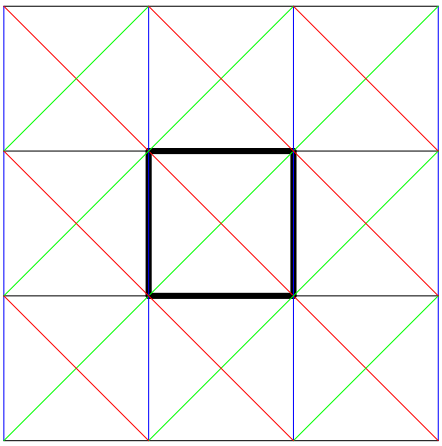

Figure 5.1: Unit cell for a stacked rotated grid. Each layer have a separate color.

This is, according to the author, the most beautiful unit cell but it is not uniquely determined. From the figure some important observations regarding a unit cell can be done. If the unit cell consists of four corners then it can be constructed such that the nodal points of the unit cell contains the intersection of all non-parallel lines (as in Figure 5.1). This is not necessarily the smallest unit cell possible but the smallest unit cell will be a subsection of this larger cell. Moreover, for this type of unit cell, either the grid lines are at the boundary of the unit cell or they have to go diagonally through the center of the unit cell (simple task to prove that the intersection of the diagonals are bisecting each other). The maximum number of non-parallel lines in order for a unit cell to exist is thus 4. Every new layer adds a maximum of one non-parallel line. Thus for a n-layered structure, $n < 4$, a unit cell can be constructed regardless of rotational angle. However, when the number of layers are greater than four the angles for which a maximum of four non-parallel lines exist become restricted. For a five layered structure the following can be formulated:

$$n\alpha = m\alpha + \pi k, \quad m < n \quad n \leq 5 \quad m, n, \in \mathbb{Z}^+, \quad k \in \mathbb{Z}. \tag{5.3}$$

The equations describe the angles, α for which a new layer of grids (n) becomes parallel with a previous layer (m) The above can be rewritten as:

$$\alpha = \pi \frac{k}{n-m}. \tag{5.4}$$

Hence the only angles of rotation that are possible in order to create a unit cell in a 5 layered structure are:

$$\alpha_{unit} = \{0^\circ,\ 45^\circ,\ 60^\circ,\ 90^\circ,\ 120^\circ,\ 135^\circ,\ 180^\circ,\ 240^\circ,\ 270^\circ\}.$$

Additional number of layers will only be a smaller subsection of above. The initial rotation is less than 90° thus the interesting rotations are $\alpha = \{45°,\ 60°\}$ (no relative rotation is uninteresting). Both of these rotations have a maximum number of non-parallel lines less than 5 for any number of layers (as the periodicity is 4 and 3 for 45° and 60° respectively). The above argument does not provide any insight of the feasibility of constructing a unit cell for these angles. This must be investigated. Consider the unit cells provided in the Figures 5.2 and 5.3. All the angles marked in these pictures have an angle of α. Figure 5.2 is the unit cell for $0° \leq \alpha < 60°$ and figure 5.3 when $60° \leq \alpha < 90°$.

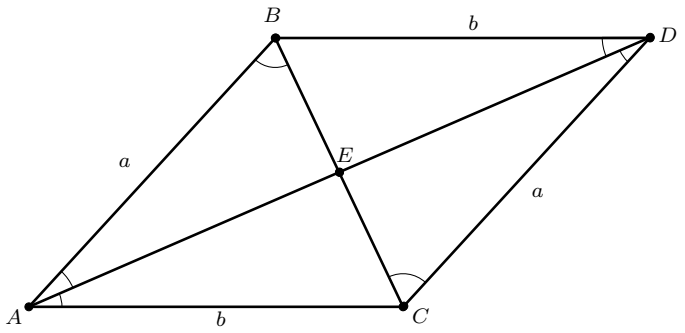

Figure 5.2: Unit cell for arbitrary rotation $0° < \alpha \leq 60°$. All marked angles are α.

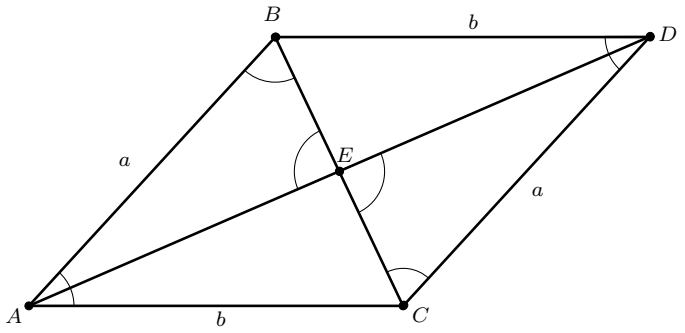

Figure 5.3: Unit cell for arbitrary rotation $90° \geq \alpha > 60°$. All marked angles are α.

For the unit cell in Figure 5.2 it is apparent that in order for the point

E to be in the center the only possibility is $\alpha = 45°$. This can be seen since $\angle ABE = \angle EAB$ it follows from the law of sines that $|AE| = |ED| = |BE| = |EC|$ and $\alpha = 45°$ is the only possible solution. For the other unit cell depicted in figure 5.3 it is clear that $\Delta ABC \sim \Delta CED$. Moreover, $|AC| = |BC| = b$ and if E is the midpoint $|EC| = \frac{b}{2}$. By similarity it is obtained that,

$$\frac{|AC|}{|CD|} = \frac{|AB|}{|EC|},$$

$$\frac{b}{a} = \frac{a}{b/2},$$

$$b^2 = 2a^2.$$

Combining this with the cosine rule,

$$a^2 + b^2 - 2ab\cos(\alpha) = b^2,$$

the below equation is obtained,

$$\cos^2(\alpha) = \frac{1}{8}.$$

This equation has only one solution in the region of interest,

$$\alpha = \cos^{-1}\left(\frac{1}{2\sqrt{2}}\right) \approx 69.3°.$$

Now the cases where E is the midpoint of the parallelogram has been dealt with. There are however two more cases to consider and that is when E coincides with the corners of the unit cell (by symmetry D and C are sufficient). This occurs when $\alpha = \{60°, 90°\}$. The possible angles for creation of a four non-parallel lines parallelogram unit cell is therefore $\alpha = \{45°, 60°, \cos^{-1}\left(1/(2\sqrt{2})\right), 90°\}$. Comparing this with the result regarding the number of non-parallel lines it is clear that the only angles for an n-layered α-rotated structure where $n \geq 4$ are $\alpha = \{45°, 60°\}$.

This gives a valuable insight that if the proposed periodic structure has components on the edge of the unit cell only two angles of rotations are possible for a computer simulation with periodic boundary conditions. This is restricting the parameters for optimization. Constructing other structures where there are no components on the boundary (completely enclosed within the unit cell) will give more freedom as then any angle of rotation is possible. Based on theory presented Subsection 3.2.4 the rotational angle for a structure with meander lines will thus be 60°.

5.3 Periodicity of Meander Lines Within a Unit Cell

One layer of the meander line structure should be as depicted in Figure 3.6, where the up-bends align with up-bends and similar for the down-bends. If they do then it is likely that the analytical code will coincide better with the full wave solvers. Naturally one first considers having a meander line of period one within the unit cell. The full structure will then be as depicted on the left in Figure 5.4. There is no alignment of the up/down-bends. Since $\cos(60°) = 1/2$ each new line in the layer gets shifted by half a period with respect to the previous line. This is not bad per se but, depending on the height of the meander lines, the layers will no longer resemble the classic meander lines and coupling and other effects will become more prominent. This alternative layout might give a valuable solution but little is known about the parameter space and much time and computational power is needed to evaluate this properly. A posteriori, the height of certain meander lines were large in certain cases and the layers no longer resembles meander lines and so one period in the unit cell is not used all that frequently.

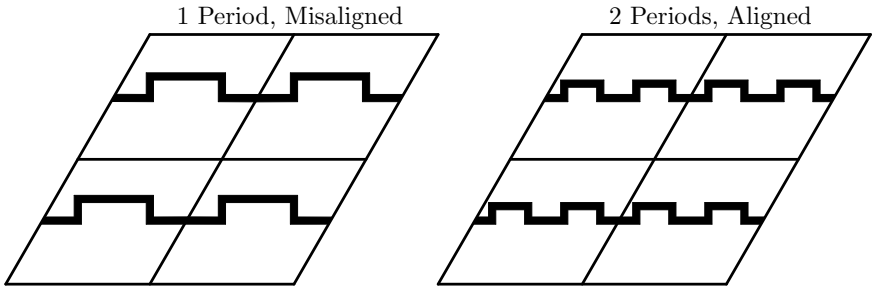

Figure 5.4: Meander line structure for 1 period and 2 periods. Each show a four unit cell structure.

Instead a two period meander line within the unit cell will be used. This is seen on the right of Figure 5.4. This will give stronger meandering of the lines compared to the case of a single period. This change can be implemented in the analytical code. The reason for two periods is simple to understand as the alignment is now correct. A mathematical motivation showing this will now follow.

Consider a period of two distinct features, a and b, which should align after a shift. One period can be described by the 2-tuple $P = (a, b)$. Consider the n-tuple $M = [P]^{n/2}$ where n is an even number. Then after $m = n/2$

cyclic shifts the n-tuples should be equal.

$$\sigma^m M = M. \tag{5.5}$$

If m is odd,

$$\sigma^m M = (b, P, ..., P, a) \neq (P, P, ..., P, P) = M. \tag{5.6}$$

If m is even,

$$\sigma^m M = (P, P, ..., P, P) = M. \tag{5.7}$$

Thus the number of periods within the unit cell must be even in order for alignment to be as depicted in Figure 3.6.

5.4 Optimizing

During the optimization the penalty function is the key in order to obtain results of value. In this case there are eight functions of value, four for each frequency region. In short the penalty function used can be written as:

$$P = \sum_{n=1}^{N} \sum_{m=1}^{4} c_{n,m} \int_{f_n^{low}}^{f_n^{up}} [h_{n,m}(f) - l_{n,m}] \cdot \theta(h_{n,m}(f) - l_{n,m}) \mathrm{d}f, \tag{5.8}$$

where N is the number of frequency regions (in this case two), $c_{n,m}$ is the weight of each function, $h_{n,m}$ is the function of interest (Insertion Loss (IL), Return Loss (RL) or AR), $l_{n,m}$ is the threshold under which the penalty for the particular function is 0 and $\theta(x)$ is the Heaviside step function. For the most simple case where the weight is equal and every function of interest should be zero ($l_{n,m} = 0$). The penalty function becomes the more simple and understandable:

$$\int_{\text{band1}} (\text{RL}_1 + \text{IL}_1 + \text{AR}_{\text{refl},1} + \text{AR}_{\text{trans},1}) \mathrm{d}f + \int_{\text{band2}} (\text{RL}_2 + \text{IL}_2 + \text{AR}_{\text{refl},2} + \text{AR}_{\text{trans},2}) \mathrm{d}f. \tag{5.9}$$

Regardless of algorithm used the penalty function has the same form.

5.5 CST Optimization Routines

A valuable perk of CST is that all important parameters for this thesis can be computed with post processing tools in CST. There is no need to export data in order to compute IR, RL and AR. This also makes it simple to use

the built in optimizers. The CST program has several different optimization routines, and they each have their own advantage and disadvantage. Here follows a brief introduction to the routines used to optimize the proposed structures.

5.5.1 Nelder-Mead Simplex Method

A method that is available in CST uses is the Nelder-Mead Simplex method. This method starts by creating a shape of N+1 points (where N is the dimension of the parameter space). Consider the simple case of N=2. The shape is then a triangle. The routine then moves the corners of the triangle and this triangle moves in the parameter space and hopefully converges on the global minima. The method can converge on non stationary points. The convergence is quite fast if the dimension is small (less than five) [36].

This method is used when a better initial guess has been obtained to avoid getting stuck in an undesirable minimum.

5.5.2 Trust Region Framework

Another routine used in this thesis work is the Trust Region Framework. An initial point is chosen and around this point a linear model is constructed and the user then defines a trust region radius where it is believed that this linear model is good. Then the next point is the predicted minimum from the linear model. If the value here indeed is better and the linear model predicting the value was good then a new trust region radius around this point is made and and the method is repeated. If the value is lower but the linear model was not, then the trust region radius is kept and a new linear model is computed. Lastly if the value did not decrease then the size of the trust region is changed. This algorithm excels at finding the best value when the parameter ranges are small and if the initial guess is relatively close to the minima.

5.5.3 Genetic Algorithm

The third optimization routine used was invented by John Holland in 1975 and is described in his book “Adaptation in natural and artificial systems” [37]. The routine draws inspiration from evolution and uses a survival of the fittest approach to find an optimal value. As in genetic randomness of mutation has an essential role. Roughly speaking, the algorithm starts with an initial population and the fitness of this set is evaluated. The parent population will then produce offspring population and mutate it. The cycle

is then complete and is iterated until completion. This is illustrated in the flowchart of Figure 5.5.

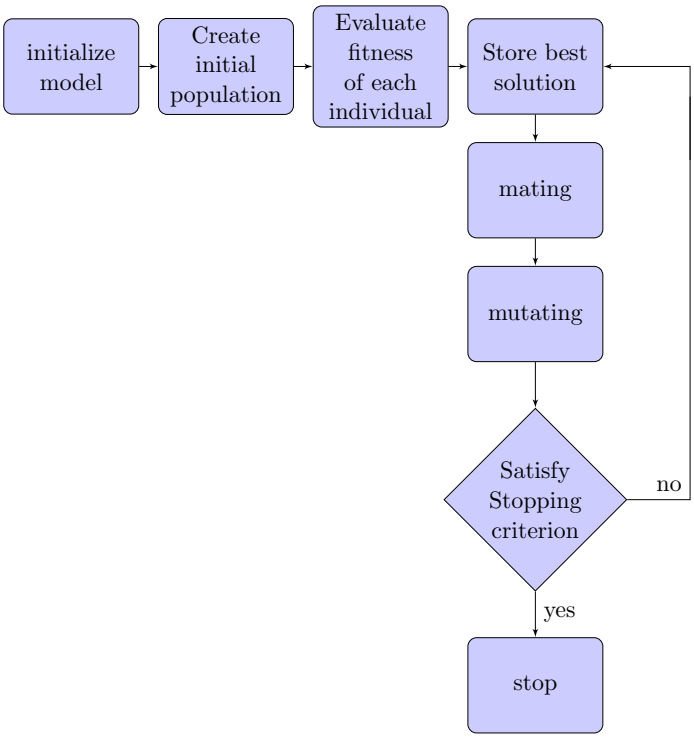

Figure 5.5: Flowchart of the genetic algorithm routine.

Important to keep in mind is that this optimization routine saves and uses information from previous runs. The algorithm is very robust and can be applied to any problem, provided it can be formulated as a function optimizing problem [38]. The genetic algorithm is generally a very good routine when the problem consists of a large and complex parameter space where the initial guesses are bad and the minima might be many and sharp. One drawback is that the algorithm often requires a lot of iterations (i.e time) to run. However, with use of parallelization the computational time can be reduced, note that parallelization was not used in the thesis. Another drawback of the genetic algorithm is that the solution found is not guaranteed to be a global minimum. Due to this the genetic algorithm is often used as a first routine to establish a better starting point for other algorithms when there are no other ways of obtaining a otherwise suitable starting point.

This is generally true but there is no clear cut answer which algorithm to use in this thesis. Certain times when the Trust Region Framework

method was unable to find a better solution, as it was stuck in a minimum, the genetic algorithm could keep improving the solution. The choice of algorithm is dependent on the problem. The convergence of a case when the Trust Region Framework was unable to improve, within the specified parameter space and settings, the genetic algorithm kept improving is seen in Figure 5.6. As seen from this figure an improvement of $\sim 25\%$ was obtained but, as mentioned previously, several function evaluations were required.

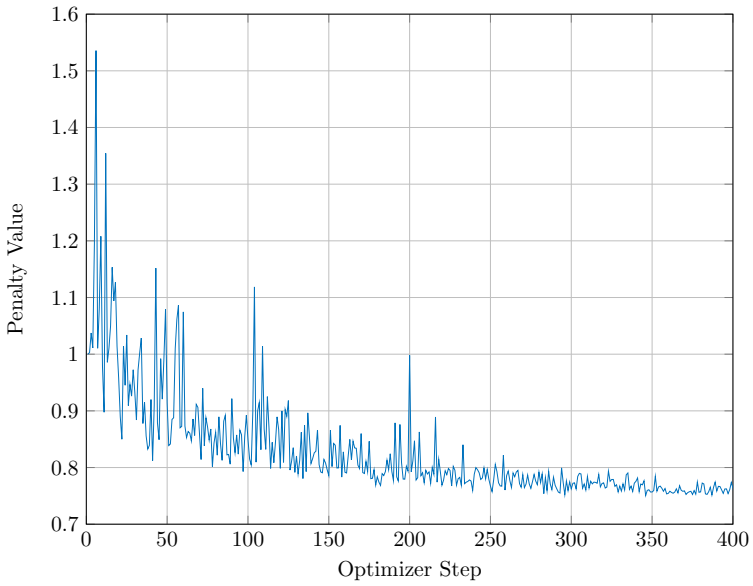

Figure 5.6: Convergence of a typical genetic alogrithm for the problem in the thesis.

5.6 Meshing

When simulating structures in numerical software a discrete mesh of the structure must be introduced. Meshing will introduce numerical inaccuracies. The size of the errors depend on the complexity of the mesh and how fine the mesh is. In a perfect world with infinite computational power this would not be a problem but reality is different and the mesh must be considered when running simulations. There is a trade off between available memory, time and accuracy. CST has a built in feature to adaptively refine the mesh in areas which it consider it needed. Since the structures consist of many interfaces it is also of interest to increase the smoothing so that the mesh size does not rapidly change over interface crossings. For most simulations the adaptive mesh of tetrahedral (Legacy) was used with

a suitable step-size. Assuming that using a finer mesh (more steps per wavelength) gives a more accurate result, the relative average deviation of the S-parameters from the finer mesh can be an indication of mesh quality. The relative average deviation of the S-parameters is computed as,

$$\frac{||S_n| - |S_m||}{|S_m|}, \tag{5.10}$$

for all S-parameters. n indicates the steps per wavelength the simulation used to obtain the S-parameters and m indicates the finest mesh which the S-parameters are compared to. The value is averaged over all S-parameters and frequency points.. A typical result is seen in Figure 5.7. Here the maximum steps per wavelength were 18 and the minimum 3. Basic mesh settings were used for these simulations but it is possible to improve mesh in particular regions of interest when needed but it is not of interest in this comparison. It is seen that the parameters converge rather quickly to the finest mesh.

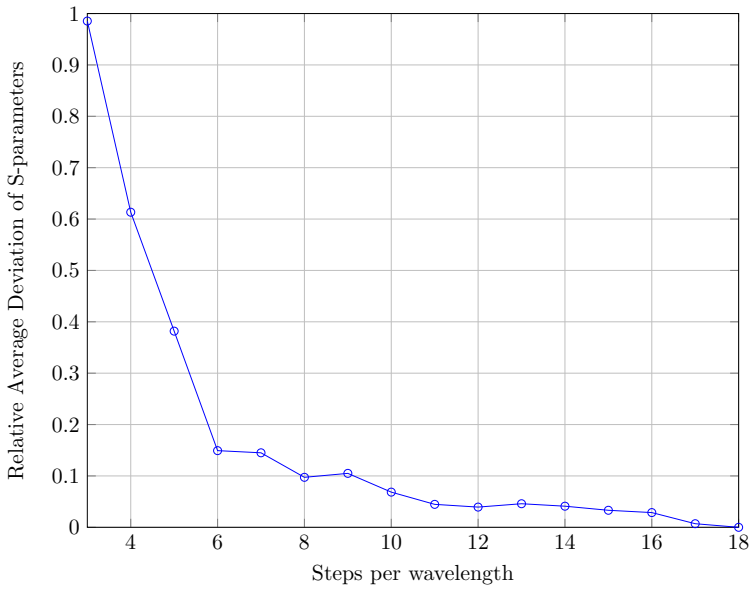

Figure 5.7: Relative average deviation of S-parameters for different mesh-sizes. Based on a 6 layer meander line design.

In order to have reasonable accuracy and speed when optimizing the steps per wavelength is typically 8-10 and the quality of the mesh is raised when finetuning the solution. A single run typically occupied 3-4 GB of RAM and finished within 1.5-2.5 hours. It is possible to maintain decent accuracy in the regions of interest with clever use of computational points and meshing

to reduce the time per run to approximately one forth. This was utilized for certain runs.

5.7 Meander Line

Constructing the meander lines in a full wave solver is straight forward. The important thing to clarify is the labeling of parameters for the optimization and how the structure is sandwiched together. This is the purpose of the current section.

Naturally the meander lines are not suspended in and separated in vacuum but are printed on substrates and glued together on distance materials. This has been taken into account in both the analytical model and for the full wave solvers. The properties of the material can be seen in Section 2.3. The meander line designs and the different parameters used for optimization is seen in Figure 5.8. The subscript indicates which layer is considered. The structure is symmetric in the regard that the parameters for layer -n and n are the same. The scattering matrix will be then be symmetric. As discussed earlier, in Section 5.3, P_{meander} is either equal to P_{cell} or $P_{\text{cell}}/2$ and all layers have the same periodicity. The periodicity parameter which is optimized is P_{cell}. Other parameters optimized on are the height, h, and the width, w.

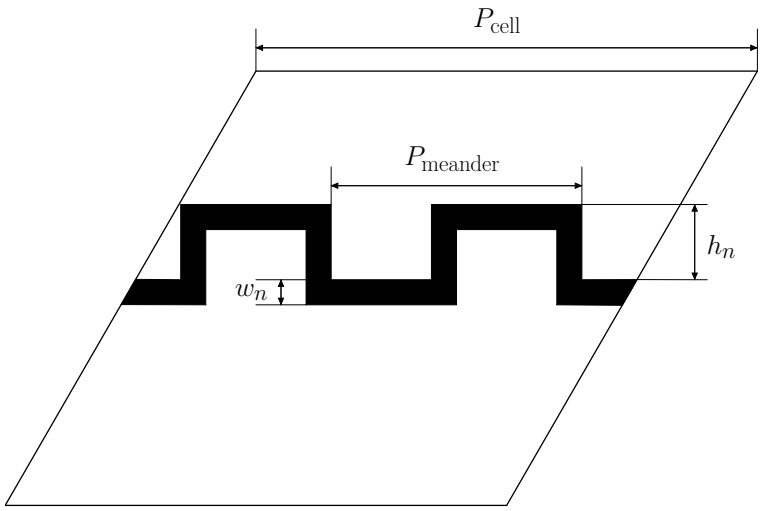

Figure 5.8: Parameters used for optimization of meander structures.

How the structure is put together and how the layers are numbered are seen in Figure 5.9. This is naturally for a general case of layers but the parameters for all layers will now be understood. For an even number of layers the central layer (with substrates etc.) is simply omitted. Note that the bonding layers are in reality surrounding the meander lines and not resting on top of them as the figure might suggest. Thus, the maximal thickness of both bonding layers are the same. The parameters optimized for are the thickness of the distance layers, $d_{\pm n}$, the other thicknesses are preset.

In total this gives a (N+1)/2 height parameters, (N+1)/2 width parameters, (N-1)/2 distance parameters and one periodicity parameter to optimize on if the number of layers (N) is odd, totaling $\frac{3}{2}(N+1)$ parameters. If the number of layers is even, N/2 height parameters, N/2 width parameters, N/2 distance parameters and one periodicity parameter. In total $\frac{3}{2}N+1$ parameters. The problem quickly becomes of high dimension. More parameters can be introduced to increase the freedom (but also complexity) such as different width along different axes. However, this is not done for this thesis but should be kept in mind for future work.

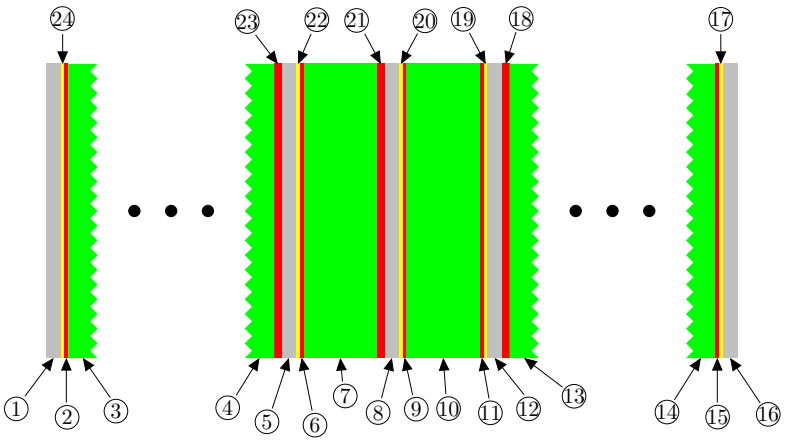

1	Substrate -n	7	Distance -1	13	Distance 2	19	Meander 1
2	Bonding Layer -n up	8	Substrate 0	14	Distance n	20	Meander 0
3	Distance -n	9	Bonding Layer 0 up	15	Bonding Layer n up	21	Bonding Layer 0 down
4	Distance -2	10	Distance 1	16	Substrate n	22	Meander -1
5	Substrate -1	11	Bonding Layer 1 up	17	Meander n	23	Bonding Layer -1 down
6	Bonding Layer -1 up	12	Substrate 1	18	Bonding Layer 1 down	24	Meander -n

Figure 5.9: Composition of layers and their labeling.

5.8 Capacitively Loaded Strip

As with the meander design it is important to clarify the parameters used in the capacitively loaded strip design. The sandwiching of the structure is identical to that seen in Figure 5.9, but the meander lines are now capacitively loaded strips. For an individual layer a unit cell is as depicted in Figure 5.10.

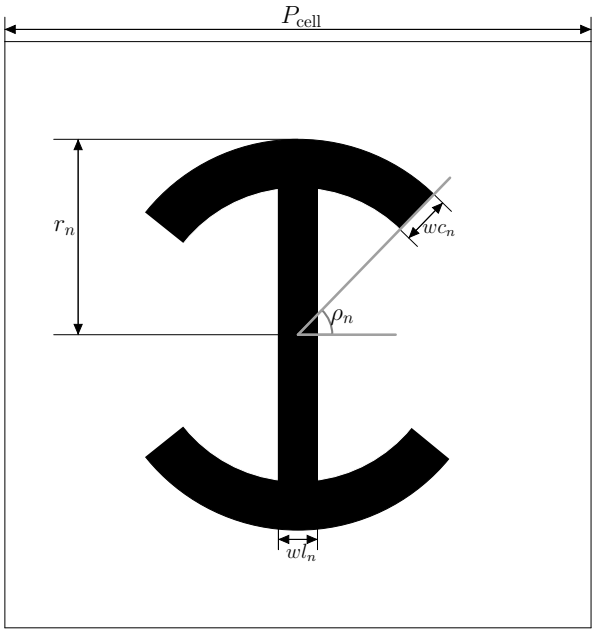

Figure 5.10: Geometry of capacitively loaded strip as implemented in CST.

r_n is the radius of the circle sector, wc_n is the width of the circle sector, wl_n is the width of the center line and ρ_n is the cut angle of the circle sector and as previous P_{cell} is the period of the unit cell. A parameter not seen in this figure is the rotation ϕ_n which is defined as the rotation between layers $\pm m$ and $\pm m \mp 1$. The unit cell can also be tilted when needed, which allows for a tighter packing of the structure.

Chapter 6

Results and Discussion

In this chapter the results will be presented. The parameter values will be given for the best structure of its kind and/or all designs fulfilling the requirements in Table 1.1.

For all the figures presented in this chapter the colors do not represent a certain polarization state but which band is of importance. For the lower band the red curves should satisfy the requirements and similarly for the higher band the color is blue. As previously mentioned all presented designs are LHCPSS in the lower frequency band and RHCPSS in the higher band. The black lines in the graph represent the target requirements and the dashed black lines the relaxed requirements, Table 1.1.

6.1 Meander Line Design

Preliminary studies indicated that the number of layers is a key component when designing a CPSS from multiple anisotropic sheets. Because of this the meander line design will be presented with several different number of layers. This section is thus divided into subsections defined by the number of layers the design utilized. In general an improvement of the results will be seen as the number of layers increases. To this end this subsection will present the results from meander line designs with number of layers ranging from 3 to 9 layers.

For each subsection, the results from the Python code (Section 4) will be presented first followed by the best optimization results in CST. For the designs where a full wave simulation has been carried out, the result will be compared and discussed. The structures which have been optimized the most is the 5 layer and the 9 layer structure. For the 4 layer and 8 layer structures no optimization in CST was done due to limited time and better performance of the designs with other number of layers.

6.1.1 3 Layers

The 3 layer design do not seem to be a suitable structure when studying the result from the Python code in Figure 6.1. For IL and RL the performance of the higher frequency band is better compared to the lower frequency band and for the AR the opposite is true. The design is not close to fulfilling the goals in either band. Nevertheless, this structure was optimized further in CST to establish how well a design of very few layers could perform. The result of the optimization can be seen in Figure 6.2. From this few amount of layers it appears that the IL and RL are far from the target. The minima are mostly within the frequency band of interest, but the magnitude is far off. The AR is noteworthy as the structure surprisingly seems decent in this regard, the design gives very sharp minima in AR for both polarizations and at the same frequencies. The magnitude is low but increases rapidly outside the minima. The performance obtained in CST is much better compared to the analytical code. Some similarities, such as that the higher frequency band has better performance than the lower frequency band for IL and RL, can be seen but in general they differ significantly. Even though the structure does not fulfill the requirements it might prove a useful structure. When developing a method of in-house construction for CPSS this 3 layer structure is relatively simple to construct and has decent performance to be measured. It is possible to use this or similar designs to develop methods for obtaining reliable and consistent CPSS.

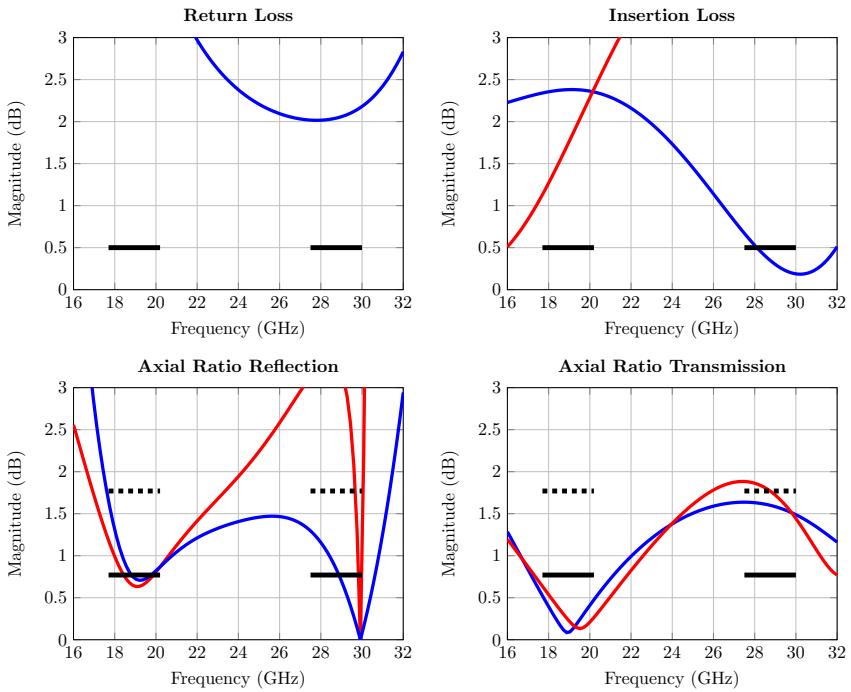

Figure 6.1: Properties of the 3 layer meander line design optimized in Python. Aimed at overall performance.

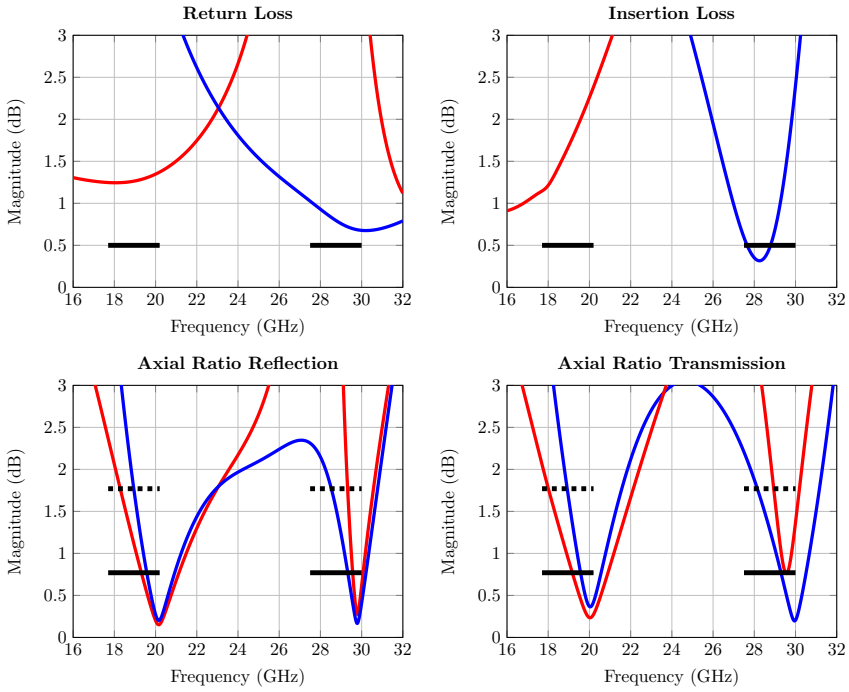

Figure 6.2: Properties of the 3 layer meander line design optimized in CST. Aimed at overall performance.

6.1.2 4 Layers

The 4 layer meander design was only optimized in Python and the result can be seen in Figure 6.3. The design gives very good AR, almost fulfilling the strict requirement. The same can not be said for IL and RL. The IL is manageable but the RL does not fulfill much of the goals in the first frequency band and is ∼1 dB off the target goal in the higher frequency band. However, comparing the result from the 3 layer meander line design, Figure 6.1, with the 4 layer meander line design, Figure 6.3, there is significant improvement in IL and RL. The sharp minima of the AR are no longer present but the overall magnitude is lower for the 4 layer meander line design. Since the performance of few layer has been investigated and the optimization in Python did not give stellar performance, the computational power was better spent on other designs and this design was not developed further.

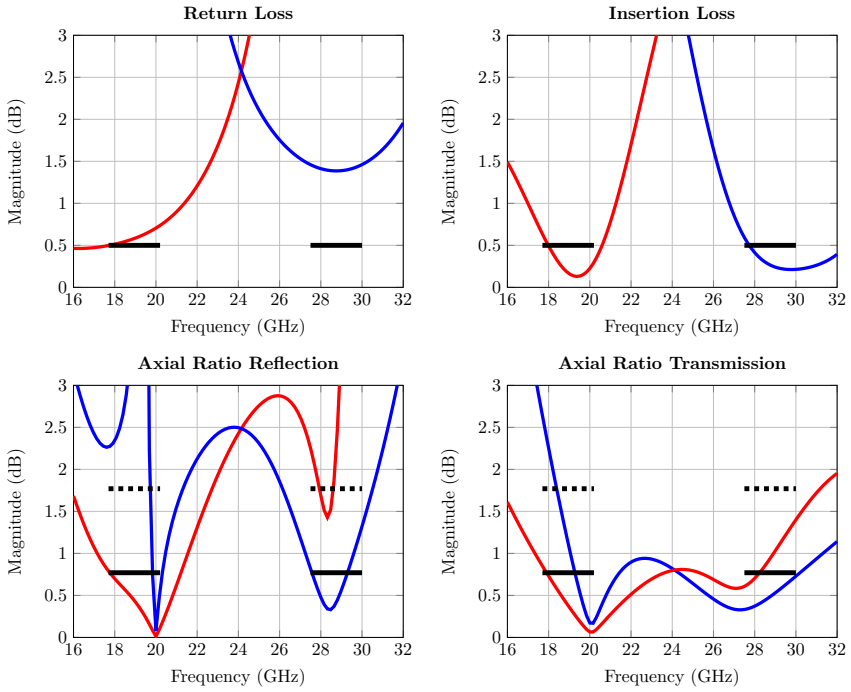

Figure 6.3: Properties of the 4 layer meander line design optimized in CST. Aimed at overall performance.

6.1.3 5 Layers

The result after optimization with the analytical code can be seen in Figure 6.4. The design gives an IL which almost fulfills the requirement. The RL for the lower frequency band is good but for the higher frequency band the requirement is not fulfilled at all, albeit close. The AR is very good fulfilling the strict requirement with ease. In total it is seen that based on this model the structure will not be able to satisfy all requirements set and the most problematic parameter is the RL for the higher frequency band. Comparing Figure 6.3 to Figure 6.4 the trends are similar but differ in magnitude. Figure 6.4 is a superior design with better performance for both bands.

The result after optimizations in CST can be seen in Figure 6.5. The IL for this design fulfills the requirement but the RL does not reach the target for the higher frequency band, ∼0.5 dB off. The minima for the AR are not as distinct as for previous designs. However, for reflection the strict requirement poses no problem. For transmission the strict requirement is more difficult but the relaxed requirement are easily fulfilled. Comparing

the result from the full wave solver with that of the analytical scripts the agreement is interesting. Even though the parameter settings are much different the general trend of the IL and RL are similar. The AR do not seem to agree well. The analytical results are very good but unfortunately the same can not be said for the full wave results. The obtained result from the full wave solver is still better than the previously presented designs of 3 and 4 layers.

If not for the return loss in the higher frequency band this design is a valid option but since the IL and RL are very important this design will not be used for further investigations.

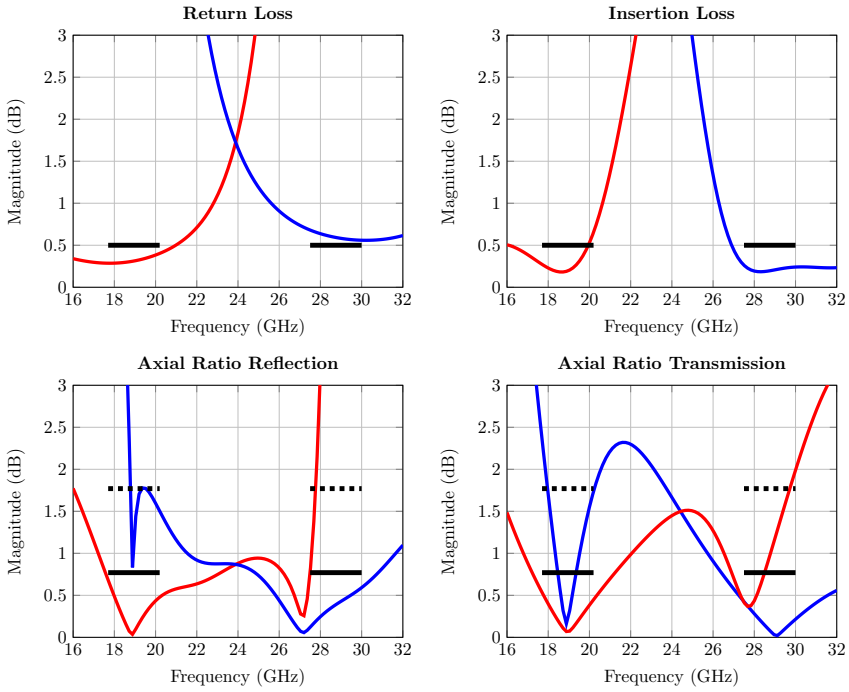

Figure 6.4: Properties of the 5 layer meander line design optimized in Python. Aimed at overall performance.

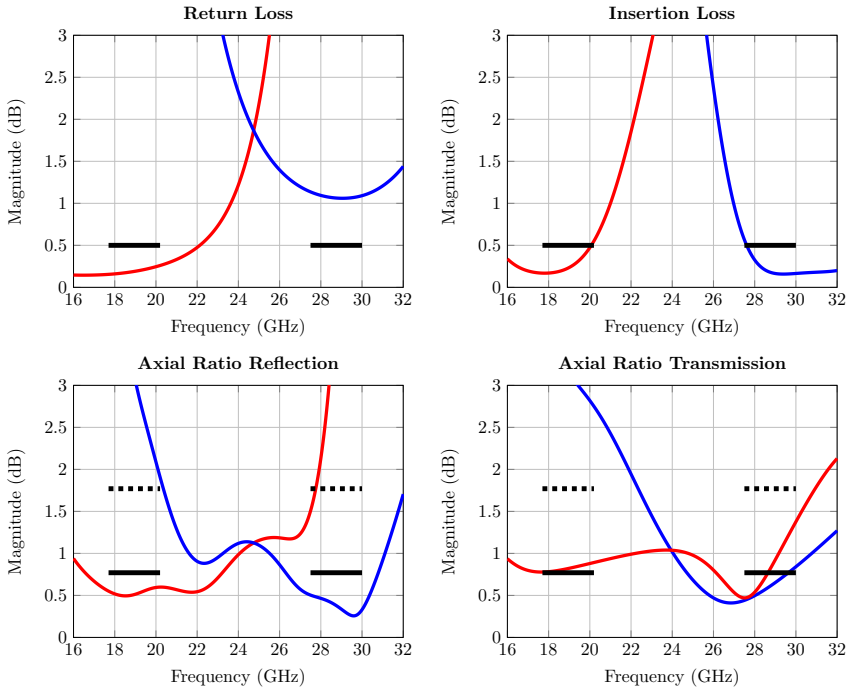

Figure 6.5: Properties of the 5 layer meander line design optimized in CST. Aimed at overall performance.

6.1.4 6 Layers

The 6 layer meander line design seem to perform on par with the 5 layer design based on the result from Python seen in Figure 6.6. It does not fulfill every requirement, but it is not far off as it is only lacking in RL and IL in the higher frequency band. The AR is the best of all previously presented designs.

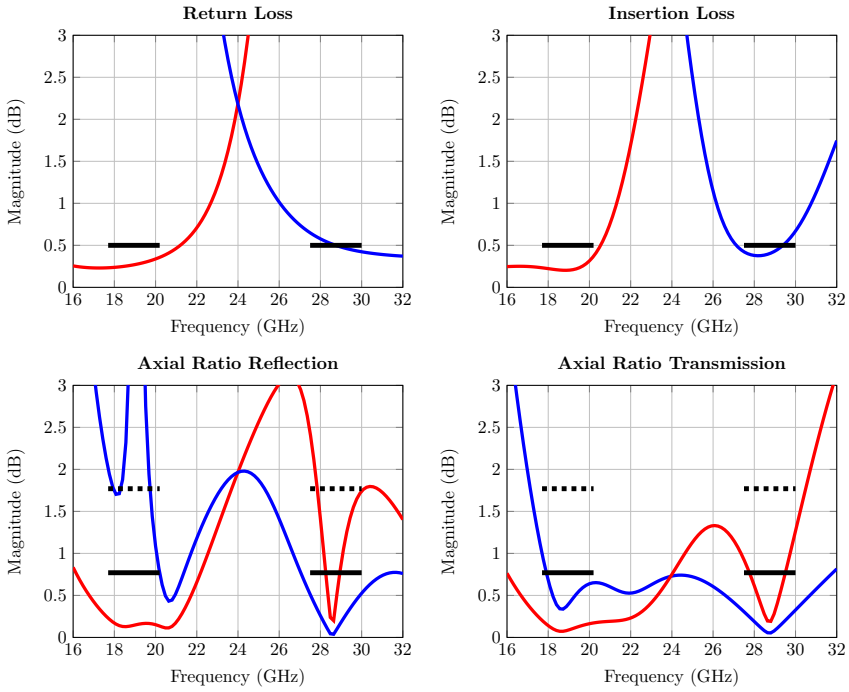

Figure 6.6: Properties of the 6 meander line design optimized in Python. Aimed at overall performance.

When optimizing in CST two different approaches were considered, one where the goal was to pass the strict AR goal and one where the relaxed AR goal was considered. The results of the two optimizations are seen in Figures 6.7 and 6.8 respectively. The AR seen in Figure 6.7 is very good and the strict requirements easily fulfilled. The higher frequency band in both RL and IL proves difficult. Neither is fulfilled and moreover there is an interesting feature around the frequency 29 GHz which disrupts performance. In Figure 6.8, the frequency range starts at 14 in order to see the entire bandwidth. For this design the performance of RL and IL is much better than the set goal, apart from RL in the higher frequency band. The AR does not fulfill the strict requirement but manages the relaxed requirement with ease.

Comparing these results to the Python model (Figure 6.6) it is interesting to see that the AR in Figure 6.7 follows the general trend well. Apart from this there are not many similarities between the analytical results and the full wave results.

Comparing Figures 6.7 and 6.8 it is apparent that there, in this case, exists

a trade-off, increase AR to gain better performance in RL and IL. The strict AR case is not a competitive solution. However, as stated, the relaxed AR case (Figure 6.8) fulfill all requirements optimized for (Compare with Table 1.1). This structure is very valuable and of great interest when considering diplex type setups. The bandwidth for the relaxed case is summarized in Table 6.1. The parameters are given by Table 6.2 and the meander lines as seen in CST are illustrated in Figure 6.9.

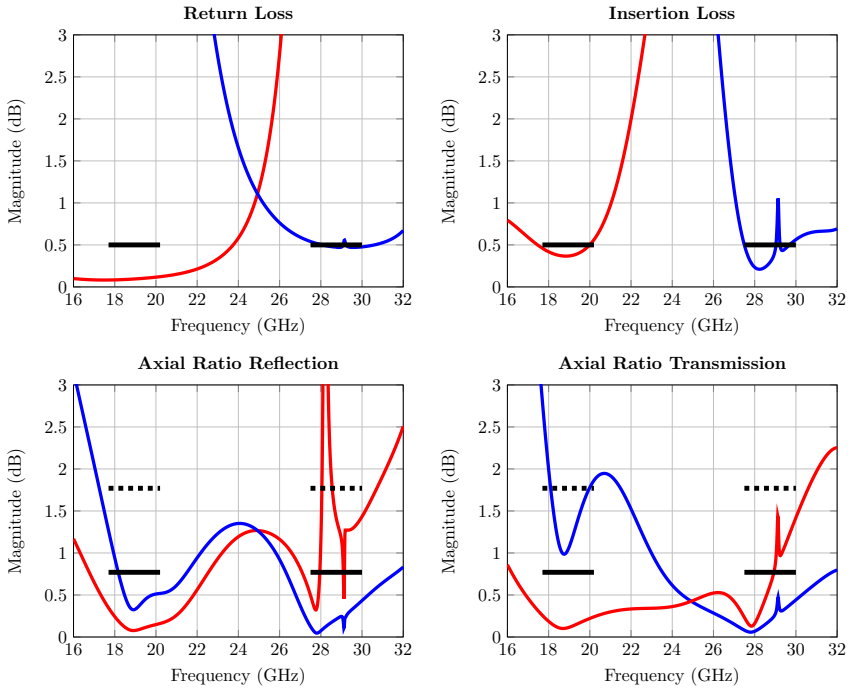

Figure 6.7: Properties of the 6 layer meander line design optimized in CST. Aimed at overall performance.

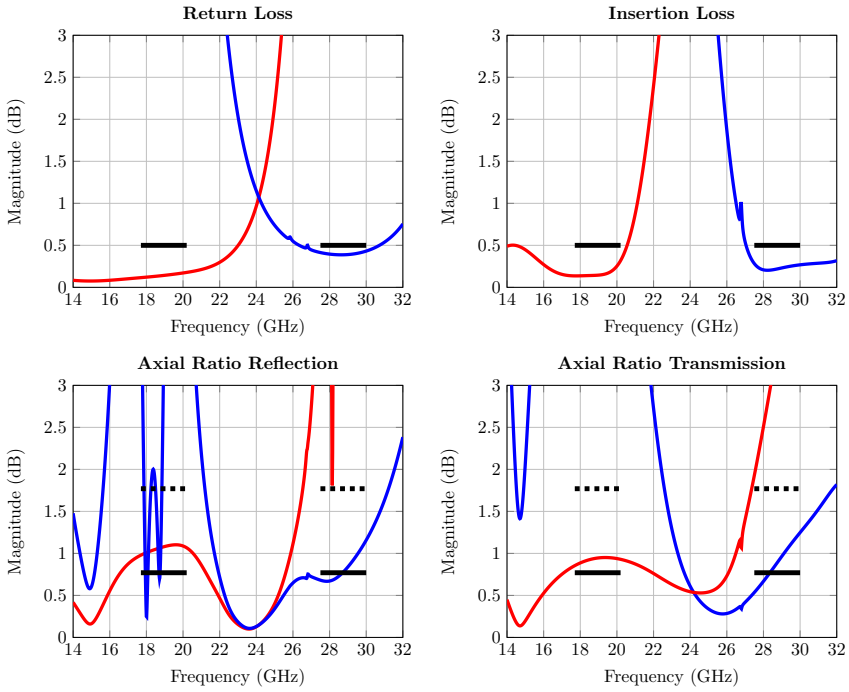

Figure 6.8: Properties of the 6 layer meander line design optimized in CST. Aimed at the relaxed requirements.

Table 6.1: Summarizing the obtained bandwidth for the 6 layer meander CPSS design.

	Frequency range (GHz)	Δf (GHz)	Δf %
Band 1 (relaxed)	14.73-20.55	5.83	33.0
Band 2 (relaxed)	27.04-30.82	3.78	13.1

Table 6.2: Summarizing the parameter values obtained in optimization. All values in mm.

name\number	0	±1	±2	±3
h	-	1.209	1.449	1.315
w	-	0.986	0.630	0.126
d	3.348	2.748	3.066	-
P	5.642	5.642	5.642	5.642

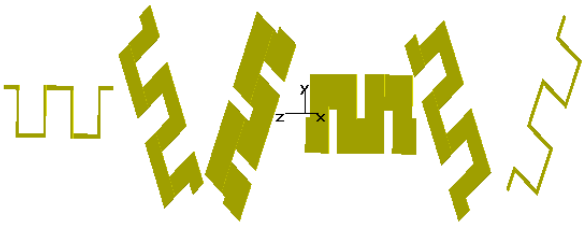

Figure 6.9: A unit cell in CST showing only the meander lines for the optimal solution.

6.1.5 7 Layers

The 7 layered structure struggles in both RL and IL as evident by Figure 6.10 where the result from the Python code is shown. For the presented 4, 5 and 6 layer meander line design the most problematic requirement was the IL and RL in the higher frequency band but for this 7 layer meander line design the IL and RL in the lower frequency band has also become a problem as seen in Figure 6.10. The local AR minima are not within the frequency bands and the magnitude is quite large. Compared to the previous presented 6 layer design (Figure 6.6) the AR is much worse in this 7 layer meander line design. In general it has been seen that an increase in layers seem to give better results but this does not hold true for the 7 layer design. Following the python code a full wave optimization was run which aimed to complete the strict AR requirement. The result is seen in Figure 6.11. The AR is satisfactory and better compared to the Python result (Figure 6.10) but the RL and IL in the first frequency band are not on an acceptable level. Moreover, there is an unwanted feature close to the center of the first frequency band which is seen in all characteristics. This design is outperformed by the previous presented 6 layer design, Figure 6.7.

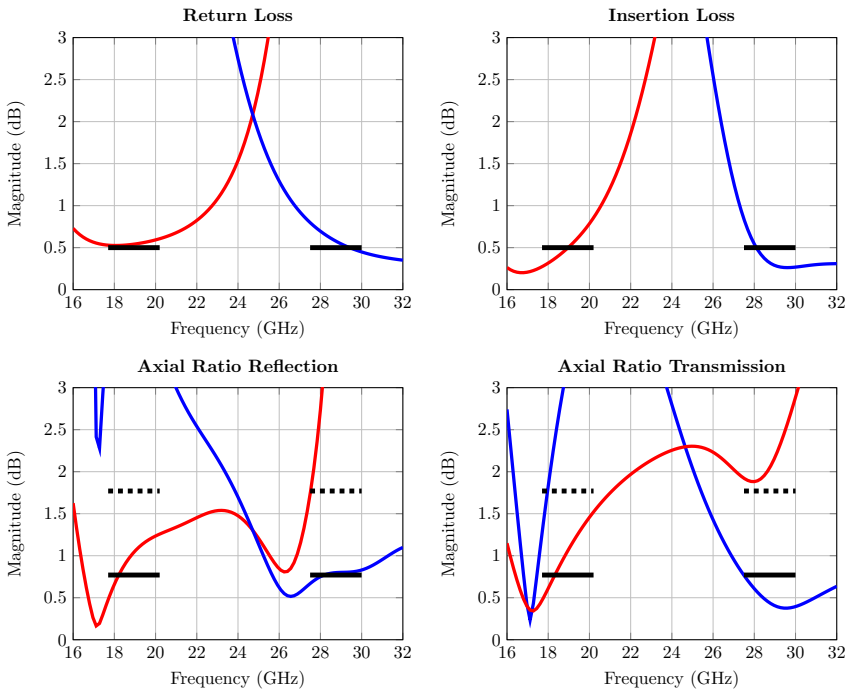

Figure 6.10: Properties of the 7 layer meander line design optimized with Python. Aimed at overall performance.

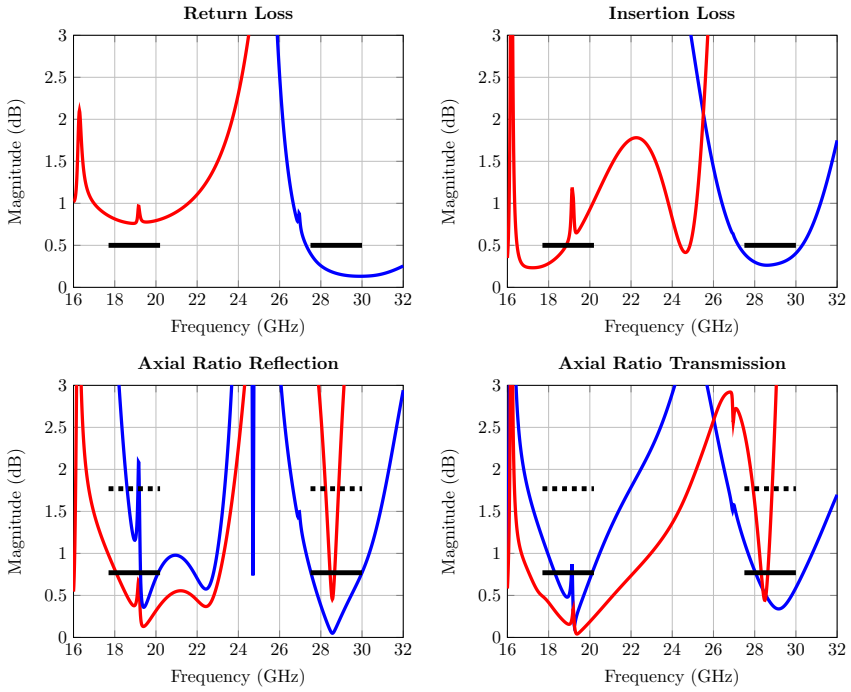

Figure 6.11: Properties of the 7 layer meander line design optimized with CST. Aimed at overall performance.

6.1.6 8 Layers

The 8 layer meander line design was only optimized with the analytical model. The result is seen in Figure 6.12. The strict AR requirement is fulfilled with the exception of transmission for frequencies in the lower frequency band. The big drawback of this design is the poor performance of IL and RL. The performance for frequencies in the lower frequency band is good with respect to RL but very poor in regards to IL. For the higher frequency band the RL is not good enough and the IL barely fulfills the requirement. From this result it seems that the 8 layer will perform on par with previous designs (7 layers) but with very poor IL in the lower frequency band. The 8 layer meander line design also perform much worse than the upcoming 9 layer structure, Figure 6.13. With the lacking performance and the added complexity of more layers as well as the computational time needed this structure was neglected from further modeling.

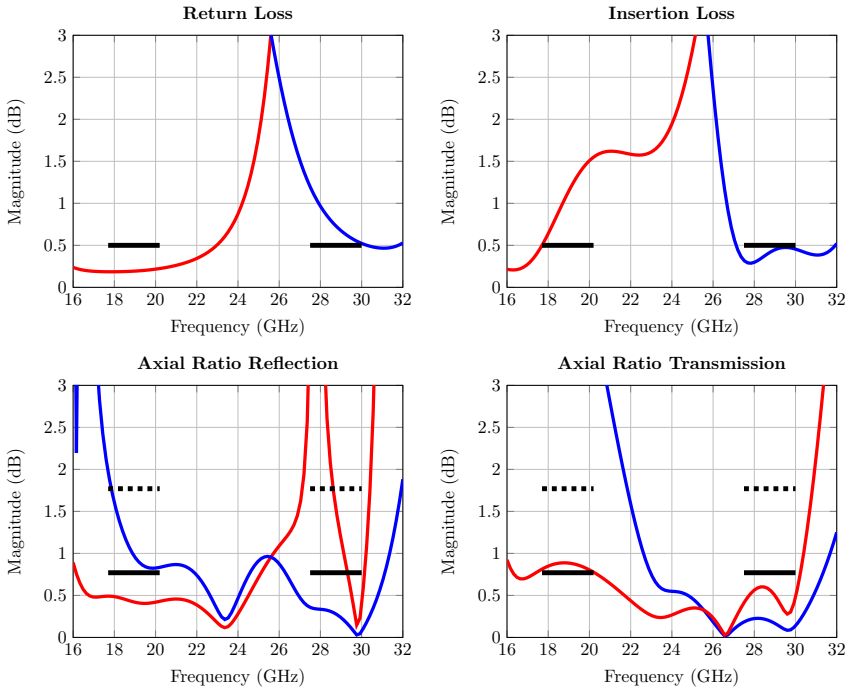

Figure 6.12: Properties of the 8 layer meander line design. Aimed at overall performance.

6.1.7 9 Layers

The result from the analytical model, seen in Figure 6.13, gives the best performance out of all analytical simulations. The RL is very good and the IL almost entirely fulfill the requirement for the two frequency bands. Only for the upper and lower frequencies of the lower frequency band is the goal not met for IL. The AR is also very good and apart from the lower frequencies of the lower frequency band this design fulfills the strict requirement with ease. This is the reason for why 9 layer meander line designs were of great interest when optimizing in full wave solvers.

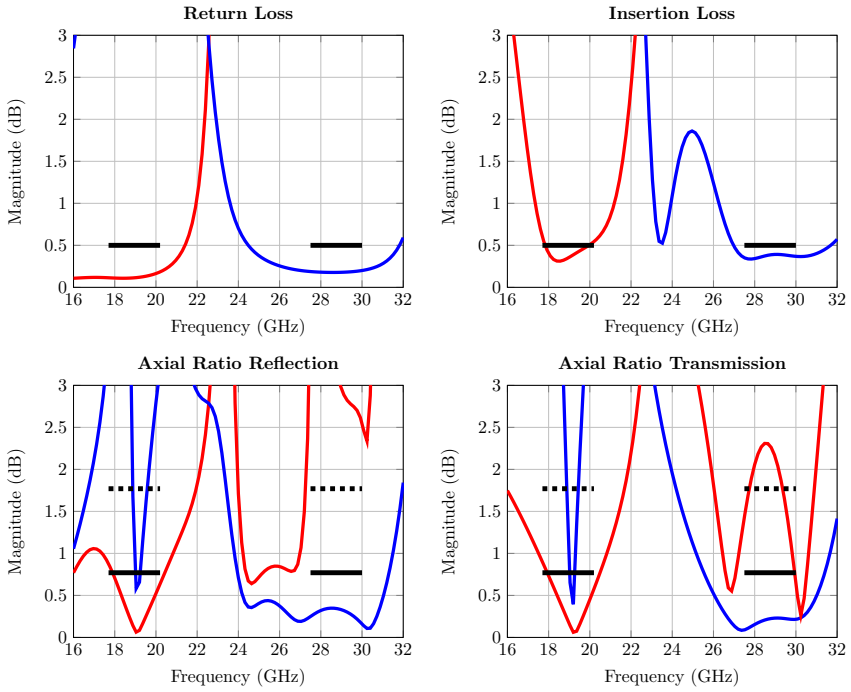

Figure 6.13: Properties of the 9 layer meander line design. Aimed at overall performance.

The result following optimization in the full wave solver is seen in Figure 6.14. Note here that the starting frequency is 14 GHz as opposed to 16 GHz, thus the full bandwidth can be seen. The IL, RL and AR are all very good with local minima of low magnitude in the frequency bands of interest. This design fulfills all relaxed requirements without much trouble and most of the stricter requirements (Compare with Table 1.1). This design has the best performance of all presented designs. The bandwidth obtained in the full wave simulations is summarized in Table 6.3. When comparing with the analytical result it is clear that the return loss and insertion loss has similar trends but the axial ratios do not follow well.

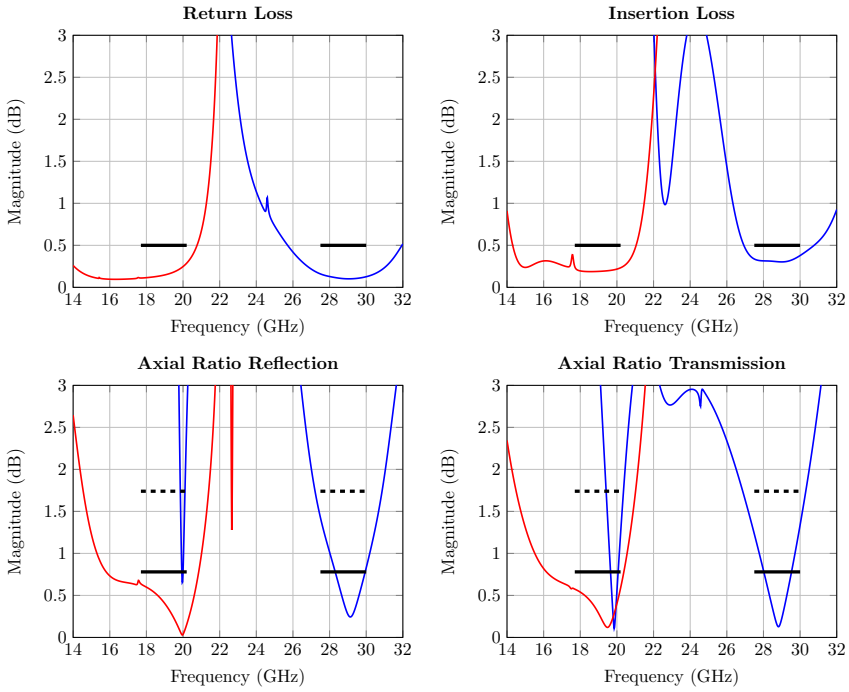

Figure 6.14: Properties of the 9 layer meander line design optimized with CST. Aimed at overall performance.

Table 6.3: Summarizing the obtained bandwidth for the CPSS. Relaxed indicates the higher AR requirement

	Frequency range (GHz)	Δf (GHz)	Δf %
Band 1	16.16-20.38	4.21	23.1
Band 1 (relaxed)	14.55-20.76	6.22	35.2
Band 2	28.31-29.53	1.22	4.2
Band 2 (relaxed)	27.20-30.31	3.11	10.8

The best parameter setup found and a glance of how the meander lines in one unit cell are can be seen in Tabular 6.4 and Figure 6.15 respectively.

Table 6.4: Summarizing the parameter values obtained in CST optimization. All values in mm.

name\number	0	±1	±2	±3	±4
h	3.318	2.383	1.787	0.978	1.295
w	0.126	0.078	0.801	0.156	0.090
d	-	2.839	2.208	3.011	2.729
P	5.032	5.032	5.032	5.032	5.032

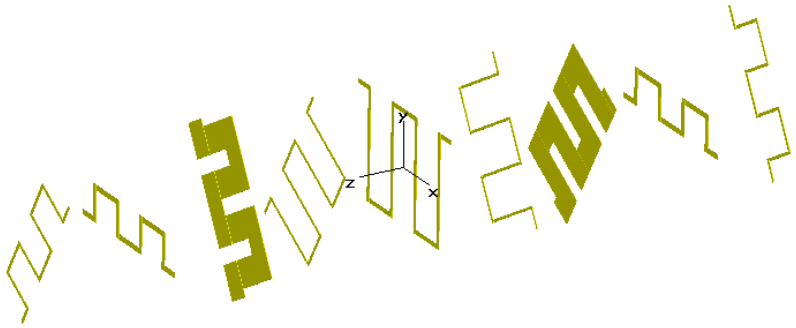

Figure 6.15: A unit cell in CST showing only the meander lines for the optimal 9 layer solution.

At frequency 17.55 GHz there is a small feature most prominent in the IL but it appears in all graphs, see Figure 6.14. To understand this small feature the surface current density on the metal meander lines are illustrated in Figure 6.16. Around the frequency 17.55 GHz there is noticeable current density, compared to the other frequencies, on the layers ±1 as evident from Figure 6.16. This is exactly when the feature becomes prominent in Figure 6.14.

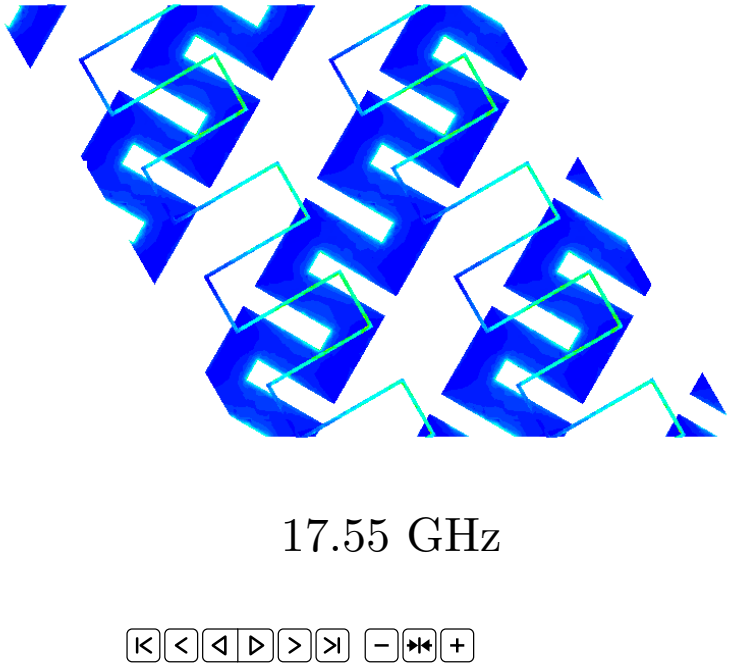

Figure 6.16: Surface current for different frequencies due to RHCP wave incident on structure. Meander 1 and 2 is shown from a 9 layer meander structure.

The meander line ±2 are very wide and there is a relatively high current density at 17.55 GHz on meander line ±1. The effect is very small but it seems to be a coupling between these meander lines. Meander line ±1 serves as a transmitter of a wave due to the current and meander line ±2 couples and seem to serve as a reflecting surface. Much effort was put into removing this feature, but without completely changing performance of the structure it did not seem possible. After an investigation of the parameters of the structure it was found that the parameters which exert the greatest influence over the feature is w_1, d_2 and the Period, P. Other parameters did affect the feature, however it completely changed the response of the structure and are not considered as parameters to control the feature. w_1 controls the position of the feature, increase the value and the feature is shifted upwards in frequency and a decrease will shift it downwards. If the period is changed the position of the feature is also moved. An increase will shift upwards in frequency and increase relative height, a decrease will result in a downwards shift. d_2 has a slight effect on the relative height of the feature. Increase the value and the relative height will get reduced. The price to pay is that for higher frequencies the graphs shift upwards in

magnitude. The described behavior seems consistent with the assumption of coupling. The relative height of the feature is only 0.2 dB and peaks at 0.4 dB. The height is thus never close to the limit and the center of the feature is outside the region of interest and should pose no problems. This feature has been investigated numerically using a a very fine mesh and a tight frequency sampling.

6.1.8 Parametric Study

With the two structures (6 and 9 layers) fulfilling the requirements it is of interest to see the stability of the solution. This can be done in several ways and here follows a parametric study letting each parameter in Table 6.2 and 6.4 vary ±5%. The resulting pictures can be found in Appendix A and Appendix B respectively. This information is very useful if a CPSS is to be constructed so extra care can be taken when manufacturing certain parts of the structure. It should be noted that no parameters were varied at the same time and effects of this are interesting but were not studied.

6 Layer Meander Design

For the 6 layer meander line design the RL and IL are seen to be stable regardless of parameter. Only for d_1, d_2 and w_1 is there a noticeable difference in the higher frequency band. However, the requirements are still met for the entire band. The AR experience more change than the RL and IL but since only the relaxed requirements are considered for this design the variations are insignificant. The parameters which control AR the most seem to be the distance and height parameters, particularly d_1 and h_2. From this parametric study it can be concluded that the structure is relatively stable.

9 Layer Meander Design

The IL and RL are seen to be stable throughout and the AR is also stable but experience more fluctuations which only seem to have an impact on the strict AR requirement and not the relaxed. From this set it is clear which individual parameters has the greatest impact on the structure as a whole. In the 9 layer case, this seems to be the height of the 6 inmost layers followed by the distances between these inmost layers. From this parametric study it can be concluded that the structure is relatively stable.

6.1.9 Usability of Theoretical Model

Glancing at all the presented meander designs one can see that the performance predicted by the Python code does not give good agreement with the simulations for the AR. This is not strange since the parameter settings differ significantly and the AR is seen to be very sensitive. However, it is interesting that the IL and RL are in such good agreement for most cases. This shows us that the Python code can not be used to get the optimal solution but it gives a hint of the general trends of the IL/RL and an estimate of how well the structure might perform after further optimization in a full wave simulation software.

It is interesting to note that the two best solutions found are the 6 and 9 layers designs as the simple theory might predict (Table 3.1). However, the assumptions are not entirely valid as the preferred designs often tended to be relatively extreme in their dimensions. The simple theory implies that the 3, 6 and 9 layered design should be preferred, within certain structural bounds, but the success of the 6 and 9 layer design does not necessarily imply that the model is valid. Based on the result in this thesis, it appears the simple theory is useful to get an idea of what amount of layers should be considered, and what performance should be expected from a given structure.

6.1.10 Meander Designs Overall

From the results presented in this section it, seems that more number of layers are generally better but certain amount of layers, 6 and 9, seem especially good. When increasing the amount of layers control over axial ratio increases at the cost of increased IL. A detail to note is that the optimized designs all had a wide meander line approximately one quarter of the total structure length into the structure and close to this meander line was another meander line which had a relatively large height.

6.2 Capacitively Loaded Strip Design

Another structure that was considered in this thesis is based on capacitively loaded strips. Here the best result following CST optimization of the capacitively loaded strip design will be presented and discussed. These structures had no underlying mathematical model and many degrees of freedom thus the optimization is nontrivial and these structures cannot be considered the best the design has to offer due to the restricted use of computational power and time. It will, however, give an indication as

to what one can expect from this design. Many different simulations were carried out with tweaking of the constants in the penalty function, see (5.8).

The optimization routine initially used was in most cases a genetic algorithm of 497 iterations. After finishing the current optimization the algorithm was changed to Nelder Mead Simplex Method to continue to search the surrounding parameter space, and finally the Trust Region algorithm was used. The structure proved to be very mesh dependent, hard to optimize and not all number of layers gave presentable result.

In Figure 6.17 the result of an 8 layer structure is seen. The AR is very poor with this design as not even the relaxed requirements are fulfilled for the lower frequency band. For the higher frequency band the AR is better but not sufficiently good. Both RL and IL have a lacklusting performance, particularly for the lower frequencies where the IL have several local minima and maxima. The performance is improved with an increase in number of layers and the performance of a 10 layered structure can be seen in Figure 6.18. For this design the RL and IL are both improved compared to the 8 layer design (Figure 6.17). The fluctuations in IL for the lower frequencies can still be seen albeit smaller. The AR for the design fulfills the relaxed requirement without problems but is far from the strict AR requirement. This is a significant improvement over the 8 layer design (Figure 6.17).

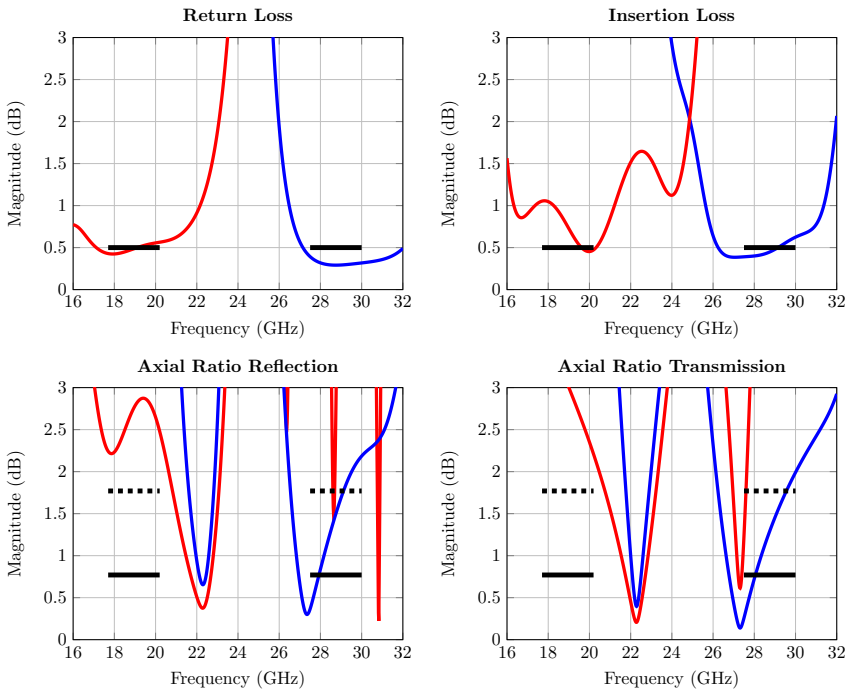

Figure 6.17: Performance of the 8 layer capacitively loaded strip design.

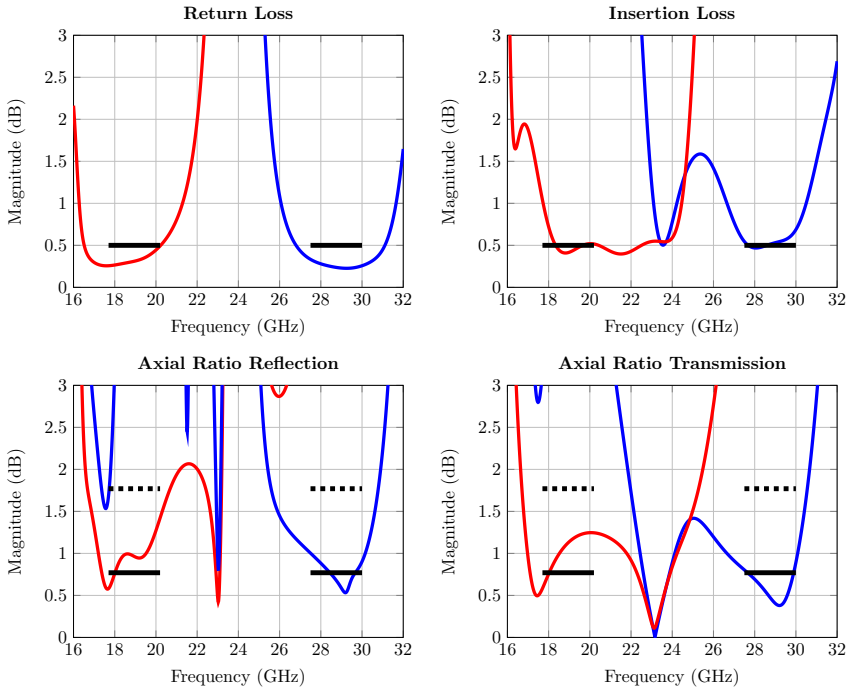

Figure 6.18: Performance of the 10 layer capacitively loaded strip design.

For practical reasons larger numbers of layers were not investigated. Summarizing the results for the capacitively loaded strip design it was seen that these do not quite hit the mark. However, the results given are interesting and indicate that the structure has potential for further optimization. The parameter setting for the 10 layer capacitively loaded strip can be seen in Table 6.5. When running these simulations it was found that the radius of the capacitively loaded strip had great influence over which band the structure performed the best. A very brief attempt to combine two different radii was made. This was made for a 5 Layer structure and the design implemented in CST is illustrated in Figure 6.19. Note the central layer has four small elements with smaller radii.

Table 6.5: Summarizing the parameter values obtained in optimization for the capacitively loaded strip 10 Layered structure. Values in mm, except ρ and ϕ which are in degrees.

name\number	0	±1	±2	±3	±4	±5
wl	-	0.114	0.129	0.125	0.116	0.111
wc	-	0.619	0.573	0.628	0.542	0.442
r	-	2.556	2.556	2.556	2.556	2.556
d	2.333	2.374	2.404	2.817	2.196	-
ρ	-	40.361	44.832	58.861	66.254	61.232
ϕ	-	51.469	57.771	74.451	63.352	73.882
P	-	7.809	7.809	7.809	7.809	7.809

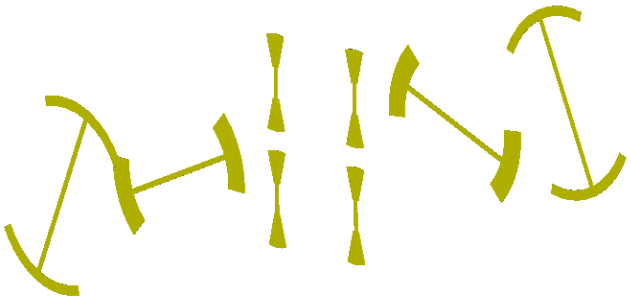

Figure 6.19: A unit cell in CST showing the mix of radii for the capacitively loaded strip design.

The result of this design can be seen in Figure 6.20 and the parameters settings in Table 6.6. The RL is good for the lower frequency band but for the higher frequency band the RL is not low enough. The fluctuations in IL seen in the previous designs (Figure 6.17 and 6.18) is present for this design as well. In the lower frequency band the IL is slightly off target and in the higher frequency band the performance is poor with a local maxima in the center of the band ∼0.5 dB over the target goal. The AR for the lower frequency band is decent though the magnitude sharply rises outside the target band. For the higher frequency band the AR is worse, the relaxed requirements is not fulfilled for the entire band and the strict requirement is far from fulfilled. Even though the structure has obvious flaws in performance the result is better than a 5 layer capacitively loaded

strip design and slightly worse than the 10 layer structure presented in Figure 6.18. Another design was also tested where the center layer was replaced with a strip grid. This did not outperform the mix of big and small radii. The result is valuable for future work when combinations of different structures and sizes might be of importance and indicates that this kind of design freedom can be investigated further.

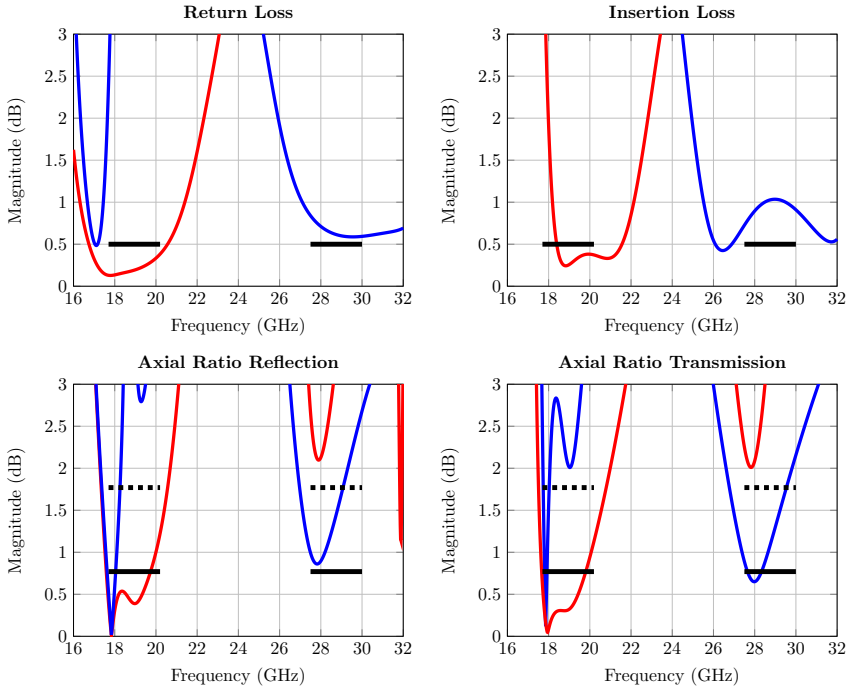

Figure 6.20: Performance of the 5 layer capacitively loaded strip design with center layer of smaller radius.

Table 6.6: Summarizing the parameter values obtained in optimization for the mixed radii consisting of 5 layers. Values in mm, except ρ and ϕ which are in degrees.

name\number	0	±1	±2
wl	0.114	0.129	0.125
wc	0.756	0.541	0.237
r	1.113	2.226	2.226
d	-	3.950	3.182
ρ	74.572	65.525	51.224
ϕ	-	111.378	43.780
P	5.311	5.311	5.311

Chapter 7

Summary and Conclusions

In this work dual band CPSS for space applications, with requirements based on previous projects in related areas, have been investigated. The theory regarding the operation of CPSS has been presented and shown to be simple if certain assumptions were made. With these assumptions and empirical formulas an analytical model for a meander line design was set up in Python. After identifying problems with creating arbitrary unit cells the previous results were used as an initial point for full wave solvers for meander line design. Other designs were also optimized without a good initial point. Two different meander designs, 9 layers and 6 layers, were found to fulfill the requirement in the relaxed AR case and the 9 layer design fulfilled most of the strict requirement.

Going into this project it was not known if a dual band CPSS was feasible with respect to the requirements. A myriad of simulations were carried out for several different design and number of layers. Once a solution was found much computational power was spent improving the design further. It is interesting that even with such a large amount of initial designs and limited power/time that two very capable solutions were found.

In conclusion, the goal of the thesis has been met and feasible dual band CPSS have been simulated with good performance. The two solutions found are both of the meander type design and are unique in the sense that they are the first dual band reciprocal symmetrical CPSS to have a performance on a level where they can be applied. The 9 layer meander line design have a working bandwidth of 14.55-20.76 GHz (35.2%) and 27.20-30.31 GHz (10.8 %) in the relaxed AR and a bandwidth of 16.16-20.38 GHz (23.1%) and 28.31-29.53 GHz (4.2%) in the strict AR case. The 6 layer meander design fulfills the requirement for the relaxed AR for 14.73-20.55 GHz (33.0%) and 27.04-30.82 GHz (13.1%) Based on the parametric study the solutions found are both stable with respect to small design variations.

Even though drawbacks are important to note, the theory presented and the analytical optimization proved a useful tool to have a foundation to stand upon before starting full wave simulations. Throughout this work it has become apparent that implementation in full wave solvers is nontrivial and that there are many things to consider when creating a unit cell for a multilayered structure. These results are very interesting on their own. Moreover, the choice of algorithm used for optimizing the structure is not clear cut. For the problems in this thesis, it seems that the best to use was the genetic algorithm. But due to the nature of those kind of algorithms one has to be clever when setting up the problem if a solution is to be found within a reasonable time. Knowing when to use which algorithm and how to manipulate the penalty function to obtain desirable results is nothing short of an artform.

Chapter 8

Future Work

Structures have been found which completely fulfill the relaxed requirements and most of the strict requirements yet much work remains to be done. Moving on with the 9 layer and 5 layer meander structure they would need to be constructed and measured to further validate the results. Much thought must be spent on how to best manufacture these structures, especially if they will be constructed within the university as tools and facilities are limited. Not only manufacturing but the measurement setup is also of great importance and need to be further expanded upon. It will be important to have low noise and high XPD in the setup to be able to measure the characteristics correctly.

All the optimizations were carried out considering normal incidence. For the intended application oblique incidence also needs to be considered. For a diplexer type setup the angle of incidence is higher than that of doubly curved reflector surface setup. Further work must thus investigate the performance at other angles of incidence and possibly optimize for $\sim 30^\circ$ angle of incidence in the case of the 9 and 6 layer meander line design, as a diplexer setup is preferred in this case.

Due to the limited time and computational power during this project once one solution was found much time was spent to optimize this structure in the best way. Further work should also investigate if similar performance to the 9 layer meander line design is possible with less number of layers as the manufacturing might be problematic for this large number of layers. Naturally as few number of layers as possible is preferred.

There is a possibility to keep studying meander line CPSS designs and carry out changes to the periodicity keeping in mind what was described in Chapter 5. Moreover, the complexity of the designs can increase, for instance by having different parameters for x- and y-directions. This seems

more favorable for designs with lesser amount of layers as the designs of high amount of layers already seem sufficiently complex.

Increasing complexity to find better solutions is a double edged sword. Depending on how the complexity is introduced it is likely that the computational demands will increase. For future work, when it comes to simulation, it is important to understand that the problems are complex and will take much computational power to solve. Investing in more computational power is therefore a highly relevant thing to keep in mind.

The meander line CPSS is now a somewhat understood structure but the other design are still relatively unknown. The other design presented showed potential and further exploration of these structures would be interesting. Other designs were also made and tested but not to an extent that they were added to this work. The different designs all have different perks that make them useful in some areas. Further working with them, and possibly new structures, will lead to a deeper understanding of them. It would be interesting to investigate combining different structures.

Lastly, the theory presented had certain limiting assumptions and for further work it would be of interest to expand this theory and possibly obtain better agreement. A more complete theory is always wanted since it might lead to other designs or possibility of using arbitrary rotational angles.

Bibliography

[1] W. A. Imbriale, S. S. Gao, and L. Boccia, *Space Antenna Handbook*. John Wiley & Sons, 2012.

[2] C. A. Leal-Sevillano, J. A. Ruiz-Cruz, J. R. Montejo-Garai, and J. M. Rebollar, "Novel dual-band single circular polarization antenna feeding network for satellite communications," in *The 8th European Conference on Antennas and Propagation (EuCAP 2014)*, April 2014, pp. 3265–3269.

[3] ——, "Wide-band compact antenna feed for multi-beam satellite communications," in *2015 9th European Conference on Antennas and Propagation (EuCAP)*, May 2015, pp. 1–4.

[4] ESA., appendix 1 to ESTEC ITT AO/1-7242/12/NL/MH, Circular Polarisation Dual-Optics Proof-of-Concept. 2011.

[5] A. Ericsson and D. Sjöberg, "A resonant circular polarization selective structure of closely spaced wire helices," *Radio Science*, vol. 50, no. 8, pp. 804–812, 2015, 2014RS005641. [Online]. Available: http://dx.doi.org/10.1002/2014RS005641

[6] D. Sjöberg and A. Ericsson, "A multi layer meander line circular polarization selective structure (mlml-cpss)." IEEE, 2014, pp. 464–468. [Online]. Available: http://dx.doi.org/10.1109/EuCAP.2014.6901792

[7] J. Sanz-Fernandez, E. Saenz, P. de Maagt, and C. Mangenot, "Circular polarization selective surface for dual-optics CP offset reflector antennas in Ku-band," in *2012 6th European Conference on Antennas and Propagation (EUCAP)*, March 2012, pp. 2683–2687.

[8] N. J. G. Fonseca and C. Mangenot, "High-performance electrically thin dual-band polarizing reflective surface for broadband satellite ap-

plications," *IEEE Transactions on Antennas and Propagation*, vol. 64, no. 2, pp. 640–649, Feb 2016.

[9] J. E. Roy and L. Shafai, "Reciprocal circular-polarization-selective surface," *IEEE Antennas and Propagation Magazine*, vol. 38, no. 2, pp. 18–32, 12 1996.

[10] G. Morin, "A circular polarization selective surface made of resonant helices," Defense Research Establishment Ottawa, Tech. Rep. 1269, 1995.

[11] R. Pierrot, "Reflector for circularly polarized waves," Mar. 10 1970, US Patent 3,500,420. [Online]. Available: http://www.google.com/patents/US3500420

[12] V. Liljegren, "Evaluation of circular polarization selective surfaces for space applications," Master's thesis, Lund University, 4 2013.

[13] W. V. Tilston, C. Cannon, Y. Sabourin, and A. Hurd, "A polarization selective surface for circular polarization," Dreo Contract #2SV84-00198, Til-tek, Final Report, March 30, Tech. Rep., 1986.

[14] W. V. Tilston, T. Tralman, and S. M. Khanna, "A polarization selective surface for circular polarization," in *Antennas and Propagation Society International Symposium, 1988. AP-S. Digest*, June 1988, pp. 762–765 vol.2.

[15] G. Morin, "Circular polarization selective surface made of resonant spirals," 1994, US Patent 5,280,298.

[16] M. A. Joyal and J. J. Laurin, "Design and analysis of a cascade circular polarization selective surface at K band," *IEEE Transactions on Antennas and Propagation*, vol. 62, no. 6, pp. 3043–3053, June 2014.

[17] Y. Zhao, M. Belkin, and A. Alù, "Twisted optical metamaterials for planarized ultrathin boradband circular polarizers," *Nature Communications*, 3:870 doi: 10.1038/ncomms1877 (2012).

[18] M. Albani, P. Balling, L. Datashvili, G. Gerini, P. Ingvarson, K. Pontoppidan, M. Sabbadini, D. Sjöberg, S. Skokic, and G. Vecchi, "Concepts for polarising sheets & "dual-gridded" reflectors for circular polarisation," in *ICECom, 2010 Conference Proceedings*, Sept 2010, pp. 1–4.

[19] S. J. Orfanidis, *Electromagnetic Waves and Antennas*. Rutgers University, 2002. [Online]. Available: http://www.ece.rutgers.edu/~orfanidi/ewa/

[20] D. Pozar, *Microwave Engineering*, 4th ed. John Wiley & Sons, 2004.

[21] J. Jackson, *Classical electrodynamics, 3rd edition.* John Wiley & Sons, 1999.

[22] J. Maxwell, *A Treatise on Electricity and Magnetism: 2.* Clarendon Press, 1873. [Online]. Available: https://books.google.se/books?id=OcS4BEiMNwoC

[23] "IEEE standard test procedures for antennas," *ANSI/IEEE Std 149-1979*, 1979.

[24] "The authoritative dictionary of IEEE standards terms, seventh edition," *IEEE Std 100-2000*, p. 75 and 559 and 981, Dec 2000.

[25] D. Sjöberg, *Circuit Analogs for Wave Propagation in Stratified Structures, Wave Propagation in Materials for Modern Applications*, A. Petrin, Ed. InTech, 2010. [Online]. Available: http://www.intechopen.com/books/wave-propagation-in-materials-for-modern-applications/circuit-analogs-for-wave-propagation-in-stratified-structures

[26] *Light Scattering by Systems of Particles: Null-Field Method with Discrete Sources: Theory and Programs.* Berlin, Heidelberg: Springer Berlin Heidelberg, 2006, ch. Basic Theory of Electromagnetic Scattering, pp. 1–82. [Online]. Available: http://dx.doi.org/10.1007/978-3-540-33697-6_1

[27] S. C. Kwon and G. L. Stuber, "Geometrical theory of channel depolarization," *IEEE Transactions on Vehicular Technology*, vol. 60, no. 8, pp. 3542–3556, Oct 2011.

[28] G. Kristensson, "Spridningsteori med antenntillämpningar," 1999. [Online]. Available: https://lucris.lub.lu.se/ws/files/5439763/4239041.pdf

[29] S. Ramo, T. Whinnery, and T. v. Duzer, *Fields and Waves in Communication Electronics.* John Wiley & Sons, 1965.

[30] N. Marcuvitz, *Waveguide Handbook.* New York: McGraw-Hill, 1951, p. 280 and 284.

[31] D. Sjöberg, "Circuit analogs for stratified structures," Tech. Rep. TEAT-7159, 2007.

[32] R. S. Chu and K. M. Lee, "Analytical model of a multilayered meander-line polarizer plate with normal and oblique plane-wave incidence," *IEEE Transactions on Antennas and Propagation*, vol. AP-35, no. 6, pp. 652–661, 6 1987.

[33] T. L. Blackney, J. R. Burnett, and S. B. Cohn, "A design method for meander-line circular polarizers." presented at 22nd Ann. Antenna Symp., Oct. 1972, pp. 1–5.

[34] "Concepts for polarising sheets & dual gridded reflectors for circular polarisation," Executive Summary, ESTEC Contract No. 21219/07/NL/ST, 2008.

[35] L. Goldstone, "A compact broadband c.p. mm wave horn." IEEE AP Symp., Albuquerque, 1982, pp. 640–643.

[36] C. V. Sokol, "Optimization techniques in cst studio suite." in *EUGM 2011*, 2011.

[37] J. Holland, *Adaptation in natural and artificial systems: an introductory analysis with applications to biology, control, and artificial intelligence*. University of Michigan Press, 1975.

[38] S. N. Sivanandam and S. N. Deepa, *Introduction to Genetic Algorithms*. Springer, 2008.

Appendices

Appendix A

Parametric Study of the 6 Layer Meander Line Design

Parameter study of the design corresponding to Figure 6.8. The parameters are seen in Table 6.2 and are varied ±5%. The gray area in the Figures in this chapter indicates the ±5% range obtained throuh simulations. The labeling of the parameter names are as indicated by Figure 5.9. Disclaimer, the Figures were obtained using 5 simulations per parameter and thus certain regions of the graph where the curves are rapidly changing might not be portrayed truthfully.

A.0.1 d_1

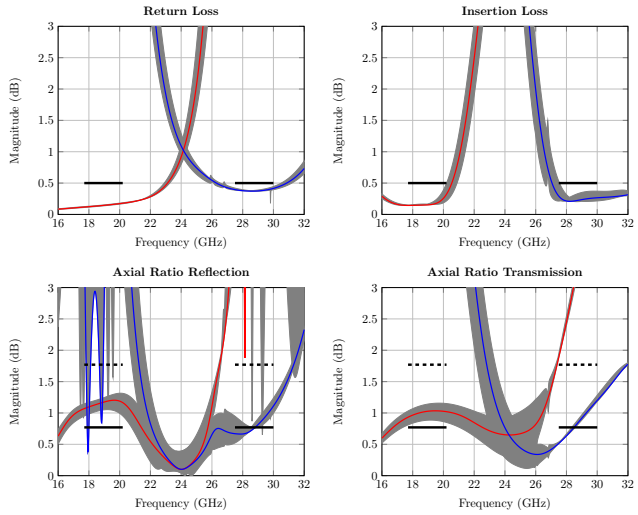

Figure A.1: Properties of the 9 layer meander line design. Gray area show effect of ±5% of d_1 parameter

A.0.2 d_2

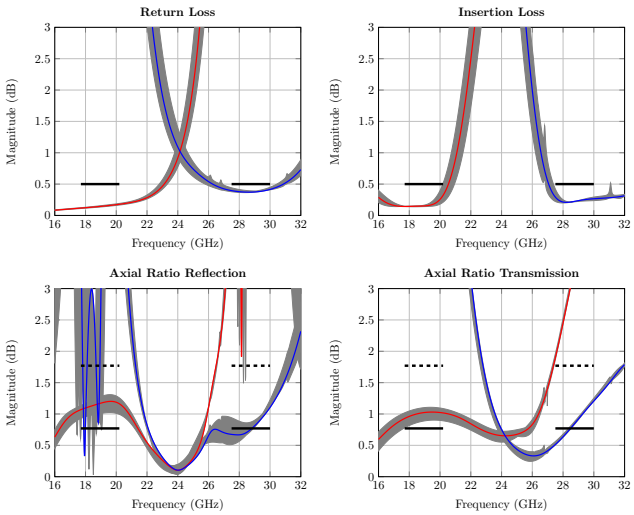

Figure A.2: Properties of the 9 layer meander line design. Gray area show effect of $\pm 5\%$ of d_2 parameter

A.0.3 d_3

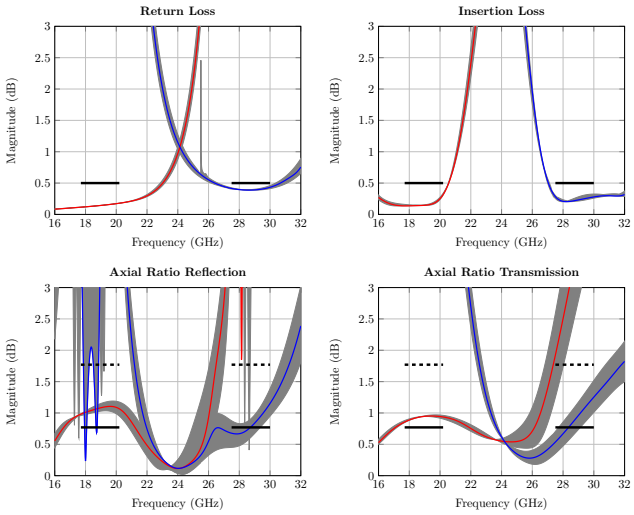

Figure A.3: Properties of the 9 layer meander line design. Gray area show effect of $\pm 5\%$ of d_3 parameter

A.0.4 w_1

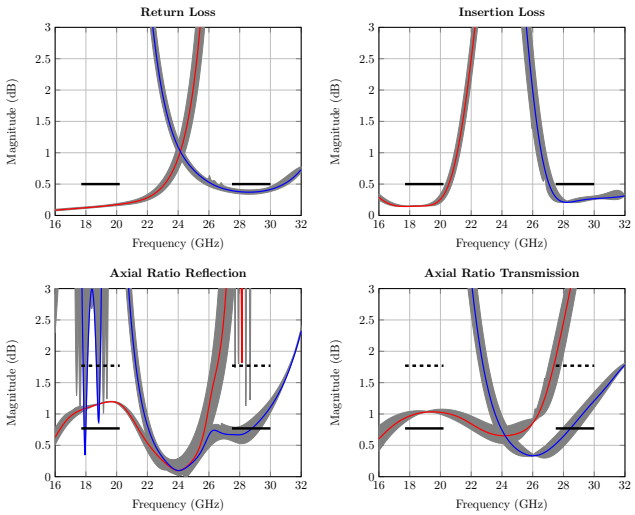

Figure A.4: Properties of the 9 layer meander line design. Gray area show effect of $\pm 5\%$ of w_1 parameter

A.0.5 w_2

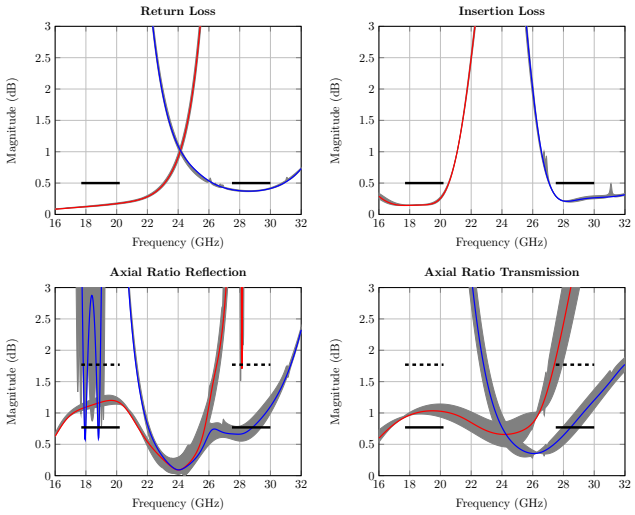

Figure A.5: Properties of the 9 layer meander line design. Gray area show effect of $\pm 5\%$ of w_2 parameter

A.0.6 w_3

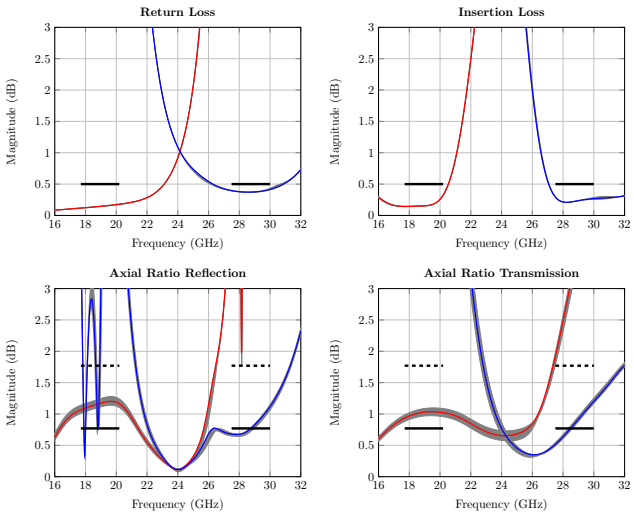

Figure A.6: Properties of the 9 layer meander line design. Gray area show effect of $\pm 5\%$ of w_3 parameter

A.0.7 h_1

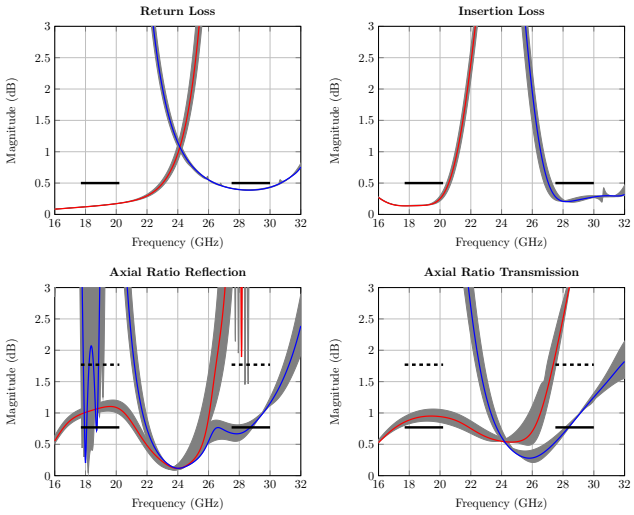

Figure A.7: Properties of the 9 layer meander line design. Gray area show effect of $\pm 5\%$ of h_1 parameter

A.0.8 h_2

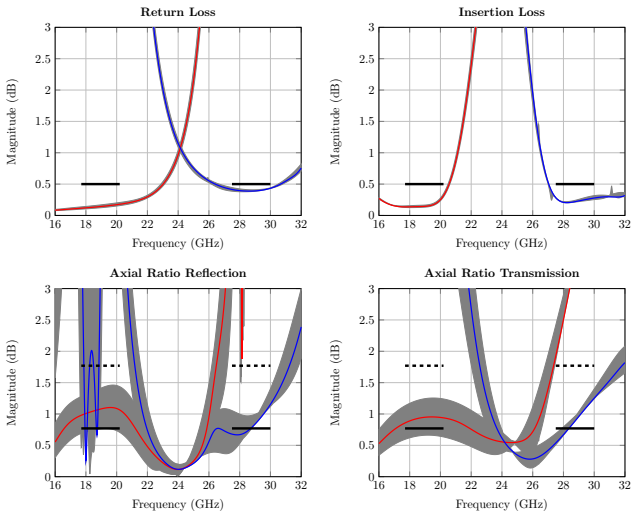

Figure A.8: Properties of the 9 layer meander line design. Gray area show effect of $\pm 5\%$ of h_2 parameter

A.0.9 h_3

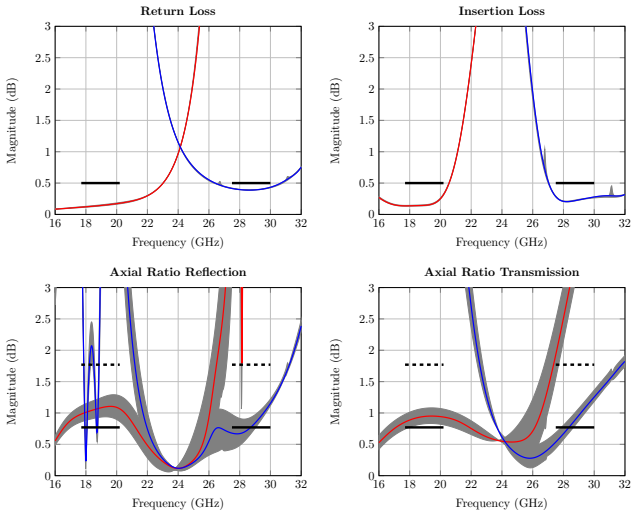

Figure A.9: Properties of the 9 layer meander line design. Gray area show effect of $\pm 5\%$ of h_3 parameter

A.0.10 P

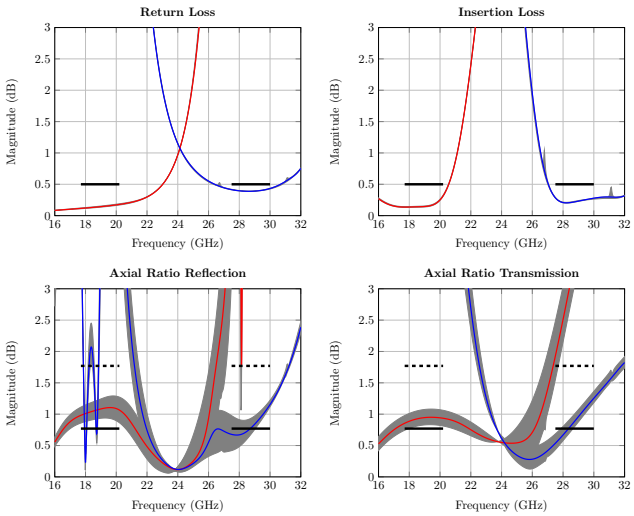

Figure A.10: PLACE HOLDER. NOT DONE SIMULATING. Properties of the 9 layer meander line design. Gray area show effect of $\pm 5\%$ of P parameter

Appendix B

Parametric Study of the 9 Layer Meander Line Design

Parameter study of the design corresponding to Figure 6.14. The parameters are seen in Table 6.4 and are varied ±5%. The gray area in the Figures in this chapter indicates the ±5% range obtained throuh simulations. The labeling of the parameter names are as indicated by Figure 5.9. Disclaimer, the Figures were obtained using 5 simulations per parameter and thus certain regions of the graph where the curves are rapidly changing might not be portrayed truthfully.

B.0.1 d_1

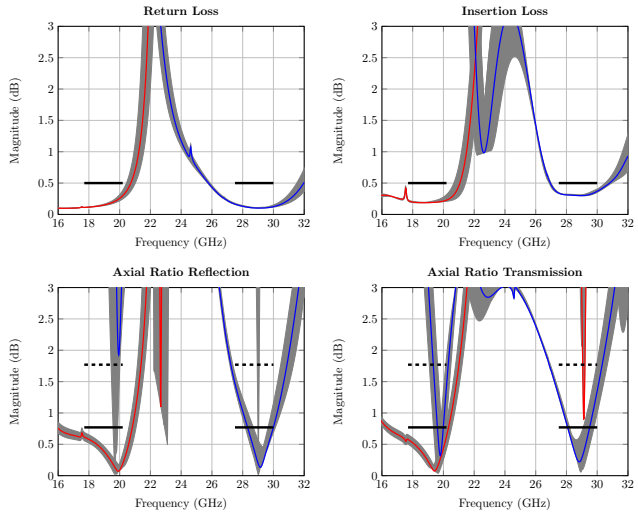

Figure B.1: Properties of the 9 layer meander line design. Gray area show effect of ±5% of d_1 parameter

B.0.2 d_2

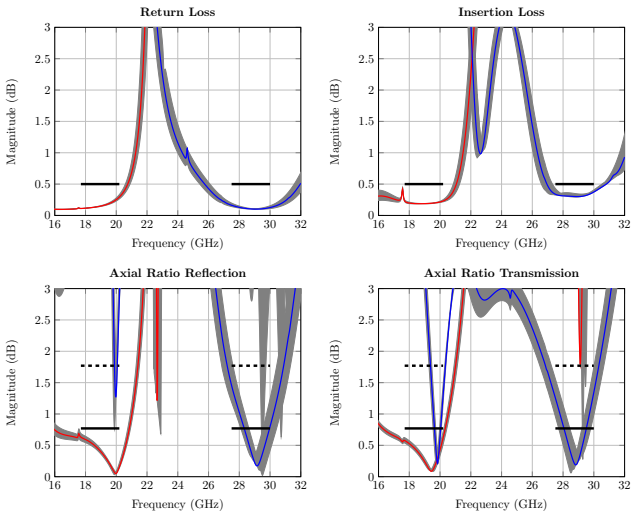

Figure B.2: Properties of the 9 layer meander line design. Gray area show effect of $\pm 5\%$ of d_2 parameter

B.0.3 d_3

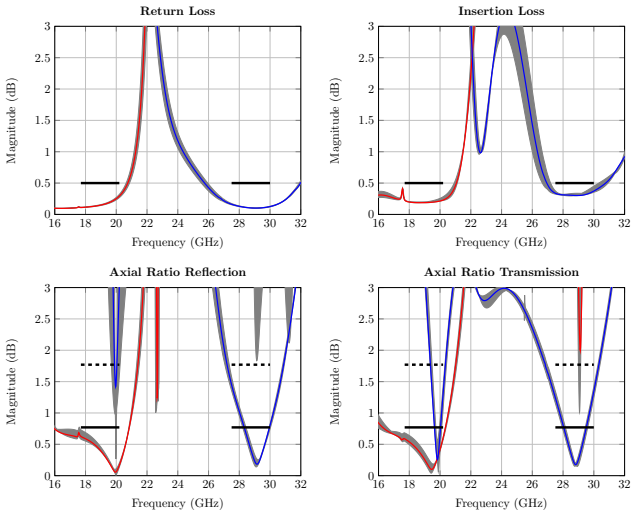

Figure B.3: Properties of the 9 layer meander line design. Gray area show effect of $\pm 5\%$ of d_3 parameter

B.0.4 d_4

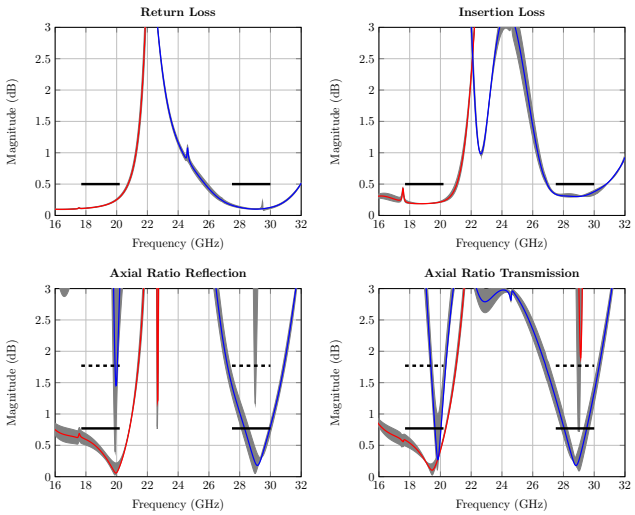

Figure B.4: Properties of the 9 layer meander line design. Gray area show effect of $\pm 5\%$ of d_4 parameter

B.0.5 w_0

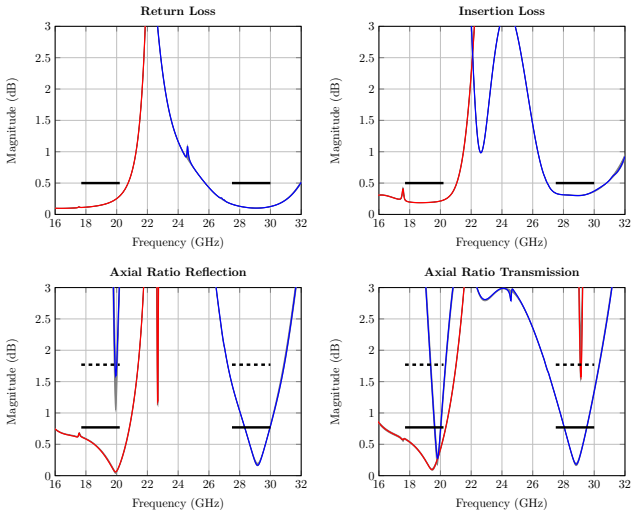

Figure B.5: Properties of the 9 layer meander line design. Gray area show effect of $\pm 5\%$ of w_0 parameter

B.0.6 w_1

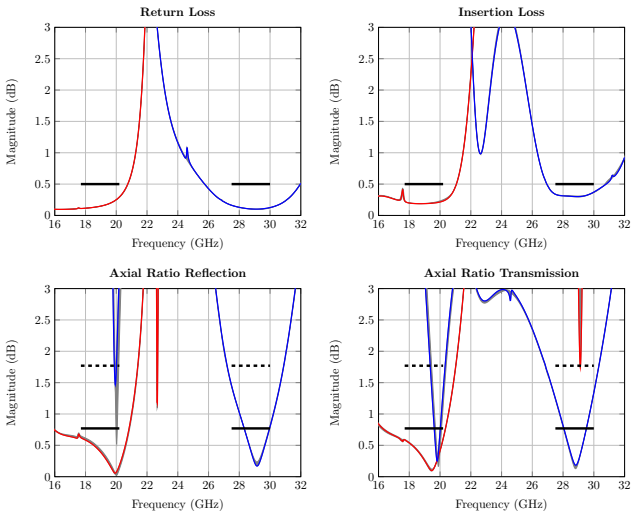

Figure B.6: Properties of the 9 layer meander line design. Gray area show effect of $\pm 5\%$ of w_1 parameter

B.0.7 w_2

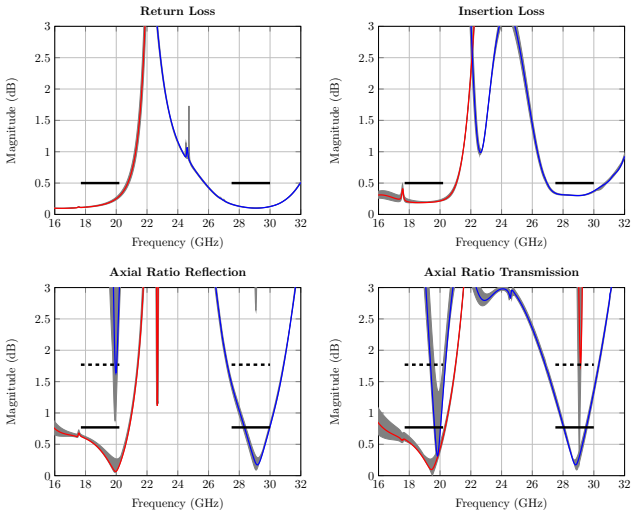

Figure B.7: Properties of the 9 layer meander line design. Gray area show effect of $\pm 5\%$ of w_2 parameter

B.0.8 w_3

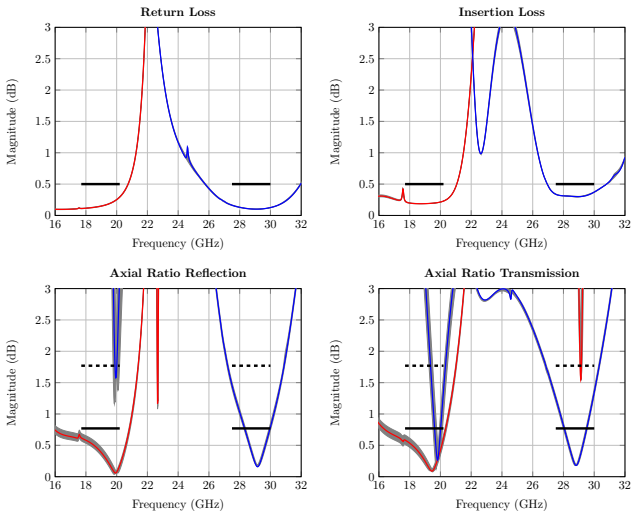

Figure B.8: Properties of the 9 layer meander line design. Gray area show effect of $\pm 5\%$ of w_3 parameter

B.0.9 w_4

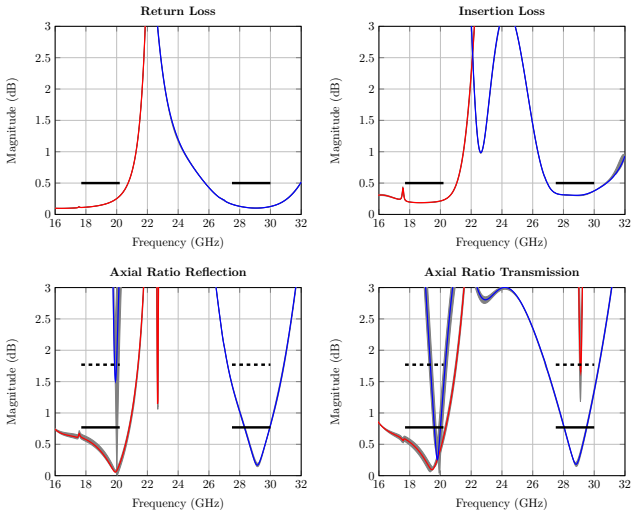

Figure B.9: Properties of the 9 layer meander line design. Gray area show effect of $\pm 5\%$ of w_4 parameter

B.0.10 h_0

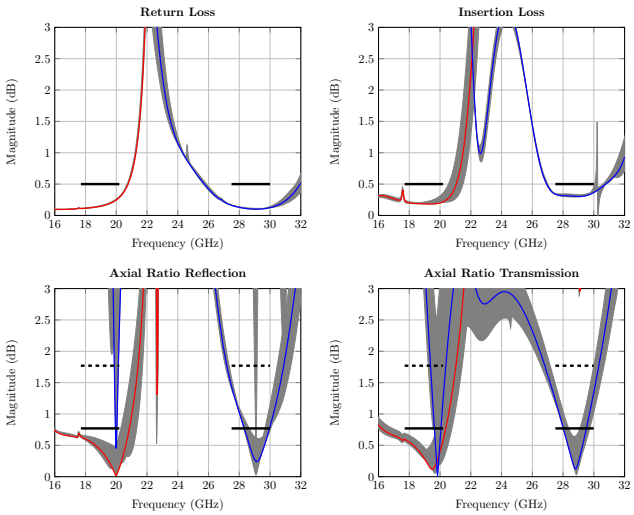

Figure B.10: Properties of the 9 layer meander line design. Gray area show effect of $\pm 5\%$ of h_0 parameter

B.0.11 h_1

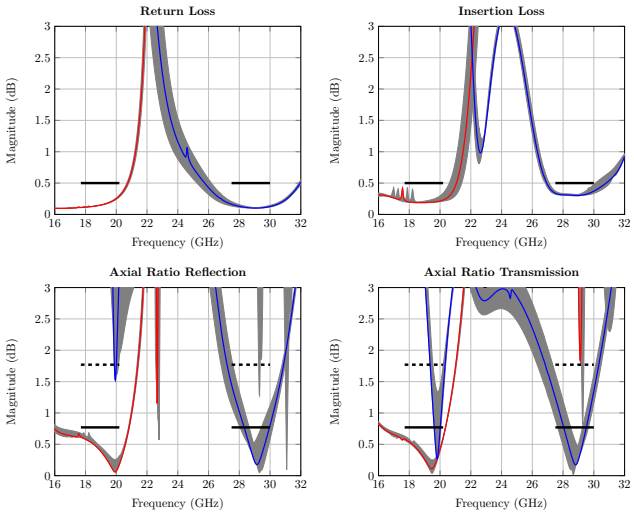

Figure B.11: Properties of the 9 layer meander line design. Gray area show effect of $\pm 5\%$ of h_1 parameter

B.0.12 h_2

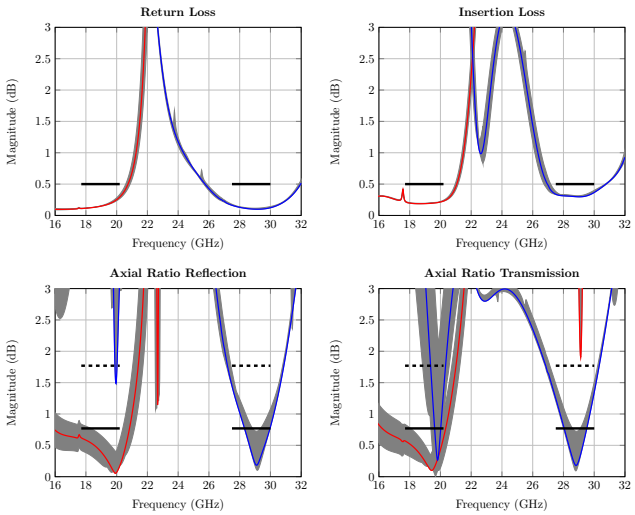

Figure B.12: Properties of the 9 layer meander line design. Gray area show effect of $\pm 5\%$ of h_2 parameter

B.0.13 h_3

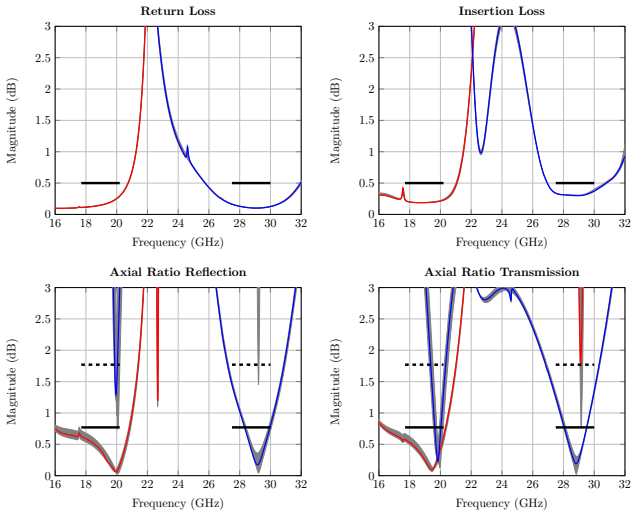

Figure B.13: Properties of the 9 layer meander line design. Gray area show effect of $\pm 5\%$ of h_3 parameter

B.0.14 h_4

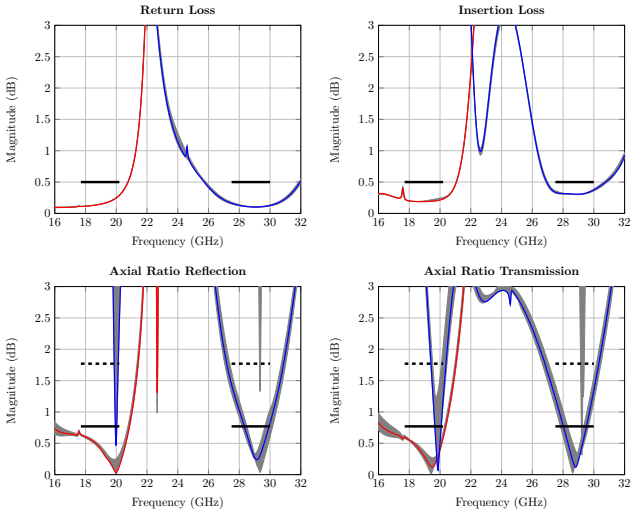

Figure B.14: Properties of the 9 layer meander line design. Gray area show effect of $\pm 5\%$ of h_4 parameter

B.0.15 P

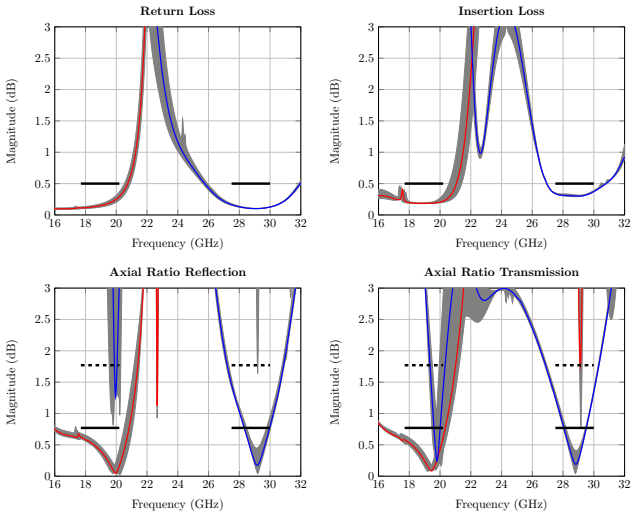

Figure B.15: Properties of the 9 layer meander line design. Gray area show effect of $\pm 5\%$ of P parameter

LUND
UNIVERSITY

Series of Master's theses
Department of Electrical and Information Technology
LU/LTH-EIT 2016-540
http://www.eit.lth.se